DISS. ETH NO. 24025

Experiments on femtomagnetism

A thesis submitted to attain the degree of

DOCTOR OF SCIENCES of ETH Zurich

(Dr. sc. ETH Zurich)

presented by

GERARD SALVATELLA

Màster en fotònica, Universitat Politècnica de Catalunya

born on 20.08.1986

citizen of Catalunya, Spain

accepted on the recommendation of

Prof. Dr. A. Vaterlaus, examiner
Dr. Y. Acremann, co-examiner
Prof. Dr. D. Pescia, co-examiner
Prof. Dr. G. Schönhense, co-examiner

2016

Abstract

When a ferromagnet is exposed to a femtosecond laser pulse, its magnetization is reduced within less than a picosecond. This surprising effect has challenged the established theory on magnetization dynamics and, at the same time, has fostered femtomagnetism as a new area of research. While substantial progress has been made in the past two decades, the underlying mechanisms governing this phenomenon are not yet fully understood.

In this work, two different sets of investigations have been performed to add further evidence on this topic. First, a spin- and time-resolved photoemission experiment has been carried out using a free electron laser source to access the magnetization dynamics of electrons below the Fermi surface. It has been found that the demagnetization behavior of these electrons is in line with studies by more indirect methods, confirming the reliability of magneto-optical Kerr experiments. Also limitations on the magnetization detection due to space charge effects have been modeled to provide insight in future experimental designs at 4th generation light source facilities.

Second, table-top experiments based on the magneto-optical Kerr effect have been undertaken in different setup schemes. The effect of the pump pulse length has been determined. It has been found that the magnetization dynamics in the picosecond timescale can be fully described by those in the femtosecond timescale, indicating that they follow the same underlying mechanism. The influence of pre-heating the sample with an extra pump pulse has been also examined. In this case nonlinearities in the system for short pump-pump delays have been detected. A comparison with a spin-flip model by Koopmans *et. al.* [149] has been performed. Finally, the role of hot electron diffusion in an indirect demagnetization process has been studied. The competition between light-induced and hot-electron-driven demagnetization for different sample thicknesses has been observed. It has been concluded that a diffusion mechanism is sufficient to explain the measurements.

Zusammenfassung

Wenn ein Ferromagnet einem Femtosekunden-Laserpuls ausgesetzt wird, wird seine Magnetisierung in weniger als einer Pikosekunde verringert. Diese überraschende Wirkung hat die etablierte Theorie der Magnetisierungsdynamik in Frage gestellt und gleichzeitig den Femtomagnetismus als neues Forschungsgebiet gefördert. Obwohl in den letzten zwei Jahrzehnten beträchtliche Fortschritte erzielt wurden, sind die zugrunde liegenden Mechanismen für dieses Phänomen noch nicht vollständig verstanden.

In dieser Arbeit wurden zwei verschiedene Arten von Untersuchungen durchgeführt, um weitere Einsichten in diesem Feld zu gewinnen. Zuerst wurde ein spin- und zeitaufgelöstes Photoemissionsexperiment mit einer freien Elektronenlaserquelle durchgeführt, um die Magnetisierungsdynamik von Elektronen unterhalb der Fermi-Oberfläche zu untersuchen. Es wurde herausgefunden, dass das Entmagnetisierungsverhalten dieser Elektronen mit Experimenten basierend auf indirekten Verfahren übereinstimmt, was die Zuverlässigkeit magneto-optischer Kerr-Experimente bestätigt. Ferner wurden Begrenzungen in der Detektion der Magnetisierung aufgrund von Raumladungseffekten modelliert, um Hinweise für zukünftige experimentelle Designs bei Synchrotron und Freie-Elektron-Laser zu liefern.

Zweitens wurden Tischversuche auf der Basis des magnetooptischen Kerr-Effekts in unterschiedlichen Aufbauplänen durchgeführt. Die Wirkung der Pumppulslänge wurde ermittelt. Es wurde herausgefunden, dass die Magnetisierungsdynamik im Pikosekunden-Zeitmaßstab vollständig durch jene in der Femtosekunden-Zeitskala beschrieben werden kann, was anzeigt, dass sie demselben zu Grunde liegenden Mechanismus folgen. Der Einfluss der Vorgängig Erwärmung der Probe mit einem zusätzlichen Pumppuls wurde ebenfalls untersucht. In diesem Fall wurden Nichtlinearitäten im System für kurze Pumpenverzögerungen erkannt. Ein Vergleich mit einem Spin-Flip-Modell von Koopmans *et. al.* [149] wurde durchgeführt. Schließlich wurde die Rolle der Heisselektronendiffusion in einem indirekten Entmagnetisierungsprozess untersucht. Der Wettbewerb zwischen lichtinduzierter und heißelektronengetriebener Entmagnetisierung für unterschiedliche Probendicken wurde beobachtet. Es wurde schlussgefolgert, dass ein Diffusionsmechanismus ausreicht, um die Messungen zu erklären.

Contents

Chapter 0

Motivation

During the last half of the 20th century and over the course of the 21st an overwhelming revolution has pushed the world toward digitalization. It has been estimated [109] that in 1986 still 99 % of the world's stored information was in analog substrate. Thanks to disruptive technological advances[1], digitalization of the information grew at an annual rate of 20 % and the share of analog storage shrank to a 70 % in 2000. In 2007, 94 % of the world's technological memory was in digital form.

Today the digital storage market has two main competing technologies: magnetic storage, represented by hard disks drives (HDD) and optical drives (DVD, Blu-ray), and MOS floating-gate transistor-based storage, represented by flash memory and solid state drives (SSD). The former has dominated the industry for the past thirty years with ever increasing areal storage densities and low production cost per bit. However, flash-related technology, which is relatively new (taking off in the 1990s), has largely benefited from Moore's Law and is increasing both its performance and capacity at an exceptional rate. In fact, actual HDD densities (up to 1.3 TB in^{-2}), are already lower than

[1] For instance,

- The rise of analog computers during the first half of the 20th century, inspired by Charle's Babbage first analytical engine as early as 1835.
- The invention of the *telegraphone* by Valdemar Poulsen in 1889 [206], the first machine which could record and reproduce sounds or signals by storing them in a magnetized steel wire. It laid the foundation for magnetic tape recording technology during the first half of the 20th century.
- The discovery of anysotropic magnetoresistance by Lord Kelvin in 1856 and its successor, the giant magnetoresistance, by Fert and Gruenberg in 1988. It paved the way to the manipulation of magnetic materials at the electronic level.
- The shift from vacuum tube electronics to transistors, after their operative production in the 1950s. It boosted the miniaturization of electronic components for eventual use in domestic applications.

the commercially available high-cost SDDs ($5\,\mathrm{TB\,in^{-2}}$) [174]. In 2016, NAND flash memories outperformed HDD technology in areal storage density for the first time, and they are expected to grow at a faster rate than magnetic storage in this aspect [174]. While HDDs still hold the upper hand when it comes to price per bit, this is likely to be made up for by the flash industry in the near future. A crucial feature for the advancement of digital storage technology is the speed of read/write operations. In this case it is also favorable to flash-type devices. Current read/write speeds for high-performance commercial SSDs are on the order of $500\,\mathrm{Mbit\,s^{-1}}$, whereas similar quality HDDs do no much better than $120\,\mathrm{Mbit\,s^{-1}}$ [126]. This constitutes a great impediment for the progress of magnetic storage technology. A substantial leap will require finding out exceptionally faster ways of recording while maintaining robustness and reliability.

Writing times in HDDs are mainly limited by the speed at which a single magnetic domain can be reversed. Conventional switching techniques have made use of static magnetic fields in a direction parallel to the easy axis of the magnetic particles forming the recording medium[2] [125]. These particles present an acicular (elongated) shape with lengths of 0.25 µm to 0.75 µm and widths of 0.05 µm to 0.15 µm [125]. They were oriented in the longitudinal direction within the recording layer of the disk. When the so-called *fringing field* of an inductive head passed by the recording material, the particles were reversed by 'brute force'. This type of switching, commonly named Stoner-Wohlfarth [252], had reversal times in the nanosecond range.

This model has been now superseded by the introduction of perpendicular magnetic recording [121, 120, 201], where the particles in the recording layer are set perpendicular to the layer surface. This has not only allowed for higher densities but also higher coercivity materials, since in this case the field can flow deeper into the recording layer thanks to the introduction of a soft magnetic underlayer. In both configurations, the torque exterted by the part of the magnetic field perpendicular to the particle spin makes those spins precess at an increasing angle until reversal occurs. This magnetic reversal by precession can be described by the well-known Landau-Lifshitz-Gilbert (LLG) equation [157]:

$$\frac{\mathrm{d}\mathbf{M}}{\mathrm{d}t} = -\gamma \mathbf{M} \times \mathbf{H} - \frac{\alpha}{M_s}(\mathbf{M} \times \frac{\mathrm{d}\mathbf{M}}{\mathrm{d}t}). \tag{0.1}$$

The equation states that the rate of change of the magnetization $\mathbf{M}$ is proportional to the magnetic torque induced by the effective field $\mathbf{H}$ seen by the medium, and is further affected by a phenomenological damping torque of

[2] They are usually made of Co-based alloys such as CoCrPt in combination with some form of oxide. See [201] for further details.

intensity α^3. With all its simplicity, eq. 0.1 has been widely and very successfully employed to model the dynamics of magnetic recording [260]. The characteristic time of this equation is given by the Larmor frequency $\omega_L = \gamma H$. This means that for high fields on the order $1\,\mathrm{MA\,m^{-1}}$, times as short as 10 ps should be available. Such fields are accessible in ultrashort electron beams at accelerator facilities and indeed reversal times in the ps range have been reported in some experiments [61, 239, 257]. Nonetheless, even for the most novel commercial recording techniques such as heat-assisted magnetic recording, which is likely to see light in the upcoming years, spin reversal times remain in the nanosecond scale [260, p.198] due to limitations from thermal instabilities and unavailability of high-field write heads.

A deficiency of the LLG equation is that no details of the microscopic mechanisms underlying the reversal process are provided. They enter the equation only through the parameters γ and α, which have quantum mechanical origin. The damping parameter α, for instance, has typically small values (0.01 to 0.1). This indicates that the coupling of the spin angular momentum (magnetization) with the sources of damping is relatively weak. For this reason, the finding in 1996 by Beaurepaire [26] that a ferromagnet could be demagnetized within less than a picosecond when heated by a femtosecond laser pulse was received with both notable surprise and great interest by the magnetism community. The magnetic fields required by the LLG equation to undertake a process at such speeds are clearly not available from table-top laser pulses[4], hence these results were challenging the current knowledge on magnetization dynamics.

The solution to this paradox is to be found precisely in the microscopic understanding of the governing interactions at play. Consider, for instance, the excitation of a ferromagnet with a magnetic field pulse of $1\,\mathrm{MA\,m^{-1}} \approx 1\,\mathrm{T}$. In this case, all the spins in the system experience an energy shift of $g\mu_B H \approx 10^{-4}\,\mathrm{eV}$. In the case of a laser pulse, however, only a small fraction of the electrons are excited, but they reach excitation energies on the order of several eV, shortly entering a high non-equilibrium state. This shows that the mechanisms responsible for the transfer of angular momentum will substantially differ in each of the two cases. For example, Koopmans [148] and his co-workers attempted to give an explanation of the sub-picosecond demagnetization from the LLG perspective by invoking the electronic exchange field, which is on the order of $10^3\,\mathrm{T}$. To make it more complicated, different types of mechanisms dominate at different timescales. Magnetic dipole, Zeeman and spin-lattice interactions, for instance, operate on a timescale of 100 ps–1 ns. Phonon-phonon, spin-phonon and electron-phonon interactions

[3] In the equation, $\gamma = g\mu_B/\hbar$, with g the gyromagnetic ratio and μ_B the Bohr magneton. M_s is the saturation magnetization.

[4] For a pulse fluence of $10\,\mathrm{mJ\,cm^{-2}}$, for instance, magnetic fields are on the order of µT!

prevail at timescales 1 ps–100 ps, whereas electron-electron and exchange interactions lie in the femtosecond realm [283].

The appearance of all these possibilities endorsed the birth of a whole new field of research devoted to investigating the magnetization dynamics of solids in the femtosecond timescale. This new field, also known as *femtomagnetism* [283], could have the potential to foster a breakthrough in the magnetic storage technology toward never-seen recording speeds.

Over the last two decades, several theories have appeared to describe the ocean of interactions that govern magnetic materials at ultrafast timescales, and it turned out to be more complicated than expected. A major leap toward technological implementation arrived in 2007 when Stanciu [245] and his colleagues demonstrated all-optical switching of a ferrimagnetic medium with 40 fs pulses. It then became clear that the manipulation of spins by light at the femtosecond scale was a reality. Nonetheless, accurate control of the magnetization at these timescales also demands a clear understanding of its underlying physical processes. To date, these are still a matter of strong controversy [119].

With this big picture in mind, the present thesis intends to add further evidence on the topic of femtomagnetism by performing a series of experiments on ferromagnetic thin films. In the first chapter, an experiment using spin- and time- resolved photoemission detection with a femtosecond light source from a free electron laser working in the extreme ultraviolet regime is described. In the second chapter, studies of the demagnetization dynamics in nickel thin films by means of the magneto-optical Kerr effect are presented.

Chapter 1

Time- and spin-resolved photoemission

In this chapter the advantages of a new generation femtosecond, ultra-bright free electron laser operating in the ultraviolet range will be exploited to study the ultrafast magnetization dynamics of an iron film resolved in time and spin. It will be shown that demagnetization in iron thin films occurs on a timescale shorter than 100 fs. Unfortunately, detection of the photoelectron polarization becomes less efficient due to the influence of space charges during the photoemission process, an effect that is further confirmed by space charge simulations.

1.1 Overview on photoemission spectroscopy

Photoemission spectroscopy (PES) has become one of the most established methods to study the electronic structure of molecules, solids and surfaces [115]. Although widely used in fields such as surface chemistry and biology, it has particularly contributed to unveil the fundamental principles of solids. From the early experiments by Hertz and Hallwachs in 1887 [108, 102] through the confirmation by Lenard [159] in 1902 of the photoelectric effect predicted by Einstein, the evolution of PES has experienced a notorious advance (most remarkably in the early 1960s), yet the fundamental experiment for spectroscopic purposes is carried out today in the same way as in the beginning of the last century. The basic principle utilizes a supply of monochromatic photons, with energy $h\nu$ and a certain polarization, which are commonly generated either in a laboratory as VUV or soft x-ray sources, or in a larger facility such as synchrotrons and free electron lasers. The radiation hits the surface target at an angle with the normal and electrons are emitted therefrom. Their kinetic energy can be determined by use of electrostatic analyzers as a function of the emission angle, the photon

energy or the spin polarization. Since the photoelectrons obtained this way reflect the electronic eigenstates of the system, valuable information such as the density of states, the band configuration or the magnetization distribution can be fetched.

The most common approach to describe photoemission spectra comes from Fermi's golden rule after first order perturbation theory. One starts from a system of N electrons in the ground state $|\psi_i\rangle$ that is excited by a photon of energy $h\nu$ to a final state $|\psi_f\rangle = |\psi_{\boldsymbol{k},\alpha}\rangle$, where $\boldsymbol{k}$ is the final momentum of the photoelectron and α is the set of quantum numbers that define the state of the remaining $N-1$ electron system. In this approximation the kinetic energy of the photoelectron is given by $\varepsilon_{\boldsymbol{k}} = \hbar^2 k^2/2m_e$, and the photocurrent J by

$$J_{\boldsymbol{k}}(h\nu) = \frac{2\pi}{\hbar}\sum_{\alpha} |\langle\psi_{\boldsymbol{k},\alpha}|H_{\mathrm{PE}}|\psi_i\rangle|^2 \delta(\varepsilon_{\boldsymbol{k}} - \varepsilon_\alpha - h\nu) \tag{1.1}$$

where the perturbation interaction H_{PE} involves a spin-less electron in a system under an electromagnetic field potential $\boldsymbol{A}$. For moderate photon intensities this can be approximated to

$$H_{\mathrm{PE}} \approx \frac{e}{m_e c}\boldsymbol{A}\cdot\hbar\boldsymbol{k} \tag{1.2}$$

When considering relativistic effects, the Dirac equation shows that polarization of the photoelectrons can be obtained either with unpolarized light, when there is a spin polarization of the ground state, as in magnetic materials, or with polarized light, that interacts via spin-orbit coupling to give a net polarization. The latter effect has been thoroughly exploited in the so-called magnetic dichroism, where the polarization of light induces small but important asymmetries in the photoelectron distribution. The technique of the x-ray magnetic circular dichroism (XMCD), for instance, has become a popular experimental method for probing ultrafast magnetism [45].

The detection of spin polarization in particles can generally be achieved by Stern-Gerlach type of detectors. However for electrons the influence of the Lorenz force and the uncertainty principle makes it an impossible task. For this reason, the spin of photoemitted electrons is usually retrieved from spin-dependent scattering effects such as Mott scattering or Møller scattering in ferromagnets. Mott detectors [87, 181] have become a reliable polarimeter choice and are currently in widespread use. At energies below 100 eV spin-polarized low energy electron diffraction (SPLEED) detection is also a common alternative [263]. These types of detectors suffer nonetheless from a very low efficiency due to the Coulomb interaction dominating over the spin-orbit in the scattering cross-section. Recent developments have taken advantage of the exchange interaction in Fe crystals to improve the spin asymmetry at very low energies, with reported efficiencies up to two orders

of magnitude higher [275]. Even more recently, use of the lateral conservation of momentum in spin-filter crystals, combined with the advent of multichannel plate amplification, has led to predicted SPLEED detection with figures of merit[1] higher than 10^{-2} [155].

PES and its variations have been extensively used to investigate solid state phenomena such as spin-polarized surface states, quantum-well states, self-energizing effects or ferromagnetic oxide systems and interlayers [153]. In particular, the area of study around ferromagnetic thin films and multilayers has attracted a lot of attention due to their association with the giant magneto-resistance (GMR) effect discovered by Fert and Günbert in the late 1980s, which has seen great application potential in modern technologies, e.g. in magnetic storage devices. Additionally, the advent of reliable ultrafast laser sources in the extreme ultraviolet (XUV) and the soft x-ray regime with unprecedented brilliances, has triggered a new field of interest on the ultrafast dynamics of magnetic materials.

The following experiment makes use of the advantages of the new generation free electron laser FLASH in Hamburg to reveal the femtosecond dynamics of the magnetization in a ferromagnet thin film. Thanks to the high photon count per pulse of these sources, a time- and spin-resolved photoemission scheme has been prepared to access the intra-band magnetic evolution during a light-induced demagnetization process.

1.2 Experimental setup

The setup used for this photoemission experiment consists of a mobile endstation provided with a system of chambers under ultrahigh vacuum (UHV) conditions. UHV environments are necessary to avoid contamination of the samples, which are grown through evaporation as detailed later in this chapter. Furthermore, photoemitted electrons should be held off of any external interactions such as collisions with gas molecules in order to keep the information they are carrying until detection. The system has been designed to be compact and easily attachable to the end branches of the free electron laser facility in Hamburg (FLASH), in order to save time and optimize maneuverability during the limited measurement times.

1.2.1 Layout

The setup, depicted in figure 1.1, is mounted around two interconnected UHV chambers. The preparation chamber provides the tools for sample preparation. Samples ready to be used can be transferred to the measurement chamber for the experiment. The connection arm contains a valve that

[1] see section 1.2.5

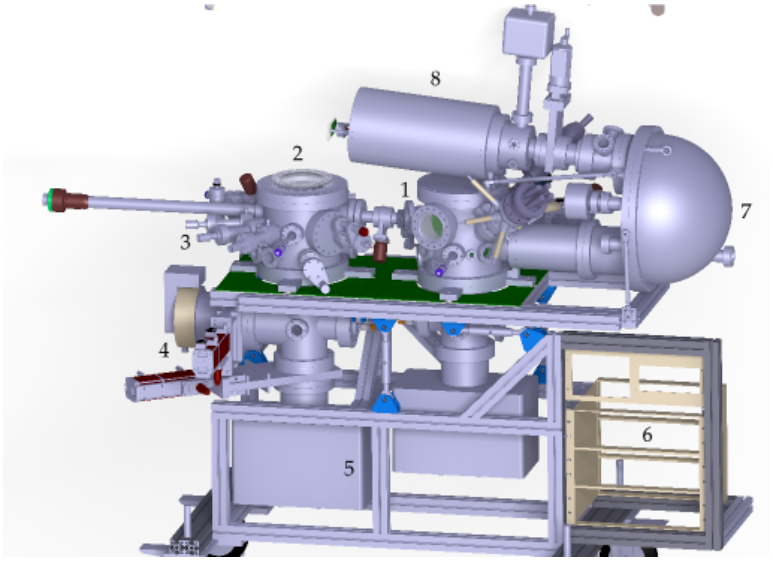

Figure 1.1: Mobile end-station for photoemission experiments. 1. Measurement chamber (with the electron gun attached). 2. Preparation chamber. 3. Knudsen effusion cells and transfer mechanism for the samples. 4. Main turbopump and security valve (red). 5. Ion pumps for UHV environment. 6. Panels for controllers and monitoring devices. 7. Hemispherical energy analyzer (PHOIBOS). 8. Voltage-floated Mott detector (smaller ion pump and valve visible on top).

provides isolation to both chambers, allowing simultaneous sample preparation and actual measuring to minimize time constraints. Equipped with standard turbo pumps as well as with ion and titanium-sublimation pumps, both chambers achieve nominal pressures lower than 10^{-9} mbar when a proper "baking" protocol is applied to flush out adsorbed impurities. An hemispherical energy analyzer is attached to the measurement chamber to collect the photoelectrons and sort them out as a function of their kinetic energy. Finally, a Mott detector provides a measurement of the polarization of the electrons, which can be translated into a value for the magnetization of the sample. The measurement chamber has been equipped with a μ–metal shield to suppress the influence of the earth magnetic field that distorts the path of the outcoming photoelectrons into the analyzer.

1.2.2 Preparation chamber and sample making

The preparation chamber is provided with two Knudsen effusion cells for material evaporation onto the sample. The Knudsen cells contain a tungsten crucible in which high purity iron lumps are deposited. The crucible is then heated by electron bombardment and the iron vapor is let out through an

orifice into the chamber. The samples chosen for study were iron thin films of 10–15 monolayers deposited on tungsten W(110). Such systems have been widely studied and are relatively easy to replicate. Up to thicknesses of a few tens of monolayers they can be magnetized in a single domain with fairly low coercive fields (on the order of 10 Oe) that do not significantly change with thickness [177]. This feature leaves some margin of error during the preparation process of the samples, since the thickness accuracy need not be as high. For the chosen thickness range the easy axis is found to be mainly in the $[1\bar{1}0]$ direction [281, 15].

In order to prepare the samples the polished W(110) crystal substrate must be cleaned out of impurities. First, the substrate is annealed at around 1400 °C under an oxygen atmosphere of 4×10^{-10} mbar during 5 min. This process retrieves the carbon impurities from the tungsten surface through oxidation to CO as detailed in [35, 279]. Next, the tungsten surface is flash-annealed for 10 s at a higher temperature of nearly 2000 °C, which removes the tungsten oxide (WO) formed during the previous annealing and the remaining adsorbed O_2. The flashing step is repeated two to three times between 30 s cooling intervals as suggested in [279]. The surface needs to cool down for a period of 30 min after the cleaning process and before the iron evaporation can take place. For the latter, the Knudsen cells must be temperature stabilized so as to provide a constant evaporation rate. This can be partly monitored by the increase of pressure in the chamber (from approx. 2×10^{-10} mbar to 3×10^{-10} mbar). The deposition rate can be estimated with a quartz balance located in the place of the sample (typical values lie around 0.5 monolayers per minute).

1.2.3 Measurement chamber

The measurement chamber is structurally analogous to the preparation chamber, but it is additionally equipped with a μ–metal shield from the inner surface to suppress the earth magnetic field, which affects photoelectron trajectories before their entrance to the analyzer. A sample holder attached to a piezo stage is placed in the middle of the chamber. The switching magnetic field to magnetize the sample is provided by a modified, custom version of a typical Helmholtz coil system. Such a system is shown in fig. 1.2 and further detailed in [81]. This coil geometry features minimal inductance and fast switching rates of a few μs at the expense of high coil currents. Thus, a high current pulser has been developed that is able to deliver currents up to 1000 A at 700 V with repetition rates up to 10 kHz and pulses as short as 2 μs.

Perpendicular to the sample surface and 40 mm apart lies the entrance of the photoelectron energy analyzer. At 45° from the collector a window allows the laser beams into the sample, and in the symmetrically opposite side an

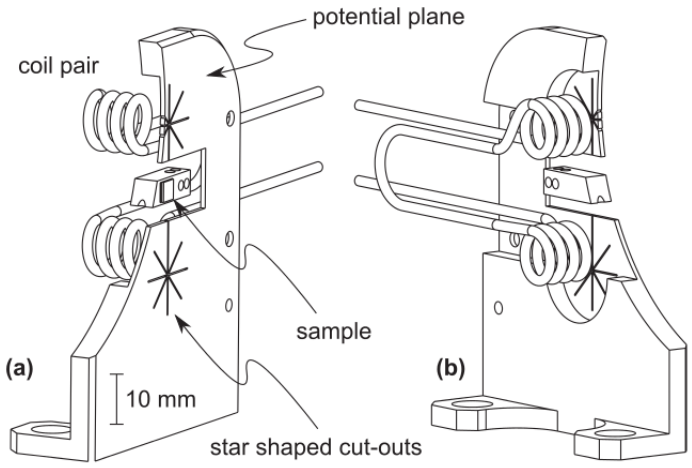

Figure 1.2: Sample holder and modified Helmholtz coil system from (a) front and (b) back. Reprinted from [81].

electron gun has been attached for calibration of the spin detector and for electron optics alignment.

1.2.4 Energy analyzer and lens system

During a photoemission process the electrons extracted from the sample show a wide range of (kinetic) energy values depending on the photon energy of the excitation and the collision processes inside the material they were involved in. Therefore it is convenient to select specific energy ranges when measuring the polarization of such electrons in order to calculate the magnetization of the material (for instance one may want to measure the electrons coming from a certain energy band which are responsible for the magnetic behavior). This is achieved with an hemispherical electrostatic energy analyzer[2], which provides recording of kinetic energy spectra for ions in the nominal energy range 0 keV to 15 keV. Before reaching the hemispherical capacitor (the actual analyzer), the photoelectrons pass through an electron lens system composed of ten lens tubes, which define the analysis area and angular acceptance by imaging the emitted particles onto the entrance slit of the analyzer (see figure 1.3). The lens system also accelerates or decelerates the particles to accommodate them to the capacitor energy requirements. The pass energy E_{pass}, which is proportional to the voltage difference between the two hemispheres of the capacitor, is the operating energy of the analyzer. The job of the lens system is therefore to set the particle nominal kinetic energy E_{kin} to E_{pass}. This step is crucial in energy

[2]In the current setup a SPECS PHOIBOS 150 model has been used.

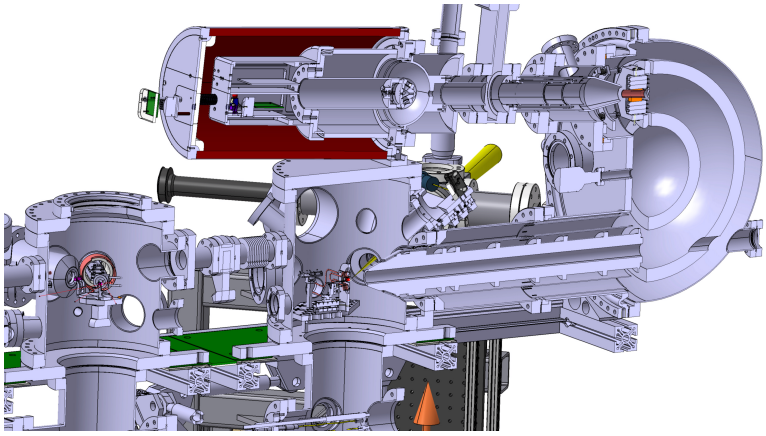

Figure 1.3: Cross-sectional view of the main components of the setup. Preparation chamber (left), measurement chamber (center), energy analyzer (right) and Mott detector (top).

analyzers, since the energy resolution of a measurement, ΔE, is proportional to the energy at which the analysis is carried out (E_{pass} in this case). To this regard, analysis at moderate energies not only favors higher resolution but also limits perturbation issues such as space charge, residual magnetic fields or degradation of surface potentials [224]. On the other hand, low energies directly translate to lower brightness, a handicap that can partially be compensated by optimizing the lens system geometry.

During their flight through the analyzer, the electrons with an energy lower than E_{pass} will deviate towards the inner hemisphere of the capacitor, whereas those with higher energy will lean towards the outer one. At the exit slit of the analyzer an image is created where the energy axis expands along the radial (vertical) direction, the center of the slit corresponding to the electrons whose energy is the exact E_{pass} (i.e. the nominal E_{kin}). The perpendicular (horizontal) axis in the slit defines the angular acceptance of the electron bunch, with its center point corresponding to the photoelectrons propelled in the normal direction from the sample surface.

1.2.5 Mott detector

After the energy-selected electrons pass through the analyzer, their spin polarization needs to be measured by an appropriate detector. Such a detector, called a polarimeter, works by scattering a large enough number of electrons through a spin-dependent interaction medium and observing the resulting asymmetry of that scattering process. Useful interactions for electrons include Coulomb scattering in heavy nuclei (Mott scattering), scattering with other polarized electrons (Møller scattering) or scattering with polarized

photons (Compton scattering). Additionally, the exchange interaction can be exploited in the so-called ferromagnetic detectors. Møller polarimeters constitute the main polarization monitor devices in electron accelerators, since they work best at electron beam energies in the range of 0.1 GeV to 50 GeV [54]. They make use of magnetized foils as a source of polarized electron scatterers. Similarly, Compton polarimeters are widely used to measure the polarization of circulating beams in storage rings or stretcher rings of synchrotron facilities due to their non-intercepting nature. In these detectors, a polarized laser beam is back scattered by the electrons of the beam and the returning photons experience an energy shift that strongly depends on the energy-mass ratio of the electrons. A few eV laser beam may produce a spectrum of back scattered photon energies up to several MeV [241]. However both Møller and Compton polarimeters show a reduced analyzing power at lower electron energies and become impractical for modest experimental setups that require compact arrangements. In contrast, Mott polarimeters are the most commonly used detectors for spin-resolved photoelectron spectroscopy (SRPES) and general low energy electron polarization measurements up to several hundred keV [134, 213].

The detection of electron polarization through Mott scattering was first envisioned by Sir Nevill Francis Mott in 1929, after realizing the impossibility of measuring single electron spins with a typical Stern-Gerlach apparatus [181]. He suggested that scattering unpolarized electrons through heavy nuclei would output a polarized beam for certain angles due to the spin-orbit interaction. Such a polarized beam could then undergo a second scattering that would result in an asymmetry between the left and right scattered electrons (figure 1.4). The asymmetry should be proportional to the polarization of the beam. More than a decade after Mott's idea, when Shull *et. al.* finally demonstrated the experimental scattering asymmetry for which the scientific community had been long waiting [236], the field of electron polarimetry experienced a rapid growth. Actual Mott detectors make use of the second scattering suggested in Mott's paper to measure beams that are previously polarized by other means.

The aforementioned asymmetry is typically given as the difference in electron counts between the left and right scattered beams, N_L and N_R (see figure 1.4), normalized by the total left and right counts, that is,

$$A \coloneqq \frac{N_L - N_R}{N_L + N_R} = \frac{I_L - I_R}{I_L + I_R} \tag{1.3}$$

where $I_i = eN_i/t$ are the respective left and right intensities. For a beam with polarization P coming out of the first scattering, the asymmetry after the second scattering must be proportional to it,

$$A(E, \theta_2) = PS(E, \theta_2) \Rightarrow P(E, \theta_2) = \frac{1}{S(E, \theta_2)} A \tag{1.4}$$

Here $S(E, \theta_2)$ is the so-called Sherman function, which depends on the scattering energy E and angle θ_2 (see fig. 1.4). Its precise form is given by the scattering potential seen by the electrons. For a single nucleus this would simply consist in the Coulomb potential. For atoms in a solid such as gold (the most common scattering target), the screening by atomic electrons need to be accounted for. Calculated values of S for various atoms are available in the literature [221]. In practice, though, the measured electrons may also have undergone multiple scattering inside the target and thus the effective Sherman factor needs to be established for every particular polarimeter. In the present case a value of $S_{eff} = 0.17$ was estimated by directly hitting the iron sample with an electron gun beam, measuring the polarization of the cascade electrons from iron and comparing it with literature values.

Another important parameter in the construction of a polarimeter is the scattering efficiency $\mu = I/I_0$, where I is the detected intensity after the scattering and I_0 the incident beam intensity. Reasonable scattering efficiencies usually demand a very high density of target atoms (for instance in a gold film it is in the order of $6 \times 10^{22}\,\mathrm{atoms\,cm^{-2}}$), which makes multiple scattering events almost inevitable, thereby affecting the value of S_{eff}. This implies, in practice, that a trade-off between the maximum value of S_{eff} and μ (which should both ideally approach 1) needs to be achieved. For example, higher scattering energies may result in an increase of the Sherman function but also entail a decrease in the scattering efficiency [140]. It is thus convenient to define a figure of merit $FoM = S_{eff}^2 I/I_0$, which can be proven to be inversely proportional to the square of the statistical error in an electron counting experiment of a polarization measurement. In this case the maximization of FoM results in the minimization of the error of P. However it must be noted that the statistical error is not the only parameter one has to take care of. For instance, the solid angle seen by the detector may leave out spin polarized particles that would otherwise contribute to the value of S_{eff} in an intensity-dependent way. Also the amount of electrons that go through the foil as well as amplification by inelastic scattering can affect the Sherman function. In the current detector a gold foil of 80 nm thickness has been utilized as the scattering target using a scattering energy of 50 keV. The figure of merit lies in the range $FoM \sim 10^{-5} - 10^{-4}$. This conforms to standard values for a favorable experiment [135, p. 79].

An important advantage of this Mott polarimeter is its reliability, as well as compatibility with UHV conditions. Contamination of the surface gold foil does almost no harm to the effective Sherman function, in contrast to other evaporated film targets which need to be regularly cleaned. Small variations in the scattering energy also minimally affect the value of S_{eff}. A major drawback is its low FoM value and its point-like nature as a detector when compared to alternatives with imaging capabilities. Also, the energy at which they operate makes it necessary to float the detection electronics at

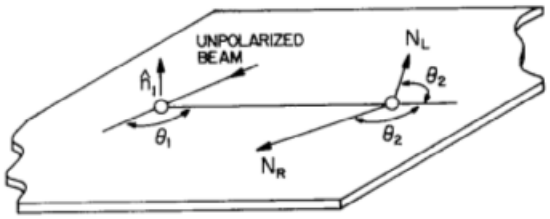

Figure 1.4: How to measure the spin of single electrons? Sir Mott proposed a double scattering process through heavy nuclei. In the first scattering an unpolarized electron beam produces a significantly polarized output in the direction $\hat{n}_1$ for large angles ($\theta_1 \gtrsim 90\,°\text{C}$). This newly polarized beam undergoes a second scattering that causes an asymmetry between the left and right scattering angles θ_2. Extracted from [87].

high voltages.

1.3 Free electron laser as probe

When measuring the magnetization in pump-probe experiments, the choice of the probe is crucial to ensure the minimum loss of information. In ferromagnetic transition metals such as Fe or Ni, for instance, the magnetization is mainly stored in the valence band (3d electrons), since their high degree of localization generates a sizable magnetic moment [250, ch. 7]. In the case of Fe this band extends over a range of 8 eV to 10 eV below the Fermi energy [47]. In addition, the work function for Fe is 4.4 eV to 5.1 eV depending on the growth direction [92]. Therefore, photons with energies of at least 15 eV need to be used for a band-integrated probing of the magnetization. Such energies correspond to the ultraviolet VUV–XUV[3] range of the spectrum (on the order of 10 nm to 100 nm wavelengths). Radiation of this type is already considered to be ionizing and is strongly absorbed by atmospheric oxygen, thereby demanding vacuum conditions. A further requirement for the probe is that pulses be in the order of 50 fs and contain a high density of photons. Several means to obtain such pulses are available to date: X-ray lasers (XRL), high-harmonic generation from infrared or visible lasers (HHG), monochromatized synchrotron radiation and free electron lasers (FEL).

XRLs typically make use of plasmas as gain mediums, which are generated by other laser beams or through electrical discharges [219]. A big handicap in this type of lasers has been their low spatial and temporal coherence due to the infeasibility of building low-loss resonators at x-ray frequencies, an issue that has recently been somewhat overcome by techniques such as

[3] Vacuum-Ultraviolet to Extreme Ultraviolet according to ISO-21348

injection seeding [271]. More importantly, their average output power has been limited by both low repetition rates of the pump lasers and low pumping efficiency [210], and the pulse lengths achievable in the XUV range are not short enough for probing many ultrafast dynamics. Respectable values on the order of 1 mJ average pulse energy (10^{14} photons per pulse) at several tenths of eV and a few Hz repetition rates have been reported [218].

Alternatively, HHG lasers focus on the optical nonlinear processes undergone by ionized light gases such as He, Ne or Ar when pumped with infrared or optical beams of sufficient intensities (frequently around $10^{13}\,\mathrm{W\,cm^{-2}}$, with some recent methods being able to bring them down to $10^{10}\,\mathrm{W\,cm^{-2}}$ [85]). HHG-generated soft x-ray and XUV light features a high degree of temporal coherence as well as short, narrow-bandwidth pulses, low divergence and jitter, and great adaptability for table-top experiments. But its low efficiency and moderate pulse energies makes these sources non-optimal in photoemission experiments when combined with the mince figures of merit of Mott detectors. Typical conversion efficiencies lie in the range of 10^{-8} to 10^{-6} and pulse energies of 60 nJ at 50 eV (i.e. 10^{6} to 10^{9} photons per pulse) can be now easily reproduced in most laboratories [219, 85].

To overcome energy limitations, intense radiation coming from storage rings in synchrotron facilities has been widely used. In a customary setup, charged particles such as electrons have their trajectories bended or circularly shaped with the help of multipole magnets, undulators or wigglers (arrangements of consecutively reversed dipole magnets). Thus accelerated, these particles start to radiate in a broad frequency spectrum that includes the XUV range and provides a considerable photon flux. In general, though, circular storage ring radiation suffers from high angular divergence and poor spatial and temporal coherence due to the particles radiating independently from one another. Also its brightness[4] scales only linearly with the number of particles, N, per bunch [113]. In contrast, free electron lasers, which can be regarded as 4th generation accelerator-based light sources, utilize longer undulators in linear accelerator (linac) setups to trigger self-amplified spontaneous emission (SASE) in electron bunches that tremendously increase both the coherence degree and the peak brightness (which scales quadratically with N) while reducing the divergence of the beams as well as the pulse duration. This method also allows for high repetition rates which can go up to several MHz with novel techniques [207]. Another great advantage of FELs is their high spectral tunability, since the emitting frequencies depend on the energy of the electron beam, which can be directly changed. All this comes, nonetheless, at the cost of intensity and time jitter between pulses, a well-known characteristic of linac FELs. Their construction costs and sizes make them also unfeasible for everyday laboratories and the experiments

[4] Flux of photons in a certain spectral bandwidth emitted per unit surface and solid angle

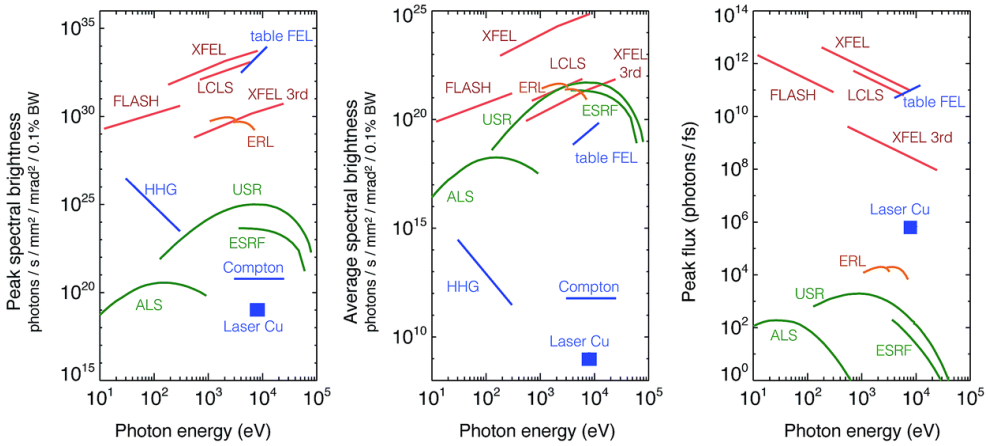

Figure 1.5: Comparison of peak brightness, average brightness and peak flux vs photon energy for different x-ray sources. In red the FEL types FLASH (Hamburg, Germany), LCLS (Standford, USA), XFEL (operational in 2016 in Hamburg, Germany) and ERL (Energy Recovery Linac); in green the synchrotron types USR (Ultimate Storage Ring concept [33]), ALS (Berkeley, USA) and ESRF (Grenoble, France); in blue other sources such as tabletop FELs [95], HHG-based sources, Compton scattering or the laser-driven plasma source with Cu target at Max-Born Institut (Berlin, Germany) [287]. Extracted from [49].

become highly time-constrained due to the increasing demand of their facilities. Although comparisons of only main parameters are inaccurate to rate the convenience of every source, figure 1.5 shows peak and average brightnesses as well as photon flux for different x-ray sources as a function of the photon energy. Clearly, FEL sources are above all others in terms of brightness and photon flux, with a remarkable five to eight order increase in peak brightness. All in all, FEL light shows up as an appealing choice for probing in photoemission experiments.

1.3.1 Principle of operation

The most distinctive feature of FELs when compared to common lasers is their lack of active medium. In fact, radiation in the XUV is strongly absorbed in most materials, with penetration depths of typically less than 1 µm. Reflection on optical surfaces in this range is close to zero under normal incidence, and the technique of Bragg reflection on natural crystals is unpractical due to the wavelengths being still too large[5]. These proper-

[5]However notorious progress has been made in the last years. For instance, synthetic diamond crystals have been reported to achieve near 100 % reflection under normal incidence [237].

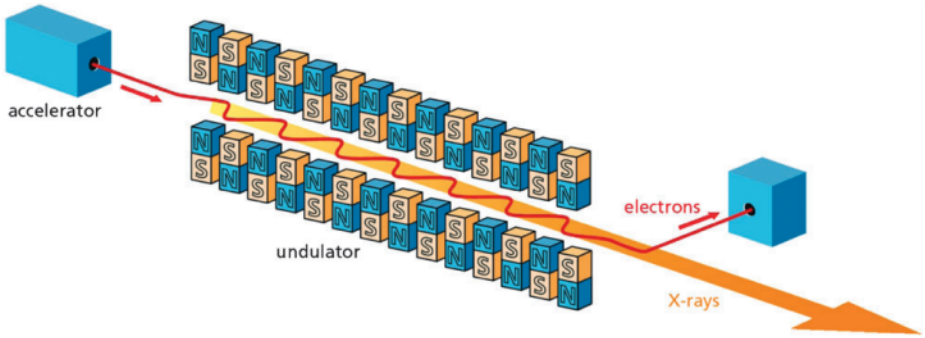

Figure 1.6: In a FEL, bunches of electrons are brought to relativistic speeds along linear accelerators. Then, an undulator, consisting of a periodic arrangement of magnets in alternate polarities, exerts an acceleration to the electrons in the transverse direction of propagation, thereby causing coherent emission of radiation whose wavelength depends on the energy of the electrons as well as the undulator design. Extracted from [194].

ties have restricted the use of both solid state materials as active mediums and mirror-based resonant cavities for amplification. An alternative to solid state mediums consists of multicharged ions. It is known that electronic transitions between "optical" levels in some elements are shifted to the XUV range when their atoms are heavily ionized [122]. However, the generation of such ionized states can only be found in plasmas, which require considerably high pumping power. Thus, the need for mediumless, intense coherent XUV radiation inspired the natural evolution of synchrotron technologies to provide the FEL concept.

In order to operate an FEL two fundamental elements are needed. An accelerator that provides relativistic bunches of electrons and an undulator as the lasing mechanism. In an undulator, a periodic arrangement of magnets with alternating polarities makes the incoming electrons follow an oscillatory path in the transverse direction of propagation (fig. 1.6). As the Lorenz force from the magnets acts on the electrons, an acceleration is produced that generates narrow-band radiation in an also narrow angular cone around the undulator axis (two distinctive features of undulators when compared to the broader-band, higher divergence radiation created in bending magnets from common synchrotrons). The central wavelength of the so-created radiation can be roughly estimated as follows. Let λ_u be the period of the undulator (the distance between two consecutive magnets of the same polarity). From the perspective of the moving electrons the period of the undulator is contracted by the relativistic Lorenz factor γ, that is, $\lambda_u^* = \lambda_u/\gamma$. The electrons will then radiate at the corresponding frequency ω_u^*. From the perspective of

the laboratory frame, however, such radiation is strongly blue-shifted due to the relativistic Doppler effect. Therefore, the wavelength in that frame $\lambda_l = \lambda_u^* \sqrt{\frac{1-\beta}{1+\beta}} \approx \lambda_u^*/(2\gamma) = \lambda_u/(2\gamma^2)$, where $\beta = v/c$ is positive for an approaching source. The last approximation holds for highly relativistic electrons. This is the case for FELs, where electrons are accelerated at several MeV (for instance $\beta = 0.993$ at 4 MeV). This calculation can be refined when the sinusoidal path of the electrons in the undulator is taken into account, which affects their actual longitudinal velocity. The formula then becomes

$$\lambda_l = \frac{\lambda_u}{2\gamma^2}\left(1 + \frac{K^2}{2}\right), \quad \text{with} \quad K = \frac{eB_0\lambda_u}{2\pi m_e c} \tag{1.5}$$

where B_0 is the peak magnetic field on the undulator axis and m_e the rest mass of the electron [233]. The quantity K is called the *undulator parameter* and lies usually in the range 1 to 3 ($K = 0.934 \times B_0[\mathrm{T}] \times \lambda_u[\mathrm{cm}]$). From equation 1.5 one can immediately see that the radiation wavelength is changed either through the electron energy $E = m\gamma c^2$ or through the undulator parameter by modifying B_0 or λ_u. The former is most commonly used since the construction of large undulators with variable gaps is a rather challenging task (although next generation sources such as the planned LCLS2, FLASH2 or the newly operative XFEL have made substantial progress in this area). Note also that λ_l in 1.5 refers to the fundamental harmonic only. This is important because this harmonic features a narrow bandwidth, which is inversely proportional to the number of undulator periods N_u (i.e. $\Delta\omega \approx \omega_l/N_u$). It is also tightly collimated, with an angular aperture dependent on N_u aswell, $\sigma_\theta \approx 1/(\gamma\sqrt{N_u})$. Of course, the total received radiation includes higher harmonics whose distribution depends on the angle of detection from the undulator axis. It can be shown that in the forward direction ($\theta = 0$) only the odd harmonics contribute to the total radiated power [6], that is, $\lambda_m = \lambda_l/m, \quad m = 1, 3, 5...$ [233]. Indeed, radiation in the off-axis direction includes both odd and even harmonics, and, once integrated over all frequencies and solid angles, it results in a total radiated power equivalent to the synchrotron radiation power from a bending magnet with a magnetic field $B = B_0/\sqrt{2}$ (the factor $\sqrt{2}$ being due to the sinusoidal nature of the electron path in the undulator). Thus, in terms of radiation power both devices, bending magnets and undulators, produce similar outputs. However, the spectral power distribution is concentrated near the working wavelength in the latter case, thus providing more power for the corresponding energy. Additionally, only undulators allow the generation of coherent radiation (lasing).

[6] Interestingly, the ratio U_m/U_1 at which the spectral energy density of each successive harmonic decays respect to the fundamental does only depend on the harmonic number m and the undulator parameter K, but neither on the electron energy nor on the undulator period λ_u.

In the infrared and visible ranges, lasing in an FEL is easily achieved through an optical resonator. The electron bunch is directed through the undulator in a periodic manner (for instance using a storage ring) and the radiation obtained is amplified in an optical cavity comprised of two high-reflective mirrors. Care must be taken that the phase of the radiation be synchronized with that of the sinusoidal movement of the electrons inside the undulator for the amplification to prevail. In the XUV and x-ray regions, though, the attempts to build a suitable resonator have been to date unsuccessful, as stated before. In this case, the lasing has to be implemented in a single pass of the electron bunch through the undulator. Undoubtedly, a longer undulator needs to be used to compensate for the lack of multipass amplification. During the motion in the undulator, and under the proper conditions, the growth of the (coherent) radiation intensity also affects the electron bunch. Since the wavelength of this radiation is smaller than the size of the bunch, its oscillating electric field tends to slice the bunch into smaller chunks. The reason for this effect, called *micro-bunching*, can be found through a detailed analysis of the energy transfer mechanism [233, ch. 5.6]. Basically, electrons that are transferring energy to the electric field (i.e. whose transverse velocity is parallel to the field) have sinusoidal paths with larger amplitudes than those that are gaining energy from the field. This creates a modulation of the longitudinal velocity that brings electrons together near the areas of maximum energy transfer. Micro-bunching is thus the end result of a coherent self-amplification process involving the radiation emitted from the accelerated electrons and the electrons themselves. The acronym SASE for Self-Amplified Spontaneous Emission has been coined to describe such processes.

Certainly, a SASE process cannot grow indefinitely, and saturation is typically reached after a few meters of propagation inside the undulator [71]. Consequently, customary undulator lengths are on the order of 10 m to 100 m. It is also important to note that although the SASE mechanism can be initiated by spontaneous emission from vacuum fluctuations inside the electron bunch, FELs can also be seeded by separated laser beams, which are focused in the area comprising the first few gain lengths[7] of the undulator, where the FEL gain process is most delicate. Seeding substantially reduces energy fluctuations that typically occur in a stochastically initiated process such as SASE. It also improves the longitudinal coherence that SASE poorly achieves after saturation due to the micro-bunching effect starting independently at different parts of the bunch. In fact, seeding facilitates saturation in faster times than with SASE, which allows for shorter undulator lengths. Furthermore, the (femtosecond) temporal jitter originating in the random

[7] In a SASE-driven FEL the intensitiy of the radiation grows exponentially as $I = I_0 \exp(x/L_g)$, where L_g is termed the *gain length*. Typical values are between 0.5 m to 5 m [233, 71].

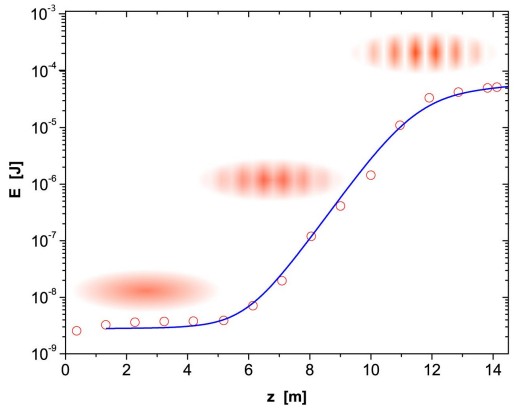

Figure 1.7: During its flight through the undulator, the electron bunch interacts with the radiation emitted by itself. Under the proper conditions, such an interaction can coherently amplify the radiation field in an exponential manner, giving place to the phenomenon of micro-bunching. After the micro-bunching is complete the system reaches saturation and the radiation energy can no longer grow. Extracted from [233] with data from [13] obtained in the SASE FEL of the TESLA Test Facility in DESY (Hamburg, Germany). The electron energy was 240 MeV to 250 MeV and the radiation wavelength 98 nm.

structure of the FEL pulses is minimized, the spectral bandwidth severely narrowed down and the resulting fundamental intensity increased by a few orders of magnitude [156].

As an alternative to seeding, the micro-bunching can be kick-started by a periodic charge density modulation in the beam current. This is achieved through special modulators before the bunch reaches the undulator. Both approaches are in fact physically equivalent and might be used simultaneously.

1.3.2 FLASH FEL at Hamburg

In 1992 an international collaboration for the development of Superconducting Radio-Frequency (SRF) acceleration technology and related accelerator studies was born under the name of TESLA (TeV-Energy Superconducting Linear Accelerator) Collaboration. This project aimed to build an electron-positron linear accelerator up to energies of 800 GeV with superconducting radio-frequency cavities for the study of high-energy particle physics beyond the limitations of former accelerators [215]. For this purpose, a test facility was constructed in the Deutsches Elektronen Synchrotron (DESY)

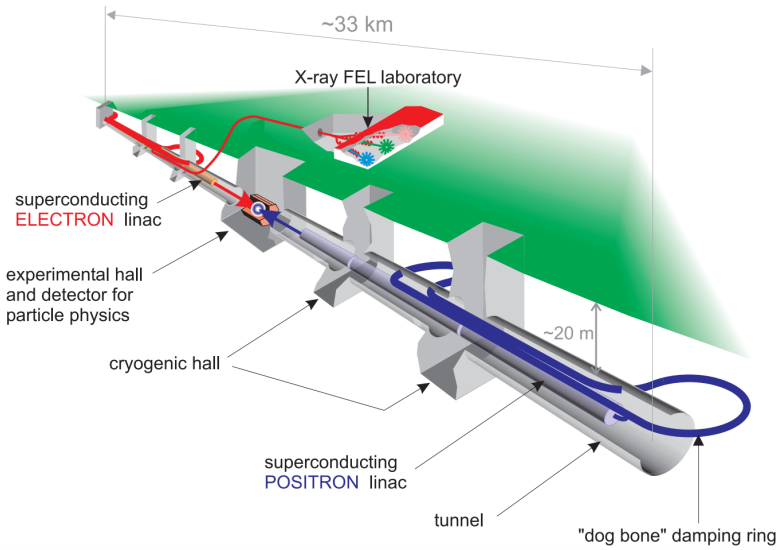

Figure 1.8: The early concept of the TESLA electron-positron collider with the attached, non-interfering x-ray FEL. Reprinted from [215].

in Hamburg, Germany, to investigate whether the high beam quality and performance needed in a collider could be achieved with the new SRF technology. In the initial design it was also envisaged the integration of an x-ray FEL source that would make use of the linear collider installation in a non-interfering manner [36, 222]. It was initially baptized as VUV-FEL and later as FLASH (Free electron LASer in Hamburg). FLASH would consist of a linac module, an undulator and a user facility with five separate beamlines adapted for a variety of experiments. In September 2001, SASE saturation was reached for the first time at a wavelength range of 95 nm to 105 nm, producing ultrashort pulses of 30 fs to 100 fs and raising FLASH to the worldwide first VUV FEL in operation [13]. In August 2005 operation at a wavelength of 32 nm with 25 fs FWHM pulses was achieved [14]. In 2007 a wavelength of 13.7 nm with 10 fs FWHM pulses was reported, including a 5th harmonic at 2.75 nm lying deep into the water window[8] [2]. Average pulse energies reached 25 µJ and peak brilliances went up to 5×10^{29} photon/s/mrad^2/mm^2/0 1% bandwidth for the first harmonic during this run period [1].

The FLASH FEL generates electron bunches from a laser-driven Cs_2Te photocatode assembled in the rear part of a normal-conducting 1.6–cell RF copper cavity operating at 1.3 GHz klystron-powered field frequency. The photoca-

[8]The region in the x-ray spectrum between the K-absorption edge of oxygen at 2.34 nm (or 530 eV) and the K-absorption edge of carbon at 4.4 nm (or 280 eV). Since water is transparent to x-rays of such energies, this window is of special interest for the study of *in vitro* (and possibly *in vivo*) biological samples.

tode is illuminated with a UV laser sending 10 ps to 20 ps long pulses at wavelengths of 260 nm to 270 nm [274]. With a quantum efficiency of 5 % to 10 %, electron bunches with charges up to 3 nC separated each other by 1 µs and forming pulse trains of up to 800 pulses are produced under such conditions with a (macro-bunch) repetition rate of 10 Hz. In order to avoid space charge effects fairly low currents of 30 A are required for the bunches, which need to be nonetheless immediately accelerated at relativistic energies of up to 7 MeV. In this regime, the attraction generated by the magnetic forces arising from parallel high currents overcomes the electric repulsion from the electrons. Further details on the FLASH electron RF gun can be found in [233, 151, 256].

After electron injection and initial boost of the bunch, the acceleration modules come into play. There are seven 12.2 m long modules comprised of eight superconducting RF 9-cell cavities each (fig. 1.9). The cavities are build with pure niobium, at present the most efficient material for cavity accelerators (fig. 1.10), and cooled with superfluid He at 2 K to attain the desired superconducting properties [12]. The first module accelerates the electrons from the injection energy of 5 MeV–7 MeV to 130 MeV (see fig. 1.9). Before the kinetic energy can be further increased a longitudinal compression of the bunch is needed to augment the modest peak currents delivered by the injector, as previously mentioned. This is achieved in a two-step process. First, an energy slope is imprinted in the electron bunch during its path through the accelerator module. Ideally the bunches are accelerated during the falling slope of the RF voltage in the cavity, however, due to their finite length, they experience a varying field that translates into an energy gradient throughout the bunch. Such a gradient can be considerably non-linear given the cosine-like nature of the RF field. It is desirable to avoid non-linearities of this type for a proper bunch compression. For this reason a third harmonic SCRF cavity working at 3.9 GHz was installed in 2010 that makes the energy deviation of the bunch become a linear function of the propagation axis [80, 266]. The so-prepared bunches are then lead to a magnetic chicane, a 4-dipole arrangement that deviates electrons off the accelerator axis and back on again in a degree that is dependent on the energy of the particle (D-chicane in fig. 1.9). Thus, trailing electrons in the bunch with higher energies deviate further and catch up with lower energy ones in the front, which travel a shorter path through the chicane (fig. 1.11). Without a third harmonic SCRF cavity for correction, the resulting compressed bunch exhibits a long tail extending several ps after the leading peak, which can be well below 100 fs in length and contains 10 % to 20 % of the total charge in the bunch [80, 220]. Once corrected for, bunch-compressed peak current amplitudes on the order of 100 A are reached. However, before the desired kA amplitudes for lasing can be achieved, an additional two-module accelerator line is interposed, which raises the energy of the bunch to 450 MeV, and

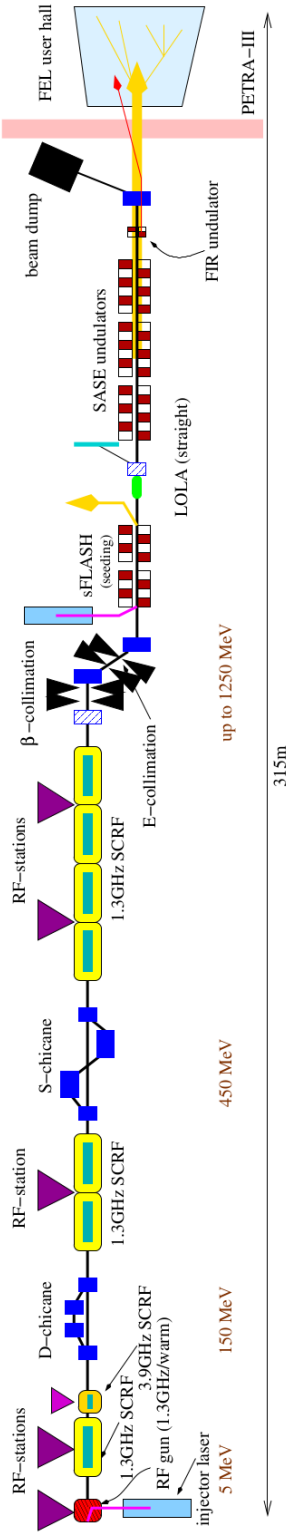

Figure 1.9: Schematics of the FLASH experiment in DESY. Reprinted from [267].

Figure 1.10: Superconducting 1.3 GHz 9-cell cavities designed for the TESLA Test Facility and used for FLASH in Hamburg, Germany. Reprinted from [12].

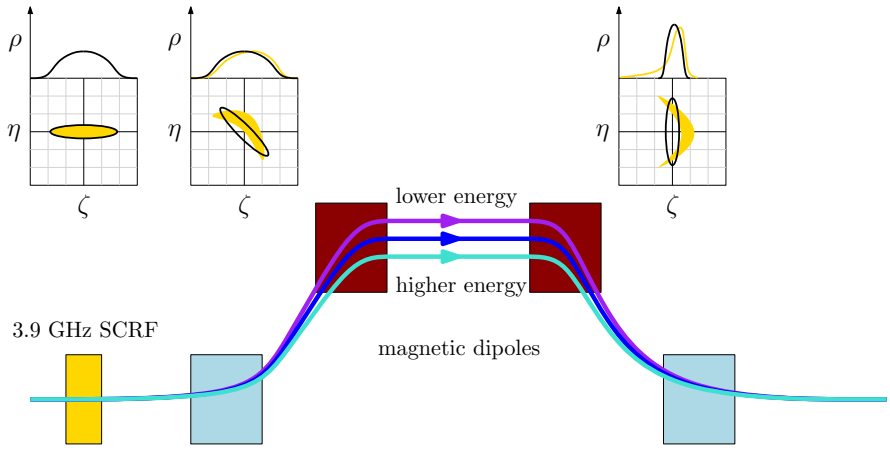

Figure 1.11: Schematic concept of the magnetic chicane at FLASH. Electrons in the bunch with higher energies (cian line) travel a shorter path than those with lower energies (purple line), resulting in a bunch compression. The plots above represent the electron charge distribution density ρ according to the relative energy deviation η and the longitudinal position ζ along the bunch axis. Such distribution must be conserved under ideal conditions after Liouville's theorem. Due to the non-linearity introduced by the cosine-like nature of the RF signal in the accelerator cavity, a deviation of the desired shape appears, which affects the compression efficacy of the chicane (gold-shaded areas). For this reason an extra SCRF third harmonic cavity is installed before the first chicane dipole which linearizes the energy slope and favors proper bunch compression.

a second compression stage is installed through an S-shaped chicane (see fig. 1.9), which delivers the optimally compressed bunches. The reason for a two-stage compression lies in the trade-off between the instabilities that high currents generate at moderate energies and the low compression ratios accessible at higher energies.

During the acceleration and compression stages several diagnostic devices have been installed to monitor the longitudinal and transverse electron beam distributions as well as timing and synchronization issues. For instance, a Transversely Deflecting Microwave Structure (TDS) has been used to capture single-bunch longitudinal profiles as well as slice emittances[9] by applying a vertical RF kick to the bunches that translates into a linear correlation between time and vertical position, a technique commonly referred to as *streaking* [117, 220]. Standard Optical Transition Radiation (OTR) detectors take advantage of the radiation expelled by relativistic electrons when crossing the interface between two media with different refraction indexes to retrieve information on the longitudinal phase space distribution of the bunches [220]. For emittance measurements in the transverse plane, view screens such as polished aluminum-coated silicon discs or thin Ce:YAG scintillator crystals are placed to intercept the beam at relevant points of the linac. With the help of CCD cameras the average emittance and other important beam properties can be reconstructed after variation of the focusing parameters. Further details for this method are provided in [166, 28]. To measure slice emittance of a part of the bunch (for instance the part entailing the peak intensity suitable for lasing) streaking techniques such as the previously described TDS are required.

Of special relevance for this work are timing and jitter measurements. Here, electro-optical sampling (EOS) methods can be employed in different layouts to spatially encode the electron beam profile into an infrared laser pulse (usually from a titanium-sapphire oscillator) when the former traverses a birefringent crystal such as GaP or ZnTe. The crystal is placed only a few millimeters far from the electron beam so that the polarization of the transient electric field exuded from the bunch, which lies on the THz range, is still approximately linear. The THz field changes the birefringence of the crystal according to the bunch distribution while the synchronized, phase-locked laser pulse experiments a change in its polarization ellipticity, which can be read out as an intensity value by a photodetector. If the laser pulses are narrow, a delay stage can be set that performs a scan along the bunch length [246, p. 46]. However due to the inherent time jitter of near 50 fs in the FEL, analysis of sub-100-fs bunches are barely attainable. For single-bunch measurements the delay stage can be substituted by a dispersive crystal that stretches (*chirps*) the laser pulse to a duration longer than that of the electron bunch. In this case the spectrum of the pulse already contains the information from each part of the bunch, which can be obtained through a CCD camera preceded by a diffraction grating. This technique, known

[9] Emittance can be roughly defined as the area enclosing the particle beam distribution when represented in the position-momentum phase-space. It is a property of the beam which characterizes its size, with the attribute that it remains constant in the absence of dissipative or cooling forces.

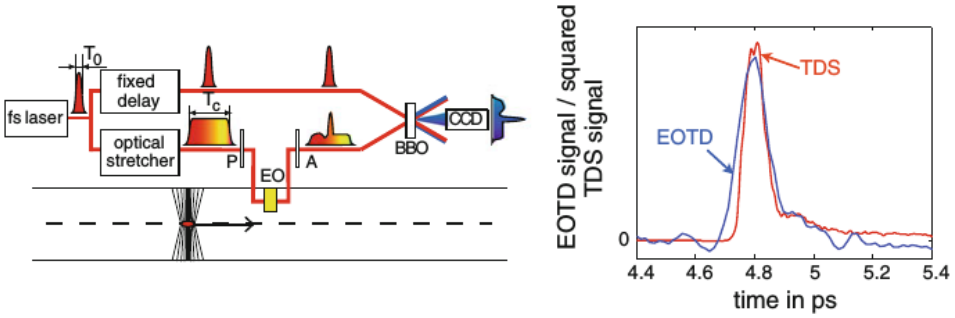

Figure 1.12: The concept of electro-optic time decoding (EOTD) implemented at FLASH. Electro-optic spectral decoding (EOSD) does not include the additional narrow pulse and BBO crystal, relying only on the information imprinted in the spectrum of the stretched pulse. The retrieved bunch profile is in agreement with measurements from the transversely deflecting microwave structure (TDS) method referred to in the text. Reprinted from [233].

as electro-optic spectral decoding (EOSD) has a resolution of 100 fs and can still be improved by a factor of two by using a secondary, non-stretched laser pulse and a non-linear crystal in the so-called electro-optic temporal decoding (EOTD), as further revealed in [246, 28]. In fig. 1.12 a sketch of this last method is presented.

A novel technique using electro-optical modulation (EOM) has been also implemented in FLASH, which is referred to as the beam arrival monitor (BAM). In this setup reference pulses from an erbium-doped soliton fiber laser are fed into a commercially available $LiNBO_3$-based electro-optical modulator. The phase of the laser pulse in each branch of the modulator is shifted by the interaction of an rf signal indicating the arrival time of the electron bunch. Such a signal is generated by induction from the electron beam through a pick-up electrode in the form of a thin metal ring that is placed after the accelerator cavities and near the beam. The phase shift inside the modulator is translated into an amplitude change in the output, which is measured by a photodetector. With this detection scheme, pulse-to-pulse time jitter can be measured with resolutions down to 6 fs, as reported in [167].

After the last acceleration cavities, the electron beam is ready for lasing under the SASE mechanism which the undulators provide. For the SASE process to take place a considerably long undulator section is required (fig. 1.9). FLASH incorporates six 4.5 m long undulator modules, each comprising a periodically arranged set of NdFeB magnets with a fixed gap of 12 mm between each and a total period of 27.3 mm. With a K-value of 1.23 and mag-

netic field peaks of 0.48 T, the undulator delivers 10 fs–50 fs pulses in the wavelength range of 6.9 nm–47 nm (2.3 nm and 1.4 nm for the 3rd and 5th harmonic, respectively). Average pulse energies vary from 10 µJ to 50 µJ, with peak powers of several GW.

1.3.3 Timing and synchronization

Of utmost importance, particularly for the end users of FLASH, is the time monitoring and synchronization design that provide the necessary information for data analysis in time-resolved experiments such as those making use of pump-probe setups. Traditional timing designs in accelerators involve the distribution of RF signals through coaxial cables with lengths of several hundred meters. However, for these lengths temperature rises of only 0.1 °C might translate into time delays of 100 fs due to thermal expansion or contraction of the cables. Such delays are clearly not acceptable when dealing with pulse time resolutions on the order of 10 fs. Attenuation is another handicap of coaxial cables. being both high and frequency-dependent. For instance, at 1.3 GHz values nearing 50 $\mathrm{dB\,km^{-1}}$ are common for many commercial products [58]. An alternative are glass-fiber cables, which show low, frequency-independent attenuation, excellent electromagnetic interference protection and reduced cost, yet exhibit similar thermal coefficients to their coaxial counterparts. Since fiber links are devised for point-to-point operation, though, the amount of links required for systems as complex as FLASH raises the costs to prohibitive amounts. All in all, a mixed signal distribution architecture was chosen for FLASH, comprising small, local sections based on coaxial cabling supplied by long, phase-stabilized optical fiber links [58, 137].

The timing mechanism in FLASH starts at the master oscillator (MO). This entails a 9 MHz oven-controlled quartz crystal (OCXO) phase-locked to a 81 MHz voltage-controlled crystal (VCXO) for optimal frequency stability. The 81 MHz signal is then divided, multiplied and conveniently amplified to deliver all required frequencies in the facility, among which 1.3 GHz, for accelerator cavity operation, is the most relevant (see fig. 1.13). Additionally, an optical link synchronized with the MO supplies infrared pulses to the FEL sections. These optical pulses are used either to drive RF signals, synchronize other external lasers (by optical cross-correlation or seeding), or to operate monitoring devices such as the BAMs.

The time emission pattern of the FEL depends fundamentally on the driving laser that triggers the photoinjection at the rf electron gun and is limited by the accelerator capabilities. An important advantage of superconducting linacs like FLASH is their acceleration efficiency even at high duty cycles. For this reason, bunch trains of up to 800 µs in length containing several hundreds to thousands of single pulses can be delivered by the driving laser

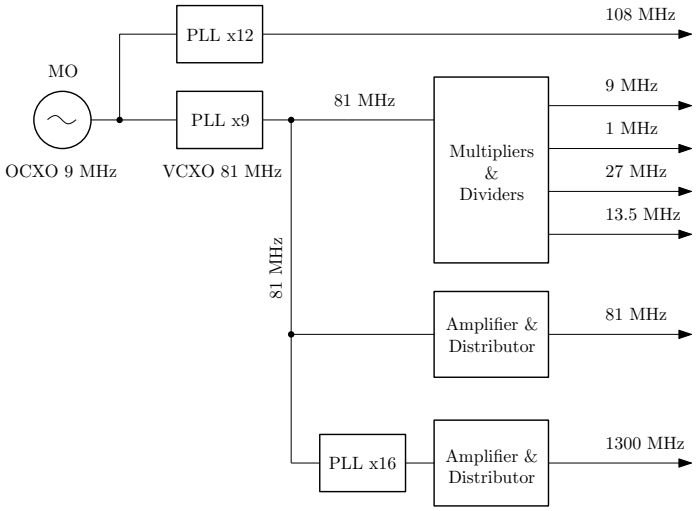

Figure 1.13: The master oscillator (MO), situated in an acclimatized hut near the injector area, uses a 9 MHz oven-controlled oscillator (OCXO) that is driven through a phase-locked loop (PLL) to generate optimally stable frequencies such as 81 MHz. Multiples of the latter frequency can afterward be obtained according to the device requirements. Some of these frequencies are used for the pump-probe synchronization at the end-user facility. Adapted from [240].

with a repetition rate of up to 10 Hz in the so-called burst mode [274]. Evidently, the pump laser will at least partly inherit such performance demands. In the experiment presented here, each burst from the FEL contains 30 pulses of 100 fs length separated by intervals of 10 µs (100 kHz). The bursts are 100 ms apart, i.e, with a repetition rate of 10 Hz. The pump laser has the same burst-mode structure, although the single pulses are slightly longer (130 fs). However, for experimental purposes it is necessary that measurements be taken with both only the FEL pulses and only the pump pulses, as well as a dark background measurement for offset subtraction, in order to conveniently normalize the effect. For this reason, a measurement cycle structure of four sets of 15 pulses has been set up (see fig. 1.14) whereby the first set comprises only EUV light, the second set incorporates the pump laser to the present EUV and the third set switches off the FEL but maintains the pump. The last set is left for the dark measurement. In this way, the Mott detector outputs a series of voltage signals for each set (V_{FEL},V_{sig},V_{ref} and V_{DC}) that are used to retrieve the signal for the computation of the asymmetry. The magnetization direction of the sample is triggered by the pulser described in section 1.2.3 synchronized to the 10 Hz repetition rate of the lasers. Thus, each measurement cycle is undertaken with a definite magnetization direction (*up* or *down*). Additionally, a delay stage is permanently

shifting the pump beam with respect to the EUV within a fixed range. Since the movement is continuous, a delay encoder stores the delay value per pulse, leaving the corresponding data sorting to off-line post-processing.

From the master oscillator, signals at 9 MHz, 108 MHz and 1.3 GHz are sent through 300 m-long coaxial cables to the experimental hall of the end-user facilities at FLASH (fig. 1.15). These frequencies are used to synchronize the optical laser that serves as a pump to the five beamlines available (fig. 1.15). The laser hutch seen in the picture hosts a titanium-sapphire (Ti:Sa) oscillator operating at 800 nm whose 12th repetition rate harmonic (1.3 GHz) is phase-locked to the master oscillator with an accuracy higher than 70 fs rms, although other instabilities sum up to a total jitter of nearly 250 fs rms [211]. From this point either a burst-mode µJ-amplifier at MHz repetition rate or a single-pulse mJ-amplifier at 10 Hz can be selected for pump delivery to the beamlines, depending on the power and timing requirements of the experiment. In any case, since the time jitter is still of considerable magnitude compared to the usually needed accuracy of most pump-probe measurements, an approach has been taken whereby the jitter itself is recorded during the measurement time and stored for shot-by-shot jitter correction during post-processing of the data.

The time jitter measurement scheme used for this work was the beam arrival monitor (BAM) described in section 1.3.2. The repetition rate of the driving fiber laser is locked to the 6th harmonic of the 1.3 GHz signal coming from the MO (i.e. 216.7 MHz). The distribution of these sub-100 fs long infrared pulses along the accelerator section requires dispersion compensated optical fiber links stabilized by piezoelectric fiber stretchers. These operate after a feedback loop system consisting in cross-correlating the incoming laser pulses in the fiber with the reflected ones at the end of the link. The sum-frequency signal from this correlation can detect time fluctuations with femtosecond precision and drive the piezo-stretchers for correction [167]. One of the pulses out of the pulse train delivered by the laser is used as a reference by synchronizing it with the zero point of the electron beam pickup signal, which corresponds to zero modulation (middle point of the slope showed in fig. 1.16). When the electron beam experiences a time delay the pickup signal shifts and effects a modulation to the amplitude of the reference pulse. This amplitude can be compared with the amplitude of the adjacent pulses from the train and the corresponding delay can be deduced with high accuracy (fig. 1.16). Two BAMs were installed in FLASH, at the beginning and at the end of the second accelerator section. The first BAM is used to feed the time fluctuations back to the first accelerator module, producing a decrease in the jitter along bunch trains of roughly 25 % to 40 %. With such a setup, a stable arrival-time jitter of around 25 fs could be established in the best case scenario [165], with an unprecedented resolution of 6 fs, as mentioned above.

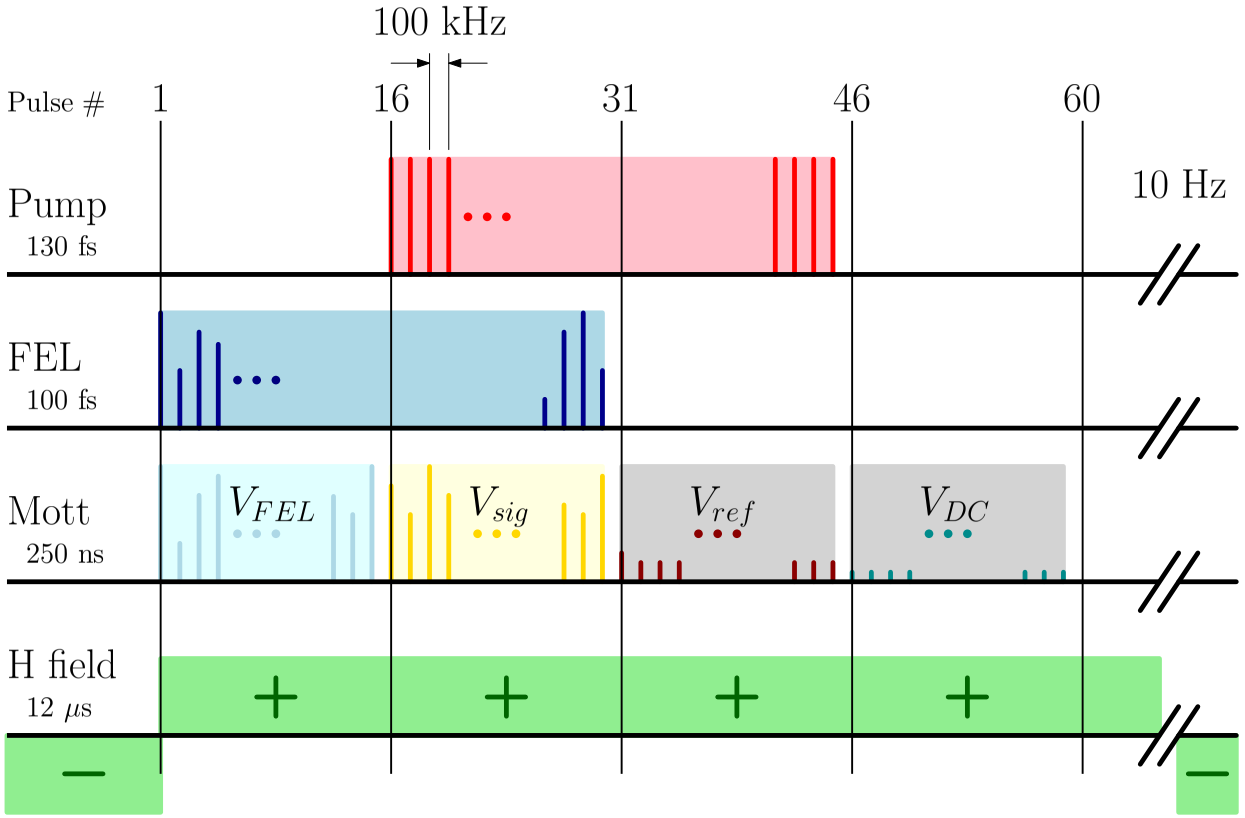

Figure 1.14: Timing pattern of the experiment at FLASH. Both the pump and the FEL deliver 30-pulse bursts with a repetition rate of 10 Hz. Each complete measurement consists of four groups of 15 pulses. The first set involves the EUV light only, whereas the second set incorporates the pump. This second set contains the desired signal for the retrieval of the demagnetization that is measured by the Mott detector as a voltage V_{sig}. The third set comprises only the pump laser to serve as a reference signal V_{ref}. The final set has no light and translates into an offset DC signal from the Mott detector. Each of these bursts is measured for a magnetizing field direction (+,−).

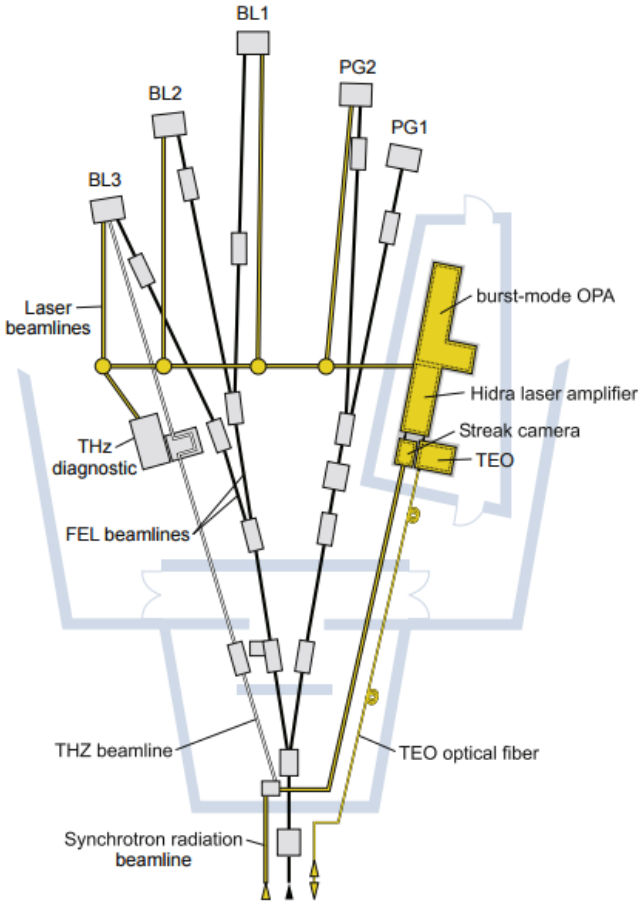

Figure 1.15: The experimental hall of FLASH1 facility. In the laser hutch the setup for pump delivery is depicted, as well as the monitoring devices for pump-probe drift and jitter recording. Reprinted from [211].

Besides the fast random fluctuations between the optical laser and the FEL pulses, slow drifts on the order of $1\,\mathrm{ps\,h^{-1}}$ arise in the accelerator. Such deviations are monitored by a streak camera located in the laser hutch. Streak cameras have the best time resolution among other instruments which directly detect ultra-fast light phenomena. They also feature a wide measurement range, which extends from the infrared to the x-ray part of the spectrum, making them adequate for mixed input signals such as the laser and the EUV. Their operational principle is simple (fig. 1.17). Light transients are directed through optics into a photocathode that generates electrons which travel along a vacuum streak tube. Inside the tube a pair of sweeping electrodes accelerate the electrons off the axis depending on their arrival time and position. The so deviated electrons are then multiplied by a

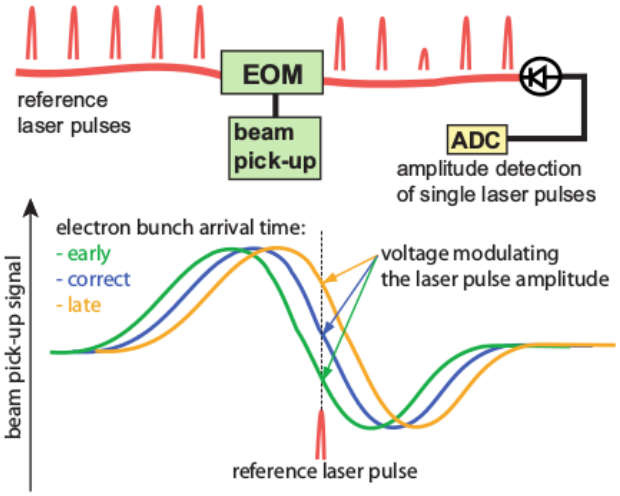

Figure 1.16: Principle of the beam arrival monitor detection. A reference pulse from the train is sampled to the zero crossing of the beam pickup signal inside the EOM. It then undergoes an amplitude modulation when the signal arrives with a certain delay, whose value can be derived from such a modulation. Reprinted from [165].

micro-channel plate (MCP) before hitting a phosphor screen that produces a 2-dimensional image with time and position as the main axes, as well as an intensity profile. Although streak cameras are suited for single shot operation, when working in synchroscan mode time-averaged measurements can help increase their resolution. Their high sensitivity, which can reach even single photoelectron detection, allows for parasitic monitoring of the time jitter in FLASH during measurement time. Finally, streak cameras have the advantage over BAMs that the pump-probe overlap can be simultaneously measured. In the present work, a small fraction, around 10^{-6}, of the optical pulse generated in the fs-laser is transported to the camera to serve as a marker for the arrival time of the pump. A reference pulse from the FEL is also needed to compare it with the arrival times of the laser and determine the jitter. Such a pulse is produced from the dipole radiation generated when the electron bunches are deflected with a dipole magnet after passing the undulator section. The duration of these pulses is approximately equal to the electron bunch length, i.e., below 100 fs and, since its generation occurs right after the undulator section, its timing is naturally synchronized with the EUV pulses that will be used in the experimental hall. This light needs to be guided by a dedicated 55 m long beamline into the laser hutch and focused on the slit of the streak camera. Due to the broadband nature of

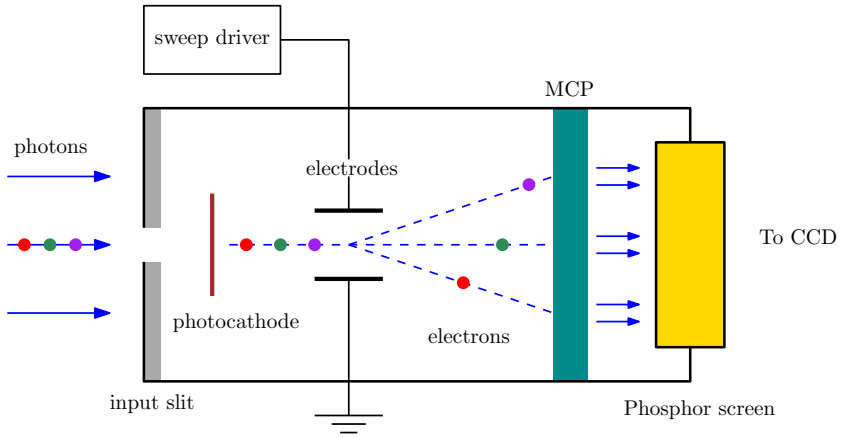

Figure 1.17: Operation principle of a streak camera. Photons are focused to the entrance slit and converted into electrons by a photocathode. Traveling along the streak tube these electrons are then deviated by a sweeping field, which spatially spreads them according to their arrival time. After proper MCP amplification, a phosphor screen reconverts them to a visible image that can be recorded for processing.

the dipole radiation[10], dispersion effects in the focusing system of the streak camera are considerable, and the pulses can lengthen to more than 10 ps. With proper analysis, though, tracking of the peak positions of the pulses in the streak camera can be determined with resolutions down to 400 fs rms, well below the nominal 2 ps resolution of the streak camera [208]. With this method time drifts of 800 fs have been reported over a measurement period of 11 h.

Both fast and slow jitter measurement techniques described above have their detection devices still far away from the actual experimental end-stations. BAMs, for instance, need their EOMs placed in the accelerator sections and close to the electron path, whereas the streak camera, located in the laser hutch by the experimental hall, can still be up to 20 m away depending on the chosen measurement beamline. Therefore, a method to evaluate the time difference and spatial overlap of the EUV and pump pulses at the interaction point of the experimental set-up would be of great value. A suited technique for this purpose is x-ray induced transient optical reflectivity on a GaAs surface [84]. In the used arrangement, both the laser pump and the EUV beams are overlapped onto a GaAs thin surface oriented at an angle of 41.5° with respect to the axis of incidence. The reflected component of the laser pump is then measured with a fast photodiode. In this case, the EUV pulses are absorbed by the GaAs, which triggers valence band excitations that induce a change in the material reflectivity, $\Delta R/R$. By using a delay

[10] commonly referred to as *white* dipole radiation

stage a scan can be made to reconstruct $\Delta R/R$ over timescales ranging from a few femtoseconds to many hundreds of picoseconds. This method doesn't allow for shot-to-shot detection, but it is of lower complexity than those designed for this purpose [169]. To record the time jitter several scans with the same time range are performed. For each delay the variation of $\Delta R/R$ can be translated into a time fluctuation. In the present experiment, though, this technique was only used to find the time overlap between the probe and the pump.

At this point it is worth mentioning how the monitoring of a relevant parameter such as the EUV beam intensity is undertaken. A minimally invasive measurement of the intensity for each individual pulse in the pulse train is obtained with an x-ray gas monitor detector (GMD) as detailed in [255]. In the employed GMD, electrons and ions generated by photoionization of a light gas (nitrogen or rare gases) at very low pressures (around 10^{-6} mbar) are collected by a pair of Faraday cups under the influence of an homogeneous static electric field. The resulting electron and ion currents can be detected in a pulse-to-pulse basis, but also the ion signal can be read out with a longer integration time (up to 20 s). The number of photons for each shot can be deduced from the ion/electron signal with an accuracy of 10 %. A pair of such detectors is placed at the end of the accelerator tunnel and another pair at the beginning of the experimental hall. In between, a krypton gas attenuator also provides intensity modulation without the need to change the FEL parameters. Further attenuation of the EUV beam is also achieved at the entrance of the experimental hall through a series of metal films of different thicknesses and materials. Although FLASH operates at typical average pulse energies of 10 µJ–50 µJ and up to 170 µJ peak energies, values as low as 10^{-4} µJ have been measured during the beamtime presented here.

1.4 Space charge and the loss of polarization

In this section data from the FLASH experiments will be briefly outlined and a deeper examination of the phenomenon of polarization loss with the EUV intensity will be carried out. A simulation for the underlying cause of this phenomenon, based on the space charge effect, will also be presented.

1.4.1 FEL fluctuations

As it has already been described above, time fluctuations in FLASH (and, generally, in any FEL source) become critical for time-resolved experiments. The gross timing of FEL pulses derives from the arrival times of the electron bunches at the undulator. These might be due to several factors such as time jitter of the electron gun, amplitude and phase fluctuations during the

off-crest acceleration in the accelerator cavities or dispersive effects in the energy-dependent magnetic chicanes. These fluctuations can nonetheless be accurately measured and accordingly minimized through closed loop feedback systems. However, the SASE process undergone in the undulator that produces coherent EUV radiation is of statistical nature, i.e, started by random emission of photons. The spontaneous origin of this process is the reason why almost all parameters (timing, intensity, spectrum, lasing mode, etc.) in the resulting EUV pulses fluctuate in a random manner. Such fluctuations lie usually in the range of the cooperation time of the system, which is a few femtoseconds for soft x-rays and less than a femtosecond for hard x-rays [167].

From all varying parameters besides time, intensity is the most relevant to the spin-resolved measurements undertaken in this work. During beamtime operation, intensity changes of up to 100 % from pulse to pulse were not abnormal, this becoming a source for appreciable noise in the asymmetry signal. Intensity needed then proper tracking in a pulse-to-pulse basis in order to be conveniently sorted for processing. In the previous section, the GMD method for retrieving the intensity of the EUV beam has been outlined, however it doesn't account for the intensity of the beam at the end of the experimental beamline. This is by no means a minutia, since the PG2 experimental beamline (the one used in the actual measurements) incorporates a monochromator. This device consists of a plane diffraction grating, preceded by a collimating mirror, and auxiliary optics [171]. With an operating range of 25 eV to 90 eV and realistic resolving powers up to 6000 at 48 eV [272], it can achieve a highly monochromatized beam despite the undulator being able to produce EUV light with a fundamental photon energy bandwidth of already 0.5 %–1 %. The monochromator transfer function from the input EUV light is generally not known due precisely to the fluctuations in the spectrum of the FEL. Therefore, the energy of the pulses before and after the monochromator are not directly correlated and a secondary measurement for the relative pulse intensities has to be made close to the experiment. For this purpose, an MCP-based photon detector has been chosen that makes use of the tiny fraction of light scattered from a thin gold wire intersecting the EUV beam. This light is then collected by an MCP detector whose voltage response has been adequately calibrated and is related to the FEL intensity. Relative accuracies better than 5 % have been reported with this method [38].

Fluctuations in intensity can be capitalized on by performing intensity dependent measurements according to the fact that such fluctuations span a reasonably confined region during normal operation of the FEL. To extend the intensity range deliberate attenuation of the EUV pulses can be obtained either through the krypton gas attenuator mentioned in the previous section, by using the exit slit of the experimental beamline just after the monochro-

mator or through the metal filter foils, in this case aluminum, also indicated above. The krypton attenuator, at a pressure of 5×10^{-3} mbar, can reduce the intensity only by a factor of two, whereas the exit slit can diminish it by around 30 % within a width change of 10 µm to 100 µm. On the other hand the aluminum filters can produce more than two orders of magnitude decrease in the intensity.

1.4.2 Detection scheme

The PG2 beamline including the monochromator which has been used in the experiments is described in [171, 88]. As detailed in section 1.3.3, 30-pulse bursts are delivered from the FEL with a 10 Hz repetition rate and a separation of 10 µs between pulses. The pulse length of ca. 50 fs–100 fs FWHM was estimated from the EUV beam spectrum and the transmission function of the monochromator via simulation. Pump pulses were a bit longer, around 130 fs and with the same structure as the FEL. The switching magnetic field that magnetizes the sample between bursts consisted of 12 µs FWHM long pulses set off 300 µs before each FEL macro-bunch.

As depicted in fig. 1.18, both the FEL probe and the pump hit the sample at 45° to the surface normal. The photons from the EUV light have enough energy to trigger emission of photoelectrons, which are collected by the lens system through an accelerating electric field and channeled to the Mott detector. The absorption of photons from the EUV pulses in the iron film produces electronic excitations, mostly in the form of electron-hole pairs. The excited electrons with energies greater than the plasmon energy $\hbar\omega_p$ favor the creation of plasmons, which constitute the first stage of the cascade effect [191]. For energies lower than $\hbar\omega_p$ electron-electron collisions are the main source of relaxation, followed by electron-phonon interactions. At the same time, Auger processes fill the holes left by the excitations, adding up to the latter mechanisms. The cascade is mainly originated from electrons in the 4s-p and 3d orbitals of Fe, since they are the most weakly bound. They also form an energy band spanning around 10 eV below the Fermi energy, where they are subject to the cited intra-band collisions and electron-hole pair creation. The electrons from the cascade contain lower kinetic energies due precisely to these relaxation processes. Some of them can, indeed, leave the sample without undergoing any relaxation at all. And it would in fact be desirable to measure them instead, since their polarization wouldn't have been affected by spin-dependent collisions. However the electron yield retrieved from these rarities is too low for a significant signal, an issue for which the also low efficiency of the Mott detector is partly to blame.

In fig. 1.18 the binding energies of the Fe bands are sketched along with the intensity spectrum of the photoelectrons after leaving the sample. Here the energy axis should be read as $E_{kin}^{n'l'} = E_b^{nl} + E_\gamma - W$, that is, the kinetic

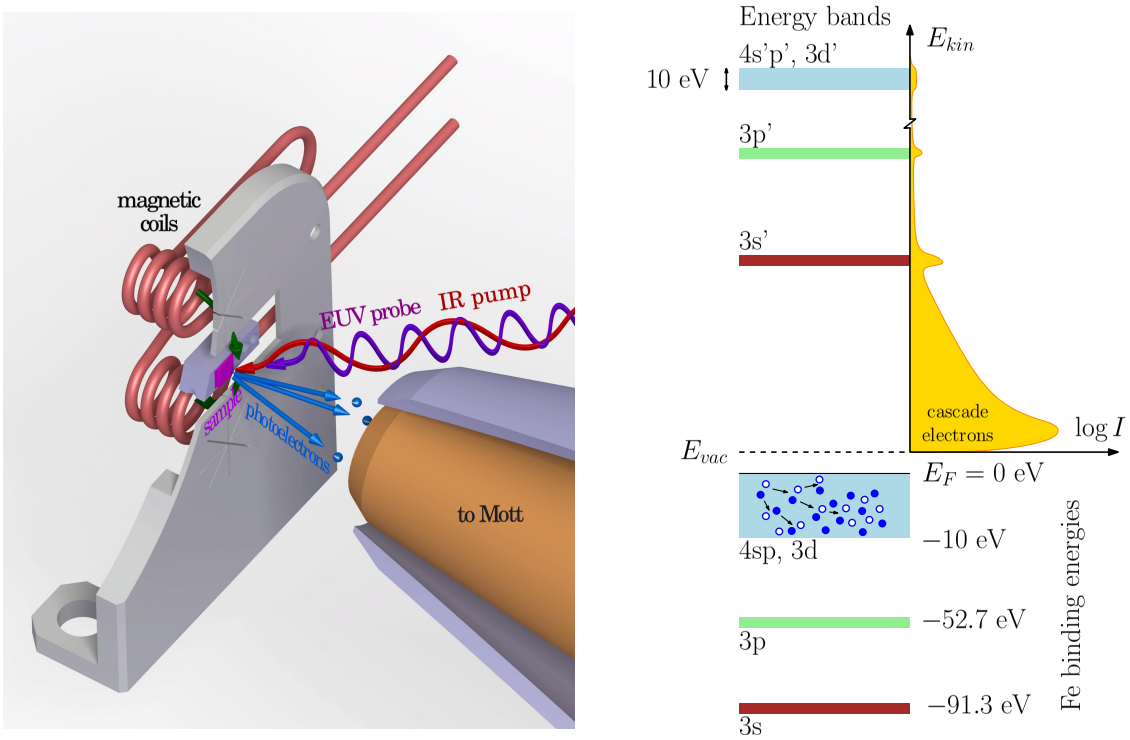

Figure 1.18: Detection scheme of the FEL experiments. Both pump and probe pulses impinge with 45° into the sample surface. Interaction of the iron with the probe releases photoelectrons that are collected by the electrostatic lens system and directed to the Mott device. An energy diagram shows the expected intensity of the photoemitted (and detected) electrons according to their origin within the energy band structure of bulk iron. Secondary electrons are basically generated in the outermost orbitals by internal collisions before leaving the sample. Such electrons have lost most of the initial kinetic energy transferred by the EUV photons and accumulate at the beginning of the intensity spectrum, which provides a strong signal from which asymmetry values can be determined.

energy of each band is equal to its binding energy plus the photon energy $E_\gamma = \hbar\omega_\gamma$ from the EUV pulse, not without offsetting the workfunction of iron $W = 5.1\,\text{eV}$ [97, p. 40]. Photoelectrons from one of these bands which have lost energy through relaxation appear below the respective energy level, as exhibited in the cascade. Most of the cascade photoelectrons have their origin in the 4s-p and 3d bands, which correspond to valence electrons in Fe. Since the magnetic moments of transition metals is mainly contained in these bands (effectively in the d electrons [250, p. 529]), the cascade must include an integrated value of the magnetic moment throughout the valence band.

1.4.3 Time-resolved measurements

In the following measurements at FLASH the energy analyzer in the setup of fig. 1.1 was used with a kinetic energy of 100 eV. The 15 ML thick Fe sample remained at ground potential while the collector of the lens system was set to 890 V to suck in the liberated photoelectrons. The signal collected from the Mott is thus blatantly dominated by the cascade, and since core electron shells show virtually no net magnetic moment, the measured polarization will come from the electrons in the valence band. The FEL photon energy was set to 40 eV due to a relatively higher photo-absorption cross section in the valence band at these energies [48]. Pulses were around 30 fs long with a maximum intensity of $0.5\,\text{mJ}\,\text{cm}^{-2}$. The excitation light coming from the pump had an energy of 1.55 eV and was conveniently focused to a greater region than the probe in order to avoid inhomogeneities, resulting in a pump intensity of nearly $12\,\text{mJ}\,\text{cm}^{-2}$, more than enough to trigger a quenching in the magnetic moment [42, 60].

Each measurement (event) undertaken at the end station is also associated with a large set of diagnostic data describing the state and parameters of the whole FLASH system, as evidenced in section 1.3.2 and 1.3.3. Before any data processing can be performed, the relevant information from this data pool needs to be retrieved. A sophisticated data acquisition system (DAQ) has been implemented in FLASH for this purpose. A central multi-processor computer collects data from around 1000 ADC channels and more than 30 cameras at a rate of up to $50\,\text{MB}\,\text{s}^{-1}$. Incidentally, 30 days of FLASH operation can provide up to 20 TB of stored data [6]. An API based on the ROOT file system developed at CERN is then used to extract the relevant data, conveniently averaged and compressed, to be loaded and further processed by analysis tools such as MATLAB. With this in hand, the spin polarization P of the photoelectrons for each pump-probe delay time is calculated using eq. 1.3 and 1.4 with jitter and time drift corrections from the corresponding BAM and streak camera measurements. Fig. 1.19 shows the time-resolved polarization signal for two different timescales. The longer time-span graph

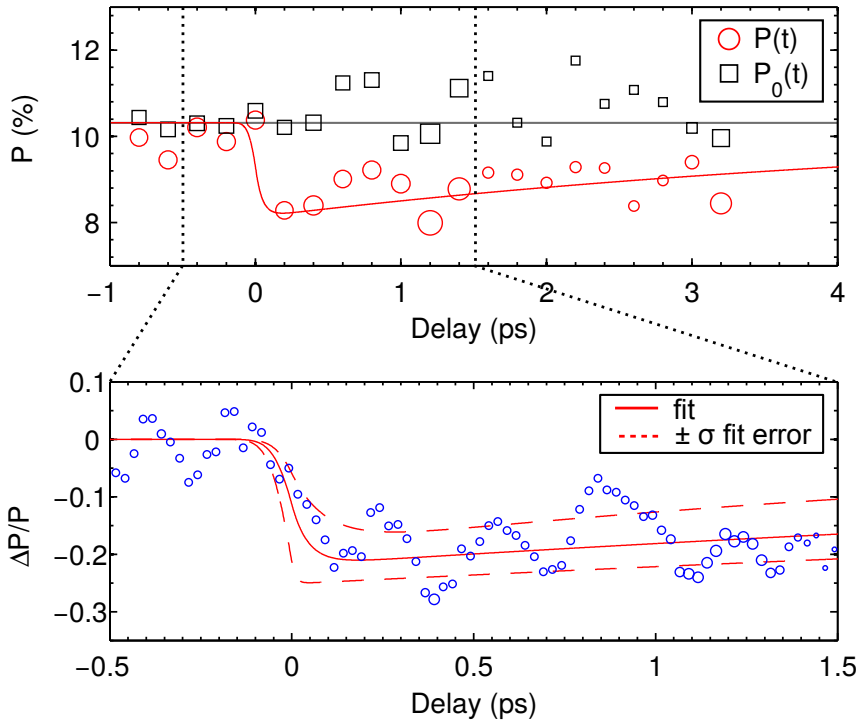

Figure 1.19: Quenching of the magnetization of a 8 ML iron film for two different timescales. In the picture above the polarization of both the pumped $P(t)$ and unpumped $P_0(t)$ signals is depicted. Data bins are 200 fs long. In the picture below the time span has been reduced to allow for a finer time resolution (bin size of 25 fs) and a smoothing filter for signal-to-noise improvement has been applied. The ultrafast magnetization decay on the order of 100 fs (see text description) is clearly visible. The diameter of each point is proportional to the amount of data for that bin. Adapted from [82].

plots data binned in 200 fs intervals. The diameter of the data circles is proportional to the amount of datapoints present in each bin. The P signal represents the polarization in the presence of the IR pump and clearly exhibits a sudden decay near the origin. P_0 is the reference signal, i.e. the polarization in the absence of the pump, which should remain constant throughout the measurements. A zoomed-in version of the demagnetization is depicted in the figure below. In this case the same data has been binned in 25 fs intervals and the considerable noise smoothed out with a Savitzky-Golay filter[11]. Such a filter substantially maintains the form of the signal while suppressing higher frequency components as opposed to a simple increase in the bin size, which inevitably harms the time resolution. Still, the filter introduces

[11] of degree 3 and window size 11

mid frequency oscillations after the magnetization drop as a consequence of a finite window size. However the artifact is not relevant for the extraction of the demagnetization parameters. Here the relative polarization change is computed as

$$\frac{\Delta P}{P_0} = \frac{P - P_0}{P_0} = \frac{P}{P_0} - 1 \tag{1.6}$$

where P_0 is the average polarization before the time origin. Fits to the demagnetization curves were performed by a double exponential function in convolution with a gaussian pulse shape simulating the laser finite excitation:

$$\frac{\Delta P}{P_0} = C\Theta(t)(1 - e^{-t/\tau})e^{-t/\rho} * G(t, \sigma) \tag{1.7}$$

In this equation C is a proportionality constant, $\Theta(t)$ is the Heaviside step function centered at time zero and τ and ρ are two characteristic times of the demagnetization curve. τ is related to the decay time and it is often used as a measure of the demagnetization time itself. ρ is identified with the recovery time and is usually referred to as the *relaxation* time. The gaussian pulse must have a broadening $\sigma = \mathrm{FWHM}/2\sqrt{2\ln 2}$, where $\mathrm{FWHM} = 0.6\,\mathrm{ps}$ is estimated from reflectivity measurements. Obtained fit parameters were $\tau = 45 \pm 50\mathrm{fs}$, $\tau = 5 \pm 3\mathrm{ps}$ and $C = -22 \pm 3\%$.

The above results clearly show that the magnetization of an iron thin film can be quenched in a timescale on the order of 100 fs. This is in accordance with previous experiments and simulations performed on transition metals [42, 52, 131, 243, 283]. Furthermore, since the magnetic moment of the cascade electron comprises an integrated value of the valence band, the conjecture that the spin angular momentum might be buried deeper in the band structure, therefore being inaccessible to other optical probing methods such as magneto-optical Kerr effect, can now almost certainly be ruled out. This issue, initially raised by authors like Oppeneer [189] or Koopmans [146], has been object of controversy in the literature for the past decade. The presented results are in line with, and add to, the addressment of the problem from other authors [29, 53].

A special remark must be made on the polarization measured by the cascade electrons. It is well known that the inelastic mean free path[12] (IMFP) of the electrons in ferromagnets is both spin- and energy dependent [89, 280]. This difference makes majority spins usually less prone to scattering, i.e. they exhibit longer lifetimes and hence have a higher probability to escape from the sample before scattering out. The polarization signal is thus enhanced by this *spin filter* effect, which is shown to be up to a few times stronger at lower energies, where the presence of empty d states dominates over the

[12]The average distance itinerant electrons can travel inside a material before they undergo any scattering events.

relatively small number of free *s-p* electrons that can serve as scattering targets [195]. Spin filtering for a fixed energy range therefore introduces a systematic net majority polarization due to the difference in IMFP, which results in an improved polarization signal from the cascade. In this context, the relative change in magnetization should remain unaffected unless the IR pump was incidentally impairing this effect. This is very unlikely to happen, since the energies at which the spin polarization is highest comprise the first 10 eV of the electron cascade. These electrons have already overcome the material workfunction of ca. 5.1 eV and should hence have started with kinetic energies in the range 5 eV–15 eV, which appears substantially higher than the 1.55 eV photon energy of the pump.

1.4.4 Polarization vs pulse energy

Although time-resolved experiments throw results consistent with the literature, the legit question remains on whether the FEL pulse intensity may be affecting the extracted polarization in some way. At first sight this shouldn't be the case; pulse intensities achieved during the working beamtime were barely higher than a few hundreds of $\mu J\,cm^{-2}$, and studies on Co/Pt samples have determined that permanent changes in the magnetization are not seen below FEL fluences of a few $mJ\,cm^{-2}$ [99, 269]. We are about to see, however, that the FEL intensity indeed affects the measured polarization, although for a different reason.

In the next set of measurements at FLASH a simple 20° deflector arm was used in substitution of the energy analyzer of fig. 1.1. The deflector was employed in order to avoid scattered light coming from the pump reflection onto the sample, which could otherwise reach Mott detector. Thus, the signal collected from the Mott consisted this time in photoelectrons from all the energies depicted in fig. 1.18, the upper limit being at 100 eV, which is the energy acceptance of this detector. The FEL photon energy was set to 182 eV and the laser timing pattern was that of fig.1.14. In this way, the collected signal in the Mott detector was much higher and allowed for a reliable polarization measurement for a wide range of FEL intensities. As mentioned in section 1.4.1 the intensities of the FEL were modified through the gas attenuator, the exit slit and to a greater extent by the aluminum absorbers, which were used to cross to the low intensity regime below $5\,\mu J\,cm^{-2}$. Pump intensity was virtually the same as in the time-resolved experiments of the previous section. The sample used this time was grown to 15 iron ML.

Fig. 1.20 (a) displays the relative polarization against the intensity of the FEL pulses. Its value remains fairly constant until around $10\,\mu J\,cm^{-2}$, where a reduction of up to a 40 % from the initial value can be appreciated at $300\,\mu J\,cm^{-2}$. Since the used intensities are not susceptible of altering the magnetization state of the sample, one could be tempted to look for an

explanation in an interaction-based spin loss during the photoelectron flight to the detector. This attempt must be undoubtedly discarded under the implacable rule of the angular momentum conservation. Electrons traveling in vacuum should maintain their overall spin momentum, plus certainly Møller scattering is spin-independent at non-relativistic speeds; hence no spin momentum loss can be expected thereof. The next natural attempt is to attribute the change of polarization to a *space charge effect*, i.e. the repelling Coulomb interaction that selectively screens highly polarized electrons at higher intensities. A detailed description of this effect will be presented in the next section but the results of its simulation are already superimposed in fig. 1.20 (a) for comparison. Fig. 1.20 (b) shows the intensity-normalized electron yield calculated as

$$\bar{Y} = \frac{Y(I_{FEL})}{I_{FEL}} \tag{1.8}$$

with $Y(I_{FEL}) = \sum_{i=1}^{4}(D_i^{\uparrow} + D_i^{\downarrow})$, that is, the sum of the Mott signals D for all four detectors and both magnetization directions. It is long known that photoemission yields show a positive, highly linear dependency with laser intensity for low-to-high intensities and a non-linear one for very high intensities [78, 27]. Clearly, then, the measurements are subject to a loss of electron yield by another mechanism. The space charge effect could account for this trend by screening out electrons during the emission process or by expelling them far enough to put them out of the detector entrance aperture (simulation line in fig. 1.20 (b)). The evaluation of this hypothesis is described in the following sections.

1.4.5 The space charge effect

When charged particles are emitted from any part of a solid in sufficient quantities, they can form a charge *cloud*, that is, a region in space that can be physically treated as a continuum charge distribution. This concept is commonly referred to as *space charge*. It generally only occurs in dielectric media or in vacuum, since conductive materials tend to rapidly diffuse and neutralize charge accumulations. One of the earliest examples was Thomas Edison findings in 1880 that incandescent filaments inside vacuum bulbs created a temperature dependent current when a negatively biased electrode was placed nearby. This effect, initially baptized as the Edison effect [34], would be termed *thermionic emission* by Owen Richardson after the discovery of the electron in 1897 [216]. During the same period the studies of Heinrich Herz, Aleksandr Stoletow and Philipp Lenard among others showed the emission of electrons from metal surfaces lit by UV lamps [108, 159, 251], establishing the well-known *photoelectric effect* later described by Albert Einstein.

The accumulation of charge near its emitting medium can be a side effect and sometimes the cause of disturbances in experiments on a variety of

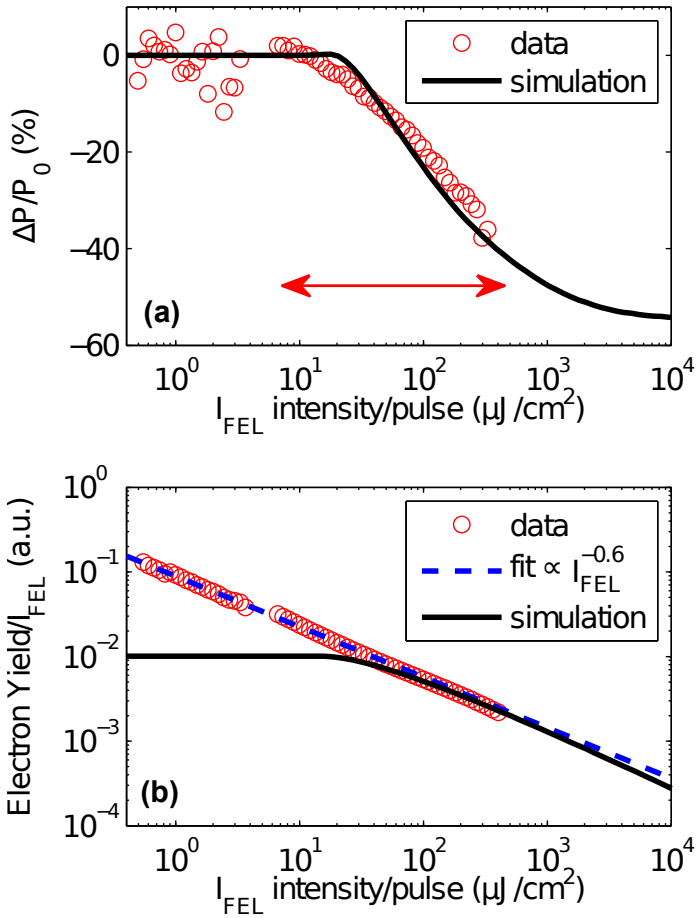

Figure 1.20: Polarization change (a) and intensity-normalized photoemission yield (b) as a function of FEL pulse fluence. The loss of both polarization and yield at higher intensities, as well as the power law fit, suggest space charge effects acting on the photo-emitted electron bunches backed up by simulation. In (b) the simulation data has been purposely rescaled to show the asymptotic behavior as the unknown transmission function of the lens system through which electrons travel cannot be taken care of in the simulations. Adapted from [82].

fields, ranging from plasma physics to semiconductor technologies or vacuum electronics. In RF injector guns such as the one used in FLASH, for instance, space charge effects emerging from high intensity driving lasers strongly degrade electron bunches through Coulomb repulsion if they are not properly accelerated to relativistic speeds immediately after emission [138]. Even so, effects from space charge still need to be taken care of in several stages of the FELs such as the RF cavities, the compressor chicanes and specially in the coupling of electron beams to the FEL undulators, in order to minimize collective instabilities [186]. On the other hand, the quick-witted group of Schneidmiller and coworkers has recently suggested taking advantage of space charge instabilities to generate EUV and x-ray radiation [234].

In the field of photoemission spectroscopy (PES) space charge effects are nothing new. Energy redistribution of photo-emitted electrons due to the Coulomb interaction between themselves and their mirror charges give rise to an energy shift and a peak broadening of the resulting photoelectron distribution [289]. When examining core-level states of solids and molecules, for instance, determination of spectral shapes and peak positions with high accuracy, a critical part of many PES techniques, can be affected by such interactions [199]. In other experiments the appearance of *ghost* peaks or unexpectedly high energy electrons in the spectrum has been reported [90, 91]. In femtosecond, high-intensity laser-driven PES studies space charge is also a not inconsiderable factor [66, 193].

When examining ultrafast demagnetization, Teichmann and coworkers were cautious in stretching their driving IR pulses to avoid disturbances from space charge [254]. Other authors in this field have reported peak shifts in their pump-probe experiments from synchrotron or FEL sources [25, 106, 107]. In these cases, however, space charge is assumed to be pump-induced. For instance, Hellmann *et. al.* demonstrate peak energy shifts depending on the pump-probe delay [107]. Notwithstanding, it was shown in section 1.3.2 that FEL sources have incomparably higher brilliances, and their notably large photon densities alone are likely to engender space charge in metal surfaces. Also their photon energies ranging from EUV to hard x-ray allow for efficient photoemission since no multi-photon emission is required. Not surprisingly, some authors have also reported peak energy shifts due to FEL only pulses in their hard x-ray PES (HAXPES) studies [188, 190]. Besides, most of the PES experiments focus on perturbations of the electron spectral distribution, but no effect of the space charge on their resulting polarization is analyzed. For instance, the FEL fluences considered in the work of Oura and coworkers ($10^4\,\mu J\,cm^{-2}$–$10^5\,\mu J\,cm^{-2}$) are certainly at least one to two orders of magnitude larger than the ones taken for the present study (see fig. 1.20), but it will be shown that the polarization values are still severely influenced by a comparably smaller space charge production.

1.5 Simulations for the space charge

In this section details of the space charge simulation will be provided. Briefly, the accumulation of charge in the vicinities of the metal surface acts both as a charge screener and an energy redistributor. Electrons with lower energies adding to the charge cloud may be slowed down or even bounced back to the sample, whereas Coulomb repulsion might increase transverse divergence of the bunch to the point where some photoelectrons fall out of the collector entrance range. Since low energy electrons from the cascade carry most of the polarization, this effect distorts the resulting measured value in a predictable way.

1.5.1 Problem definition and parameters

The presented simulation was undertaken with the help of the program package ASTRA (A Space charge TRacking Algorithm) developed in the DESY facilities in Hamburg. This algorithm, written in Fortran 90, is freely available for non-commercial use with executables in several platforms (Windows, LINUX, Solaris or Mac X)[13] and its parallelized version is maintained to date. It has been extensively applied in the field of photoinjector design with reported success [79, 110, 288], as well as for the benchmarking of experimental data in FLASH [200, 116, 288]. The ASTRA *suite* contains the particle tracking code, an input distribution generator and two post-processors running a graphical user interface based on the PGPLOT[14] library. The program has yet some limitations. Only one input distribution can be entered at a time, the post-processor routines are barely tunable and the output data is spread over different files that need to be brought together for cross-referenced data analysis. Therefore, a python routine has been implemented that handles input parameters and output data processing while leaving the hardcore tracking computations to the main ASTRA program.

The ASTRA algorithm tracks point-like charge carriers such as electrons, positrons, protons or hydrogen ions under the influence of an (optional) input external field. The fields have to be rotationally symmetric, usually generated from standing wave cavities, travelling wave structures or electrostatic sources. The program then computes the trajectories of the particles taking into account the space charge field internally generated in the cloud. The computation method is based on Runge-Kutta integrations of fourth order and fixed time step. Beam line elements such as cavities, solenoids, dipoles and quadrupoles, cathodes or apertures are to be placed with respect to a global Cartesian coordinate system whose longitudinal axis (and

[13] http://tesla.desy.de/ meykopff/

[14] Freely available at http://astra.caltech.edu/ tjp/pgplot

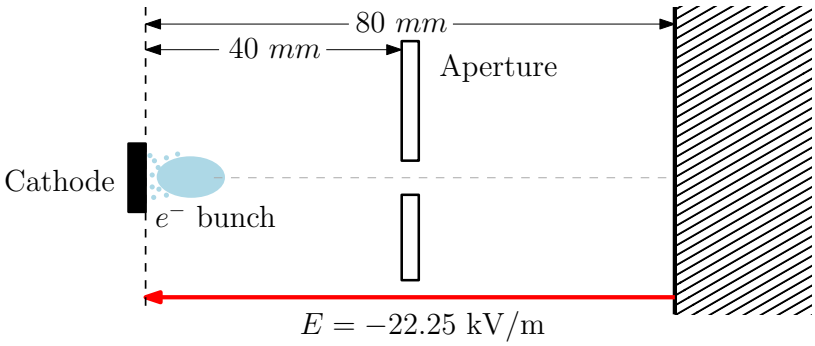

(a)

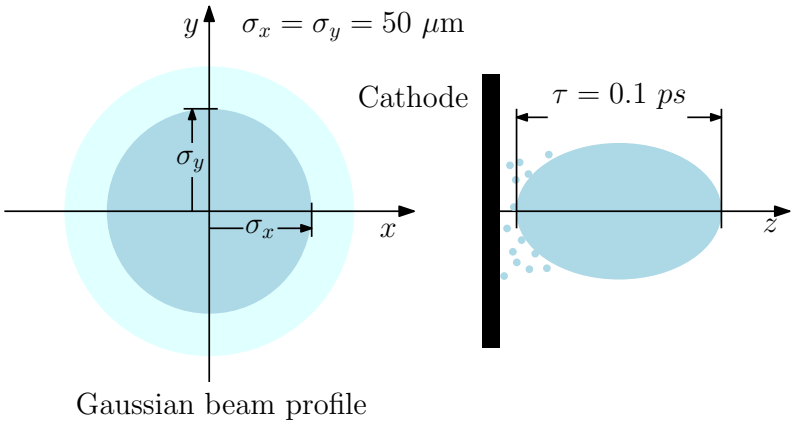

(b)

Figure 1.21: (a) Geometry of the simulation. Electrons emitted from a photo cathode are accelerated by a static electric field $\vec{E}$ towards an aperture reproducing the collector entrance to the lens system 40 mm apart. The simulation ends after the remaining electrons have been tracked up to 80 mm away from the cathode. (b) Detail of the electron bunch spatial geometry. Photoelectrons are released from the cathode in a semi-random manner within a time constant on the order of the FEL pulse length. The initial energy and momentum distribution is taken from experimental measurements.

preferred direction of motion) is defined as the z-axis, with the x- and y-axes defining the horizontal and vertical directions of the transverse plane.

To simulate the space charge effect in the photoemission experiments in this work the geometry of fig. 1.21 (a) has been introduced. An emitting cathode representing the FEL-driven photoemission from the sample engenders an electron bunch that is accelerated by a homogeneous electrostatic field $E = 22.25\,\mathrm{kV\,m^{-1}}$. The field is generated in the experiment by the potential difference between the sample and the entrance of the lens system,

$\Delta V = 890\,\mathrm{V}$. However in the simulation it is introduced by hand without the need of potentials. The entrance of the collector is modeled as an aperture placed at a distance of 40 mm from the cathode. The diameter of the real collector aperture is 10 mm, but since the transmission function of the lens system into the Mott detector is unknown, it could be argued that some additional electrons would be lost inside the lens system, altering the agreement with the simulated results. For this reason other values of the aperture have been tested for comparison. The ASTRA routine keeps tracking the particles beyond the aperture until they have traveled double the distance to the aperture, i.e. at $z = 80\,\mathrm{mm}$. This is a rather arbitrary value, however some additional tracking distance is convenient to better observe the effects of transverse momentum spread and the overall bunch deformation.

In fig.1.21 (b) the geometry of the electron bunch is shown. Following the Gaussian profile of the FEL pulses the photo-emitted electrons are assumed to adopt the same spatial distribution. For simplicity a symmetric profile on both the x- and the y-axis has been chosen, thus neglecting actual beam deformation from leading optics, with a standard deviation $\sigma_x = \sigma_y = 50\,\mu\mathrm{m}$. This choice shouldn't sabotage the simulation main results, since the size of the bunch is three orders of magnitude smaller than the aperture and the momentum part of the phase space distribution is by far the most relevant factor. Although it is possible to start with an initial electron phase space distribution, the emission from a cathode allows for the inclusion of a time constant that mimics the ultra-fast but time-constrained generation of photoelectrons upon excitation of the FEL. This time constant, defined as the rms emission time, has been set to $\tau = 100\,\mathrm{fs}$ to reflect the EUV pulse length ($\approx 50\,\mathrm{fs}$) and determines the bunch length. The use of a time-dependent emission is of considerable importance when dealing with space charge effects, since it is during the emission process that the screening mechanism takes place.

For optimal simulation efficiency the cylindrical symmetric gridding scheme was preferred over the full 3D FFT algorithm. In the former system a cylindrical grid, with coordinates (r, φ, z), comprising radially concentric rings with longitudinal slices is created around the space of the particle bunch. The grid is dynamically scaled at each iteration to match the actual dimensions of the bunch. It is then Lorentz transformed to the average rest frame of the bunch to sidestep relativistic effects. In this frame the charge density can be assumed constant in each ring so that the static space charge field therein can be computed by simple numeric integration over the rings. The field at points other than the grid center points is retrieved from a cubic spline interpolation, which ensures both the field and the first spatial derivatives to be continuous functions. After integration, the field is transformed back to the laboratory system. Outside of the grid a $1/r$ decaying field is applied as an extrapolation to maintain definition over the whole space.

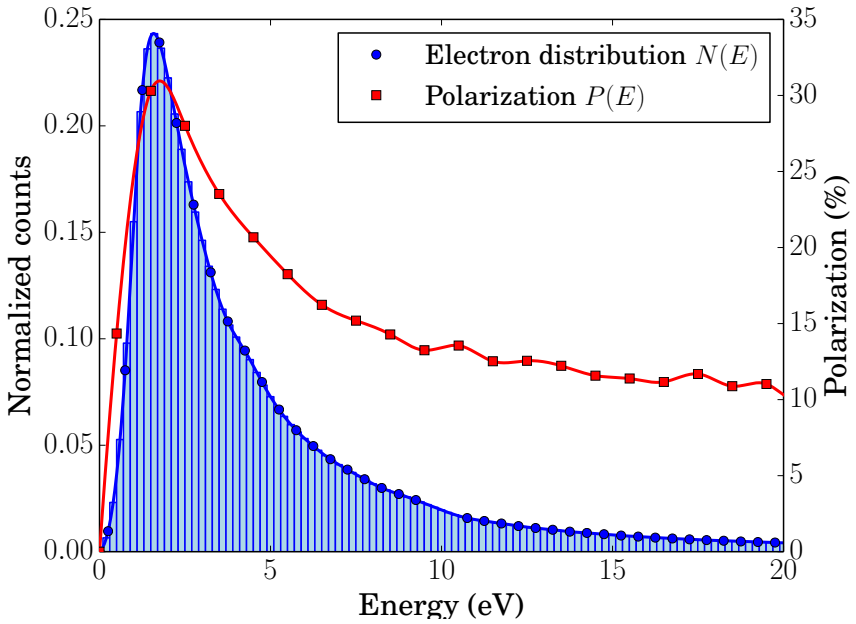

Figure 1.22: Measurements for the electron distribution (blue squares) and polarization (red squares) used to generate the input electron distribution for the simulation (histogram). Blue and red lines are a cubic spline interpolation of the data.

The initial momentum distribution of the particle bunch is a key point of the simulation. For this reason a custom distribution profile was taken from experimental measurements using an electron gun at 4 keV to excite a 15 ML iron film on W(110) within the setup devised in section 1.2. Fig. 1.22 exhibits the electron spectrum (blue squares) resulting from these measurements and conveniently interpolated (blue line) to provide a smooth function $n(E)$ from which an input distribution can be generated. It is important to point out here that the number of particles as a parameter in the simulation has been held to a fixed value of $N_0 = 10^5$. Although different FEL intensities would provide different number of photons per pulse, thereby modifying the number of photo-emitted electrons, it is the total charge Q that has been set as the independent variable, and therewith the charge per particle. Hence for the initial distribution, the same number of particles have been randomly assigned an energy (momentum) value according to the experimental probability distribution. A histogram of the generated distribution is overlaid under the experimental plot for comparison.

Clearly, the spectrum depicted in fig. 1.22 shows the conspicuous peak from the secondary electron cascade [63], yet the question might arise on whether

the excitation mechanism, i.e EUV pulsed radiation or a continuous electron beam, has an influence on the form of this cascade. As it is well established, the nature of the irradiating carriers is irrelevant for the cascade formation [276]. The cascade itself is a complex phenomenon involving several relaxation channels. For most metals at room temperature these are mainly electronic, being dominated by electron-plasmon relaxation rapidly followed by electron-electron interactions, as extensively modeled by Ovchinnikov and Kresin [191]. These mechanisms have characteristic times from a few tenths to a few fs [5], which is substantially faster than the FEL pulse length. To this regard, it is expected for the EUV pulses to be seen as a continuous excitation by the electron sea, an argument that justifies the use of the electron gun generated input distribution.

Fig.1.22 also depicts the polarization (red squares) of the electrons from the same experiment with its corresponding interpolation (red line) to obtain the function $P_0(E)$. The characteristic peak-and-tail shape observed has been extensively documented and is attributed to the spin filter effect described in section 1.4.3 [195, 196].

1.5.2 Results and discussion

Space charge tracking is a computationally demanding task. Daylong runs were required to perform one set of calculations with 100 different charge values and $N_0 = 10^5$ particles, the latter parameter severely affecting the computation time. For each total charge value Q the particles reaching the end position at $z = 80\,\text{mm}$ were energy-binned and a new distribution yield $Y(Q, E) = N(Q, E)/N_0$ was obtained. Fig. 1.23 shows such distributions for some selected charge values. For the lowest charge, $Q = 10^{-5}\,\text{nC}$, the resulting distribution is virtually identical to the input distribution in fig. 1.22. For low charge values the space charge effect is negligible and basically all particles reach the collector entrance. As the charge is increased, lower energy electrons are ejected by the electron bunch and lost in the tracking process. This effect is stronger at higher charge values, where only higher energy electrons survive, as the tail overlap among all distributions exhibits. Most of these electrons are backscattered to the sample during their emission. Some others, though, can be expelled along the transverse direction during acceleration and will eventually be blocked by the aperture. This is reflected in fig. 1.24 (a) where the total electron yield $Y(Q) = N(Q)/N_0$ as a function of the total charge value is depicted for different apertures. When no aperture is included in the simulation, the decrease in the total yield can only be explained by the back-scattered electrons. For finite apertures, however, such a decrease is amplified on account of the beam divergence dependence on the total charge. Smaller apertures block electrons with higher transverse momenta at lower charge values than wider apertures. Recall that a diame-

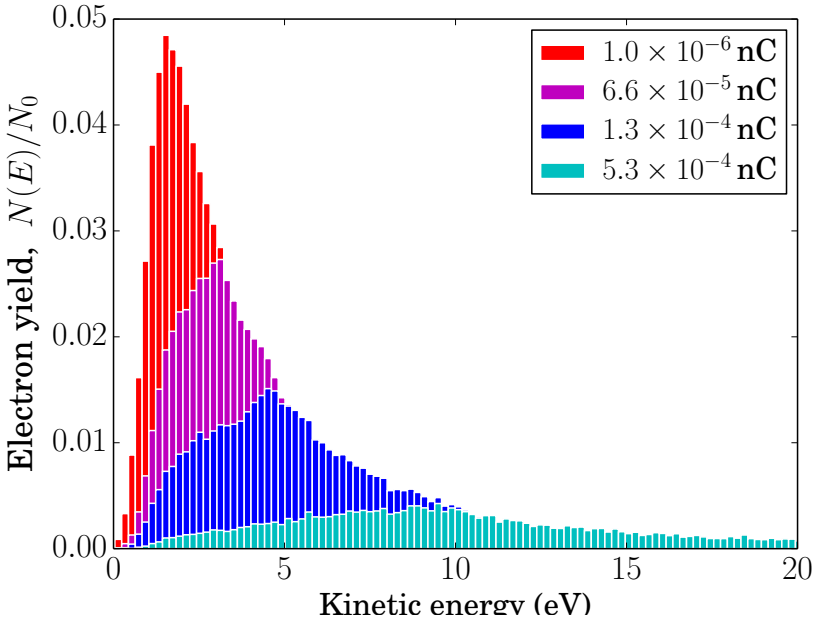

Figure 1.23: Electron yield distributions after simulation for different total charge values. The space charge effect selects out lower energy electrons by screening. This implies a modification of the integrated polarization as charge varies.

ter of 10 mm has been used for the simulations when not stated otherwise.

The effect of this inhomogeneous loss of electrons into the end polarization value is obtained by weighting the initial polarization distribution with the resulting yield distributions from fig. 1.23 for each total charge, that is,

$$P(Q) = \frac{\int_0^{E_{max}} P_0(E) Y(Q,E) dE}{\int_0^{E_{max}} Y(Q,E) dE} \tag{1.9}$$

where $E_{max} = 30$ eV is the integration limit given by the measurements. Plots of $P(Q)$ for the same apertures as in fig. 1.24 (a) can be seen in fig. 1.24 (b) for comparison. The shape of this plots can be qualitatively understood by comparing fig. 1.22 with fig. 1.23. For low charges, the resulting distribution remains unaffected, thereby leaving the integrated polarization value constant. At some threshold charge value, space charge effects start to play out by suppressing lower energy electrons while leaving higher energy ones intact. Since the former are more highly polarized, the end result is a decrease in the value of P from eq. 1.9. The decrease continues until only electrons far from the cascade peak remain. The polarization of these higher

energy electrons is fairly constant according to fig. 1.22, which justifies the value of P stabilizing at higher charge values. The effect of the aperture size is not so straightforward. The aperture does, indeed, block electrons whose transverse momentum is high enough to move out of its entrance range during acceleration. These are still higher energy electrons until the aperture is not small enough to interfere with those of the cascade peak, whose polarization is more relevant for the calculation of P. Therefore, changes in the shape of the polarization curve are not visible for too big apertures. This is a noteworthy result, since it implies that space charge mainly affects polarization values through screening near the emission point.

The tiny hump observable at $Q \approx 3 \times 10^{-5}$ nC in the beginning of the polarization downfall is due to the inaccuracy of the input distribution measurements. Since the polarization data points are limited in the beginning of the peak of fig. 1.22, the interpolation function assumes a high initial slope that precedes the electron distribution. When the first few electrons at the lowest energies with low polarization are screened out by the space charge, there is a sudden albeit slight increase in the integrated polarization value.

Variation of the bunch dimensions has also been tested to verify its qualitative impact in the polarization. Not surprisingly, fig. 1.25 (a) demonstrates that an increase (decrease) of the bunch size shifts the electron yield curve to the right (left), indicating that the space charge screening starts at a higher (lower) bunch charge values. The polarization is therefore shifted accordingly, as fig. 1.25 (b) evidences. Note howbeit that the shape of the curves are not affected in any case. In general, for reasonably symmetric bunch geometries, space charge does not affect the polarization behavior with the FEL intensity but, as expected, sets the fluence limit at which its effects start to take place.

It should not be disregarded that, on attempting the space charge simulations, the assumption has been taken that the intensity of the FEL pulses is proportional to the photo-emitted charge, i.e. $I_{FEL} \propto Q$. This assumption is generally accepted in photoemission studies of thin films and has been extensively studied in the field of photoinjectors, with the linearity holding even for high laser powers on some cases [51, 57, 209, 262]. The proportionality constant is the parameter that has been adjusted to fit the simulation with the polarization data in fig. 1.20. An important factor not considered in the simulation is the transmission function of the lens system after the photoelectrons enter the collector. At this point additional electrons might be lost or their energy and momenta re-distributed, modifying the final yield most likely in a decreasing manner and thus accounting for the discrepancy in fig. 1.20 (b). Deformations of the FEL beam spot size such as that resulting from a 45° incidence or deviations from an ideal gaussian profile could contribute to the aforementioned discrepancy. All in all, space charge effects

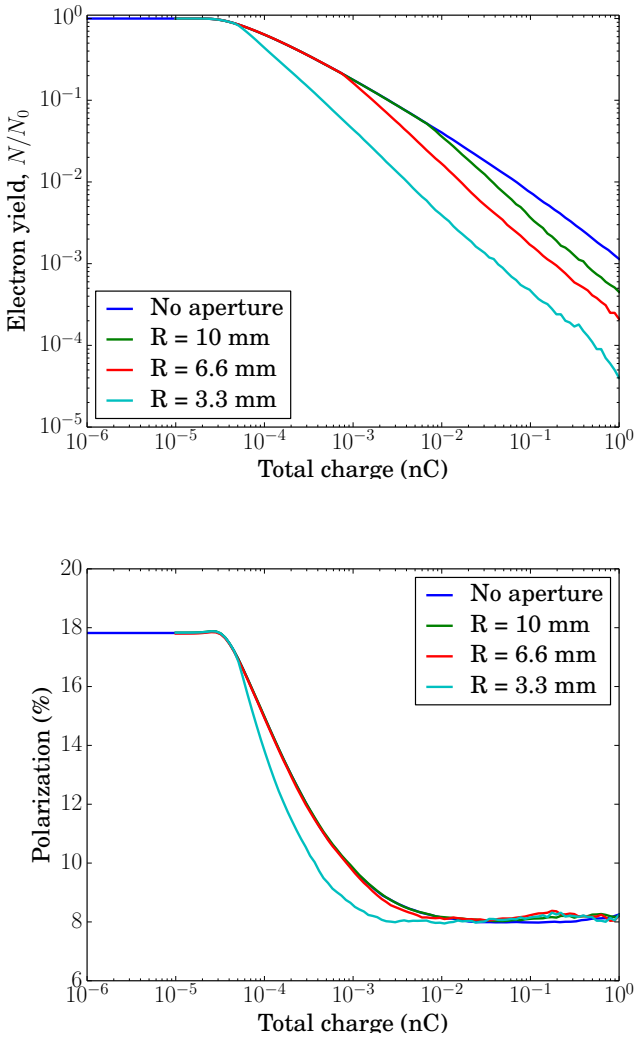

Figure 1.24: (a) Total electron yield as a function of the total charge in the simulation, computed as $Y(Q) = \int_0^{E_{max}} Y(Q,E)dE$, for different aperture sizes as well as for no aperture as a reference. (b) Polarization value as computed by eq. 1.9 for the same apertures.

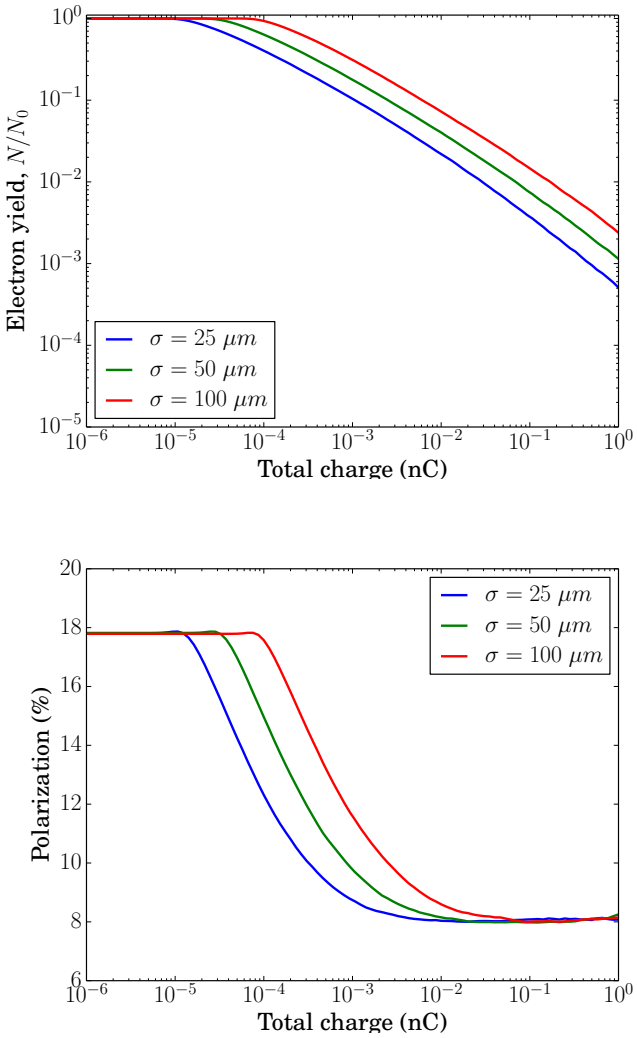

Figure 1.25: (a) Total electron yield as a function of the total charge in the simulation, computed as $Y(Q) = \int_0^{E_{max}} Y(Q, E)dE$, for different bunch sizes. Here $\sigma = \sigma_x = \sigma_y$ refers to the standard deviation of a gaussian-shaped pulse. (b) Polarization value as computed by eq. 1.9 for the same bunch sizes.

can, at least qualitatively, explain the loss of polarization in the intensity resolved measurements, rather than an FEL-induced demagnetization.

1.6 Summary and conclusions

In this chapter a time- and spin-resolved photoemission experiment on iron thin films with a pump-probe setup has been described. A FEL source has been used as the probing mechanism given the proven advantages of its properties, a combination of high brilliance, short pulse lengths and high photon energies albeit with limited (yet sufficient) repetition rates. With the EUV photon energies used (40 eV for the time-resolved measurements and 180 eV for the intensity-resolved measurements), electrons can be excited from anywhere withing the whole valence band, which spans over 10 eV under the Fermi level. Therefore, magnetization values can be obtained which constitute an average value over the valence band. Such values are retrieved from measurements of the polarization of the electron cascade formed during a photoemission process. In the time domain it has been shown that the magnetization of a magnetically saturated iron film can be quenched in a timescale smaller than 100 fs, which is in accordance with previous observations using alternative methods such as the magneto-optical Kerr effect [42, 52, 131, 243, 283]. This result adds new evidence that, during an ultrafast demagnetization, the angular momentum reduction probed by more indirect techniques reflects the angular momentum within the whole valence band, that is, there is no additional angular momentum buried deep in the band.

Due to the inherent fluctuations in the SASE process of an FEL source, plus the experimental ones that synchronization of the time-dependent driving mechanism (RF signals in cavities and compressors) introduces, the EUV pulse energy experiences a high level of fluctuations during beamtime. This has effects in the polarization of the photoelectrons, with its value being reduced when the pulse intensity increases. It has been demonstrated that this phenomenon can be explained by the influence of the space charge produced during the photoemission process. The corresponding simulations show that above a certain FEL intensity threshold the photo-generated electron bunch acts as a Coulomb barrier that rejects low energy electrons mostly through backscattering. Low energy electrons are primarily engendered in the cascade process that takes place in the valence band during photoexcitation, and hence carry most of the polarization. The net result is a non-linear loss of the total measured polarization with increasing FEL pulse intensity. This findings render valuable information to design novel spin-resolved experiments in the future. Further research is encouraged to make use of detection setups with improved FoM as well as simultaneous time, energy and spin resolution (e.g. SPLEED detectors [155]) in order to gain better

access to directly photoionized electrons from selected energy bands, which would provide a more precise understanding of the role and the dynamics of the band configuration in the demagnetization processes.

Chapter 2

Magneto-optical Kerr effect

In the last chapter time- and spin-resolved photoemission experiments with a FEL source have added evidence to an ultrafast demagnetization process in iron within a sub-picosecond timescale. Furthermore, it has been shown that the magnetization measurement comes from an integrated value over the whole valence band, a possibility not available in other measurement techniques such as the magneto-optical Kerr effect (MOKE), that indirectly probes the uppermost layers of the band structure. The results are consistent with extensive studies on both iron and other transition metals such as nickel, cobalt or gadolinium, using different experimental methods. With this in mind, the present chapter attempts to bring further insight on the mechanisms involving the ultrafast demagnetization by presenting experiments in the MOKE domain.

2.1 Overview on the Kerr effect

It is well known that the complex index of refraction of a material can be modified by the application of electric and magnetic fields. Several of these effects are possible depending on the type of field and the geometry of the experiment. The first of them was discovered by Michael Faraday in 1845 [62, p. 123], when he observed the rotation of a linearly polarized ray of light after passing through a silicon borate glass. Thirty years later, in 1875, John Kerr made a series of publications [133, 160] explaining his experiments with linearly polarized light, first on glasses and liquids under a strong electric field and later on magnetized ferromagnetic cores. In the first case he found changes in the refractive index of the material that were proportional to the square of the electric field. This would be coined the *electro-optical Kerr effect*. In the second case he found a change in the polarization (rotation and ellipticity) of light reflected from the ferromagnet which depended on the magnetization direction. This would become the *magneto-optical Kerr effect*.

Later studies by Hall, Kundt, Du Bois, Sissingh and Zeeman showed that the Kerr effect could be further grouped in three categories: the *polar* Kerr effect, when the the magnetization was normal to the surface, the *longitudinal* Kerr effect, when the magnetization was parallel to the plane of incidence of the light ray, and the *transverse* Kerr effect, when the magnetization was perpendicular to that plane. Both the Faraday and magneto-optic Kerr effects are linear phenomena, whereas the electro-optic Kerr effect is a quadratic process. Interestingly, all of them were discovered before the linear electro-optic counterpart, the Pockels effect, described in 1906 by Friedrich Pockels [203].

Since the 19th century MOKE has become a standard technique in the study of surface magnetism as well as a relevant tool for the development of commercial technologies such as magneto-optical storage [124]. In the research arena, the field of ultrafast magnetism has largely benefited from time- and spin- resolved MOKE techniques to study the magnetization dynamics on the femtosecond timescale [144, 139].

During this endeavor the question was raised on whether the Kerr effect properly measures the magnetization during the first picosecond after a laser excitation. Koopmans *et. al.* [146] challenged this statement in 2000 arguing that certain optical transitions were blocked in a strong out-of-equilibrium state. They found a discrepancy between the change in rotation and ellipticity of the pump-induced MOKE signal. This claim was backed by calculations from Oppeneer and Liebsch [189], but similar experiments were already in contradiction with this thesis [31, 53, 98]. Comin and co-workers clarified that, when taking the difference for opposite magnetization directions of the rotation or ellipticity, the artifacts described Koopmans disappeared. The groups of Zhang [286] and Bigot [30] further demonstrated that the magneto-optical signal follows the magnetization in a reliable way even in a sub-100 fs timescale. Moreover, the photoemission experiments presented in the previous chapter, as well as others [52, 243], are in agreement with the MOKE results. It is concluded, thus, that the MOKE method is adequate to inspect the magnetization dynamics on a sub-picosecond timescale.

In the next section, the different hypotheses around the mechanisms that drive the ultrafast demagnetization in metals are discussed.

2.2 Hypotheses on ultrafast demagnetization mechanisms

In their pioneering research in 1996, Beaurepaire *et. al.* determined a "decrease [of the magnetization] which occurs within 2 ps" in nickel thin films [26]. So far, electron dynamics from short laser excitations had been explained by the two-temperature model (2TM) describing the relaxation process between an out-of-equilibrium gas of electrons and the lattice bath. In

this thermodynamic model, the assumption is made that the internal interactions in each reservoir are much faster than the electron-phonon processes that affect the relaxation, that is, an equilibrium temperature T_e for the electron gas and T_p for the phonon gas can be defined wherefrom a standard Fermi-Dirac or Bose-Einstein distribution, respectively for each bath, follows. The interaction is then simulated as a set of coupled differential equations for the temperature of each reservoir where the coupling constant is the relevant parameter [242]. Beaurepaire extended this model, renamed as the three temperature model (3TM), by adding an independent spin temperature T_s interacting with the other two, thereby adding two more coupling parameters to the equation set. The results are in line with the experimental observations for the resolved timescales. However, some questions have araised ever since.

On the thermalization assumption

In the first place the thermalized reservoir assumption has been questioned by some authors. It had been long understood that dynamics of photoexcited electrons in metals are governed by non-thermal carrier distributions, when measured either by optical methods [96, 112, 253] or by direct time-resolved PES [39, 77, 176, 180]. Lisowski and coworkers, for instance, pointed this out while showing nonlinearities in the Fermi distribution of ruthenium samples that increased with laser fluence [162]. Pietanza *et. al.* call attention to the inaccuracies of the 2TM in their semi-empirical model for silver films based on the Boltzmann kinetic equations [198]. Nonetheless, most of these claims relied on investigations for noble metals (mainly Au, Ag and Cu), partly because their full d-bands are less prone to interacting with the sp electrons, thus approaching them to an ideal Fermi liquid model. The Fermi liquid theory (FLT), built upon the self-energy operator of the many-body solid-state theory, is the most widely used first-principles model so far [24, 187]. Even for noble metals, though, the agreement with the experiments is far from absolute, particularly at electron excitation energies close to the Fermi energy. Subsequent refinements making use of more realistic band structures from electron-density functional theory and considering higher order perturbations did improve the agreement to a great extent, yet for low energies the behavior is still not fully reproducible [290].

Theoretical understanding of these dynamics is important because the lifetime of non-equilibrium distributions might have a direct implication in the ultrafast transfer of the total angular momentum during the demagnetization process. For instance, calculations from the Fermi liquid approach predict electron thermalization times t_{th}, obtained from single electron-electron inelastic relaxation lifetimes τ_{ee}, of hundreds of femtoseconds to a few picoseconds, casting doubt on the validity of the 2TM [96, 129]. However, for ferromagnetic metals such as Ni, Fe and Co the measured lifetimes of low

energy excitations are on the order of a few femtoseconds only, considerably smaller than those resulting from the FLT. This is mainly due to their d-type bands being close to, or intersecting with, their Fermi levels, which provides additional phase space for scattering events and turns them into rather poor Fermi liquid candidates [22, 290]. Since the thermalization time is dominated by the longest inelastic lifetimes, it can be inferred that actual thermalization in these materials would proceed faster. Subsequent experiments based on time-resolved two-photon photoemission spectroscopy (TR-2PPES) have tried to retrieve an integrated value of the thermalization time through different methods. Van Kamper *et. al.* have reported $t_{th} \approx 80\,\mathrm{fs}$ for Ni [130], whereas Mueller and colleagues recount values between approximately 18 fs and 43 fs depending on the absorbed pump fluence [183].

It must be noted here that TR-2PPES, although providing the most direct access to the electron inelastic lifetimes, is not without experimental contingencies. Several secondary processes such as cascade electrons, Auger decay or transport effects can distort the measurements and need to be taken into account when computing τ_{ee}. More importantly, TR-2PPES requires very low excitation densities, which translates into pump-probe fluences on the order of a few hundred $\mu\mathrm{J\,cm^{-2}}$. In this regime, scattering among the excited electrons is negligible, the dominant decay channel being e-e scattering within the electron liquid below E_F [141]. In fact, the aforementioned studies by Mueller show evidence that higher fluences, as well as high electron temperatures, lead to a drastic decrease of the thermalization time. In contrast, demagnetization of thin films require pump fluences on the $\mathrm{mJ\,cm^{-2}}$ range, where higher excitation densities could favor further scattering mechanisms. Thermalization in this case could take place within a small fraction of the demagnetization timescale, allowing for equilibrium temperatures to be defined according to the 2TM [270]. All in all, it is still an ongoing debate whether the thermalization assumption is fully justified for ferromagnetic metals, but it is certainly a factor to contemplate when modeling ultrafast demagnetization.

On the spatial diffusion assumption

Besides the thermalization assumption, both the 2TM and 3TM operate under the condition that no spatial diffusion takes place. Roughly speaking, an electron with a typical velocity of $10^6\,\mathrm{m\,s^{-1}}$ inside a metal would take only 10 fs to cover a distance of 10 nm, which corresponds to the penetration length δ_{opt} of infrared light in most metals. The timescales for ballistic transport outside the area of interest are then on the same order of magnitude than the inelastic relaxation lifetimes and need to be considered in the calculations. This has been demonstrated experimentally, such as in the works of Hohlfeld and Garduño-Mejía with gold [86, 111]. The latter made use of a modification of the 2TM after Carpene [41], wherein diffusive as well as

non-thermal effects were considered. Further evidence of diffusion mechanisms has come from the observation of anisotropic ballistic motion due to non-spherical Fermi surfaces in some metals [105, 104, 164]. Of particular relevance is the fact that relaxation times rapidly increase well above a few tens of fs for low excitation energies, which gives rise to diffusion (as well as other relaxation channels such as electron-phonon or defect scattering) becoming the dominant factor [143]. Indeed, transport effects have been accounted for through several approaches beyond the 2TM [5, 39, 112, 141, 143, 142]. Alternatively, transport effects can be considerably minimized by appropriate experimental design. For instance, films of thicknesses comparable to the optical penetration length of the relevant material can help confining the excited electrons within the probed surface region [5]. In a similar manner, some polycrystalline samples have shown longer relaxation lifetimes at low energy excitations than their single-crystal counterparts, a phenomenon that has been attributed to elastic scattering at grain boundaries impeding carrier diffusion [3].

Transport of spin carriers not only represents a channel for the loss of spin in magnetic materials, but can also directly affect their magnetization properties through net spin transfers. For instance, Malinkowski and co-workers first showed in 2008 that direct spin transfer between two ferromagnetic layers separated by a spin conductor could both speed up and enhance ultrafast demagnetization [168]. Moreover, when the interlayer was comprised of a spin insulator, the effect was lost, proving that a net spin current was the responsible mechanism. This experiment has been later reproduced with similar results by von Korff Schmissing [150]. Rudolf *et. al.* further demonstrated that, in a similar spin valve of Ni/Ru/Fe, ultrafast demagnetization of the first ferromagnet could even induce a net magnetization on the second one through pure spin transport [225], an observation that has been verified and extended by Mathias and Turgut [173, 258], and theoretically examined by Yastremsky [278]. Several recent studies have added support to the validity of nonlocal ultrafast demagnetization and spin reversal due to transport mechanisms [94, 175, 265].

In light of this evidence, Battiato and his colleagues proposed in 2010 an ultrafast demagnetization model based on a superdiffusive mechanism without the need of on-site dissipation of angular momentum. This model is based on a semiclassical description of laser excited non-equilibrium electrons that undergo both elastic and inelastic scattering on their way out of the probing region. Since both the mean free path λ of the electrons and their average velocity v inside the material are on the order of the relevant experimental scales (for instance, $\lambda \approx 10\,\mathrm{nm}$ and $v \approx v_F$, where v_F is the Fermi velocity, on the order of $1\,\mathrm{nm\,fs^{-1}}$ for most metals), Battiato argued that the standard diffusion regime, which assumes small λ and large v, is insufficient to describe the transport dynamics. On the other hand, ballistic

transport alone cannot account for the scattering processes electrons are subject to [37, 50]. Therefore, a unifying model is needed that can describe the electronic motion on different length and time scales. In general, it is indeed accepted that standard Fourier diffusion breaks down under length and time scales on the order of the mean free path λ and the average relaxation time τ, respectively [103]. In this first microscale regime the Boltzmann transport equation (BTE) is taken instead to follow the time evolution of the carrier distribution. In fact, this treatment has been extensively used for the study of electron transport in metals [50, 143], however obtaining a numerical solution is computationally demanding and several strong approximations are commonly taken. The superdiffusive model proposed by Battiato also starts off from the BTE, but it integrates the dispersive behavior of the electron motion in an analytical way, thereby sidestepping approximations such as the relaxation time or the thermal equilibrium assumption.

The lack of fitting parameters in this model is an important step towards an accurate *ab initio* calculation of femtosecond magnetization dynamics, yet the introduction of some approximations is still unavoidable. For instance, refraction of the electron momentum in the interfaces has been neglected. Also momentum correlations upon inelastic scattering and the additional delayed generation of Auger electrons have not been included in the derivation, which leads to an underestimation of the diffusion process [20]. Although electron thermalization is fundamentally coupled to the transport equation in Battiato's model, an effective comparison between the ballistic and diffusive regimes of transport can be performed, in which the anomalous diffusion exponent parameter[1] becomes itself a function of time that changes from the ballistic to the diffusive regimes in a timescale of 100 fs.

While superdiffusion has been referred to as the underlying mechanism in some measurements on multilayer or even magnetic nanodomain thin films [72, 132, 172, 175, 197, 225, 228, 231, 258, 264], several authors report a rather mince influence of spin transport in similar experiments. Schellenkens *et. al.*, for instance, showed that exciting a Ni film from either the front or the back surface, while probing it from the front, has no effect on the demagnetization amplitude, concluding that no trace of spin transport can be observed [229]. Additionally, they couldn't reproduce the magnetization transfer in FeNi bilayers exhibited by the study of Rudolf *et. al.* with an alternative method [230]. In apparent contradiction with the investigations of Vondungpo [264] and Pfau [197] on spin transport with CoPd and CoPt multilayered films, Moisan and colleagues report that, for similar samples, hot electron spin transfer does not influence the demagnetization dynamics[2] [178]. Quantita-

[1] In the anomalous diffusion theory, the mean squared displacement σ^2 of a particle is a power law function of time, $\sigma_2 = Dt^{\alpha}$, where $\alpha = 1$ corresponds to standard diffusion, $\alpha > 1$ to superdiffusion and $\alpha < 1$ to subdiffusion. D is termed the standard diffusivity.

[2] For details on the treatment of interface reflections in heterostructures within the su-

tively, a critical factor of the superdiffusive theory is that, since it is build with the absence of fitting parameters, it heavily relies on the accuracy of the spin- and energy-dependent values of the electronic inelastic lifetimes and velocities and, more importantly, on their spin ratios $\tau_\uparrow/\tau_\downarrow$, since the latter will influence to what extent net spin transfers are to account for the demagnetization dynamics. In the original work from Battiato, these values are extracted from Zhukov's *ab initio* calculations [292], based on the GW+T approximation of the Green function expansion within the many-body quantum theory [8, 291]. Comparison with TR-2PPES measurements in Fe, Ni and Co shows not only an overestimation of the spin-integrated lifetimes (at least for excitation energies below 2 eV), but also a considerable discrepancy in the spin ratios [23]. For instance, the theoretical ratio for nickel is around 8, whereas a value of only 2 is measured. A similar variation is apparent in Co, where almost no difference between majority and minority lifetimes is actually observed [93]. Such discrepancies have been ascribed to exchange scattering during inelastic relaxation in combination with secondary electron generation. Kaltenborn and Schneider have also demonstrated that incorporating spin-orbit coupling effects in the GW+T framework, which allow for spin-flip transitions, better explains the measured inelastic lifetimes in metals [127, 128]. For iron, on the other hand, both theory and experiment agree on an inelastic lifetime ratio very near 1. In this case, though, the spin asymmetry is found in the electron velocities, since the presence of empty d bands for the minority spin states greatly reduces their group velocities in contrast to the high delocalization of majority spin states. Although velocities are evaluated from band-structure calculations, the product $v(E)\tau(E) = \lambda(E)$, called the inelastic mean free path (IMFP), can be obtained from spin-transport experiments [67, 123, 217]. In Zhukov computations, theoretical IMFP values from the GW+T method are compared with data from permalloy samples published by van Dijken [67], however Banerjee and co-workers report values at least three times lower for simple Fe layers and a visible disagreement with the theory [16]. In view of the previous considerations, then, the possibility that superdiffusion in single-layer 3d ferromagnets has a smaller influence than expected can't be discarded.

On the delta-pulse assumption

There is yet an extra condition under which the 2TM and 3TM from Beaurepaire operate after the instantaneous thermalization and the absence of diffusion: a delta-pulse laser excitation is assumed. This is not an irrelevant presumption, since excitation pulse lengths of current light sources lie in the range of 20 fs to 50 fs FWHM, which is only a few times smaller than,

perdiffusion scheme see [21]

but on the order of, demagnetization timescales. Variations in the excitation length during the demagnetization process could dynamically affect the fundamental interaction mechanisms as well as their associated timescales. Finite-pulse excitations, as well as absorption effects, can be included in the 2TM/3TM by means of a space- and time-dependent source term. Nevertheless, the role of the pulse length in demagnetization events is a relevant study to consider. This role will be inspected in section 2.4.

Photon-electron interaction

Despite the remarkable ability of the 3TM to describe demagnetization dynamics with its strong assumptions, and even when these assumptions are addressed by the modification of the equations as commented above, this model has a fundamental limitation. It does not provide us with an appropriate microscopical description of the transfer of angular momentum. Since the total angular momentum of a free electron sea is conserved, how exactly do electrons interact with the resting degrees of freedom in a ferromagnet to deploy their initial angular momentum in a sub-picosecond timescale? In Batiatto's superdiffusive approach this question is sidestepped because spin-transport asymmetries leave the fate of angular momentum to rather unspecified rebalancing mechanisms outside the probed region (for instance spin-flips in boundaries and interfaces or slower spin-phonon relaxation). Notwithstanding, several other approaches have been taken after Beaurepaire's findings in 1996 to solve this enigma. The first attempt was made in 1998 by Hübner and Zhang. In a series of publications [114, 118, 282, 285, 284] they construct observables such as the magneto-optic Kerr signal, the reflectivity or the second harmonic generation (SHG) signal from first principles by means of a many-body Hubbard-like hamiltonian that includes the band structure, the electron exchange interaction and the on-site spin-orbit coupling. Additionally, they incorporate the laser effects as an external field. It is argued that the interplay between the laser field, the exchange interaction and the spin-orbit coupling determines the spin dynamics, which intrinsically occur on a timescale of 10 fs. In this case, the laser pulse length would still be limiting the possibilities of ultrafast dynamics. This needs to be set in contrast, however, with the facts that for Fe and Ni the demagnetization time constant in the 100 fs range has been consistent in time across experiments with a variety of techniques, pump pulse lenghts and fluences [11, 30, 42, 72, 149, 172, 223, 229, 243, 244, 258], in contradiction with the model from Zhang and Hübner. In 2003 Koopmans *et. al.* questioned the validity of this model with an estimation of the prohibitive amount of photons needed for such an angular momentum transfer to take place [145]; and in 2007 Dalla Longa and co-workers determined a virtually null influence of the photon field in the demagnetization of Ni [60]. Also Fähnle and Illg, in his 2011 review, support incoherent effects over direct photon-electron

momentum transfer [75]. It has been argued that, even if the electron spin orbital momentum is transferred to the electron orbital degree of freedom via electron-photon interaction in an ultra-short timescale, eventually the lattice needs to absorb the total momentum for the demagnetization to take place, thereby acting as a bottleneck [119]. Nevertheless, the debate has kept growing ever since. For instance, the demonstration of all-optical magnetic switching with circularly polarized laser pulses in 2007 [245] constituted a breakthrough for the manipulation of magnetic ordering by light. The photon shortage claimed by Koopmans has also been addressed by Si and Zhang [238]. In 2009 Bigot, Vomir and Beaurepaire went a step further and suggested a light-induced coherent spin-flip mechanism of ultra-relativistic origin [30], a theory that has been recently challenged from *ab initio* investigations [179].

Spin-flip approaches and the Elliot-Yafet scattering

Since the angular momentum during a demagnetization process needs to be eventually transported out of the electron system, it is widely believed that the lattice needs to intervene as a transfer mechanism [119]. Thus, concurrently with the promotion of the electron-photon theories, approaches were also developed whereby spin-flipping events, usually through in-place scattering, could take place. In this line, a remarkable theory proposed by Koopmans in 2005 gained a great deal of attention [147]. In this theory, the Boltzmann equation is employed with the possibility of a spin-orbit-induced spin scattering by phonons known as Elliott-Yafet scattering. This type of spin-phonon scattering was introduced as early as 1953 by Overhauser [192], when he connected lattice vibrations and electron spins through the current-induced magnetic field generated by the former. A year later Elliott highlighted that, due to the spin-orbit coupling, the spin state of an electron in a crystal should be a momentum-dependent asymmetric mixture of the spin eigenstates of a free electron [69], which implied an additional contribution to the spin-lattice relaxation by Overhauser. Shortly thereafter, Yafet calculated the spin-flip matrix from the electron-phonon mechanism that included both contributions [17, 277]. Koopmans used this spin-flip probability in his calculations and showed that a loss of magnetization within a sub-picosecond timescale was feasible and could even account for the different demagnetization regimes observed in rear-earth metals such as gadolinium [149, 223, 261]. Although subsequent reports have shown support for the Elliott-Yafet mechanism [52, 243, 244, 247, 249, 248, 273], recent *ab initio* computations from independent authors conclude that, albeit present, it is not strong enough to account for the observed quenching of the orbital momentum [46, 44, 74, 119]. To this regard, Haag and co-workers advocate for electron-magnon interactions as an additional spin-flip contribution to the Elliott-Yafet scattering [101]. Spin relaxation through magnons had already

been scrutinized in the late 1990s [202] and has been taken into consideration for ultrafast demagnetization models both experimentally [42, 55, 259] and theoretically [100, 170]. Alternatively, Krauss and his colleagues defended in 2009 the possibility of an Elliott-Yafet type of scattering between only electrons without the need of a phonon bath [152]. Their computations agree with the experimental data for Ni and Co when the spin-orbit coupling constant and the fluence are conveniently fitted. Further approaches of this proposal included the phonon contribution with remarkable success [182, 185, 184].

Finally, it is worth mentioning studies making use of extended versions of the Landau-Lifshitz-Gilbert equation commonly used to describe dissipative magnetization dynamics. The reader is referred to the following studies: [10, 11, 75].

All in all, the passionate debate maintained in the scientific community makes it evident that the underlying mechanisms for ultrafast magnetism are not fully understood and might depend on the precise characteristics of the sample, the excitation source and the experimental setup in a stronger way than expected. In the following sections, some experiments will be shown that address the assumptions of the 3TM for the ultrafast magnetization dynamics for nickel. Also a comparison with the predictions of the Koopmans model will be presented in a double pump pulse experiment and the effect of diffusion in indirectly pumped samples will be examined. clues on the ultrafast magnetization dynamics in nickel.

2.3 Experimental setup

The employed experimental technique in the following sections to measure the magnetization is the time-resolved transverse magneto-optical Kerr effect (MOKE) in the longitudinal geometry, although some minor modifications in the setup have been implemented in each particular case. The complete setup is shown in fig. 2.1. Femtosecond infrared pulses of 800 nm from a Ti:Sapphire amplified laser[3] are delivered with a repetition rate of 10 kHz, a pulse energy of 1 mJ/pulse, an average power of 10 W–12 W and a minimum length of 17 fs (FWHM from a lorentzian profile auto-correlation fit). Most of the laser power (8 W–10 W) is sent to the pump branch while the rest is left for the probe. Along the pump branch the pulses first undergo pulse compression inside the amplifier system. Afterwards, they are regulated in intensity by a $\lambda/2$ plate plus a polarizer and then chopped out at a 83 Hz rate. In the next stage the beam is divided into two copies by

[3]The laser source includes an oscillator (Vitara) and an amplifier (Evolution) with a combination of a regenerative- and a single-pass amplification stages. Acquired from Coherent Inc.

a beam splitter. Each of them is passed through an automated delay line for independent arrival time control and its intensity is further regulated by a $\lambda/2$ plate and a polarizer. From there, several configurations can be employed. Only one of the pulses can be used, for instance, in a customary pump-probe setup such as in the pulse length experiment or in the Al/Ni diffusion experiments, where the sample is pumped from the back surface. Alternatively, both pulses can be directed to the front part of the sample for a double pulse experiment, or each one in an opposite surface as in a front-back pulse configuration. Moreover, both the pump(s) and the probe are subject to a spatial beam stabilizer mechanism in order to minimize long-term drifts generated in the amplifier cavities and temperature sensitive optical elements, which could affect experimental conditions ranging from the spatial pump-probe overlap to the performance of optical components such as reducing telescopes. The mechanism involves a set of piezo-driven mirrors and photo-detectors operating within a feedback loop software routine (PID regulator).

On the probe side, the beam is first directed to a pulse compressor, then intensity-regulated and finally up-converted to a wavelength of 400 nm by a barium-borate (BBO) crystal. The output beam is immediately cleansed from its base infrared frequencies through a set of dichroic mirrors acting as a band pass filter[4]. The use of 400 nm radiation for probing the magnetization procedure is aimed at circumventing any possible state-blocking effects (or *dichroic bleaching* as reported by Koopmans [146]), to which reliability issues of the magneto-optical signal have been attributed [45, 189, 212, 268]. On reaching the sample, the polarization of both the pump(s) and the probe is parallel to the worktable (p-polarization). A magnetic field of 20 mT is applied to the sample in the longitudinal direction. Each sign $(+,-)$ of the field is henceforth denoted $\uparrow,\downarrow$. After the sample, dichroic mirrors ensure that no base frequency components of the deviated pump can reach the detector, which is itself isolated to avoid any further stray light contributions. The detector comprises a $\lambda/2$ plate and a Wollaston prism coupled to a pair of balanced photo-diodes connected to a lock-in amplifier. The $\lambda/2$ plate is adjusted so that an equal intensity reaches each photo-diode. This way, only variations from the pump-induced Kerr signal are recorded and systematic errors coming from laser fluctuations or changes in the reflectivity are conveniently minimized. Additionally, a $\lambda/4$ plate is installed to remove spurious elliptic contributions from the Kerr signal.

In the present setup, measuring the change of rotation of the polarization $\Delta\theta_{\uparrow,\downarrow}(t)$ is preferred over the change in ellipticity. It is argued, in this approach, that the reaction of the rotation to the pump excitation is slower

[4]The mirrors are optimized for p-polarized light, with high reflection in the 400 nm window and high transmission in the 800 nm range.

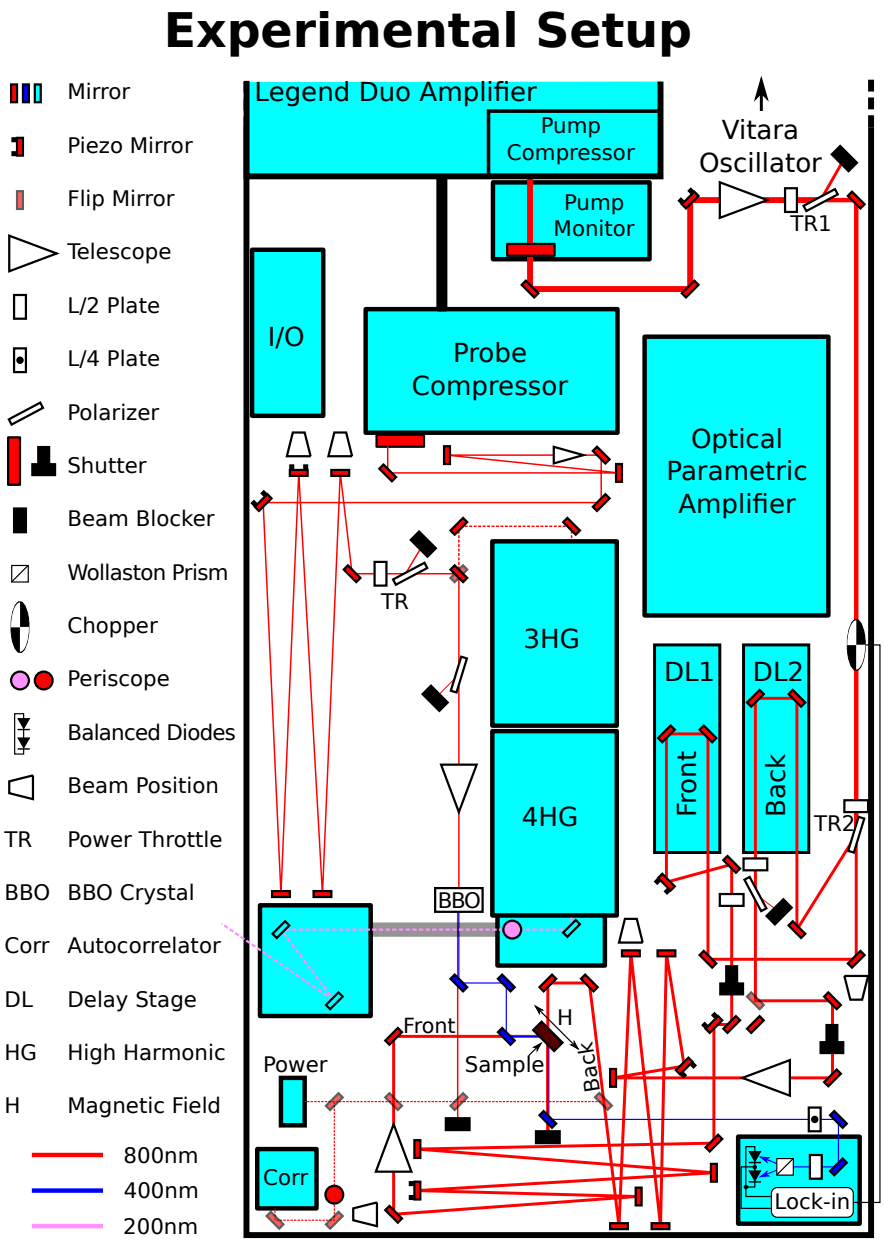

Figure 2.1: Layout of the table-top laser system and the MOKE configuration employed throughout the text. Some elements such as the higher harmonics stages or the optical parametrical amplifier are aimed at future experiments.

than the ellipticity, which makes the former less prone to be affected by quasi-instantaneous charge redistribution, therefore better suited to represent the actual optically induced magnetization dynamics [30]. The change in polarization rotation can be obtained for each magnetization direction $(\uparrow, \downarrow)$ as it is proportional, for small angles, to the measured photo current, $\Delta I_{\uparrow,\downarrow} \propto \Delta\theta_{\uparrow,\downarrow}$. The relative magnetization change can be retrieved as

$$\frac{\Delta M(t)}{M_0} = \frac{\Delta\theta_{\uparrow}(t) - \Delta\theta_{\downarrow}(t)}{\theta_{\uparrow} - \theta_{\downarrow}} \tag{2.1}$$

with $\theta_{\uparrow,\downarrow}$ defining the static value of the Kerr rotation (i.e. the value before the pump has acted). Eq. 2.1 is only valid when the optically induced change in reflectivity of the sample, which determines the charge dynamics, is small compared to the variation in the Kerr signal [43]. In this case, the charge contribution to the Kerr signal is marginal and, under the linear magneto-optical response assumption, the latter is proportional to the magnetization M.

2.4 The effect of the pump pulse length in the demagnetization process

As discussed in section 2.2, delta-pulse excitations are an implicit assumption in the 3TM model of the demagnetization. Currently available pump pulses, however, are on the order of several tens of femtoseconds, which is comparable to the well-observed demagnetization times $\sim 100\,\text{fs}$. For this reason, it is of interest to examine the effects of pulse length to demagnetization processes. In this approach[5], demagnetization of nickel thin films is tested for different pump pulse lengths.

2.4.1 The pulse length experiment

In fig. 2.2 (a), a reduced schematic for the pulse length experiments is shown. The pump pulse compressor allows for the variation of the pulses from around 20 fs to several ps. The pulse energy is nonetheless kept constant at 88 µJ, which results in an incident pump fluence of $1.5\,\text{mJ}\,\text{cm}^{-2}$. Notice, however, that the absorbed fluence might be considerably lower than this value due to reflections in the outer and inner Ti layer. On the other line, the probe's own pulse compressor is adjusted to deliver the shortest possible pulses. These correspond to an autocorrelation trace of 40 fs FWHM, which can be converted back to a lorentzian pulse shape of approx. 20 fs. During the measurements the sample is magnetized to saturation with an external in-plane magnetic field $H = \pm 15\,\text{mT}$ in opposite directions (the coercive field determined from the hysteresis loop reads $H_C = 6.3\,\text{mT}$). The

[5] Part of this section has been published in [83].

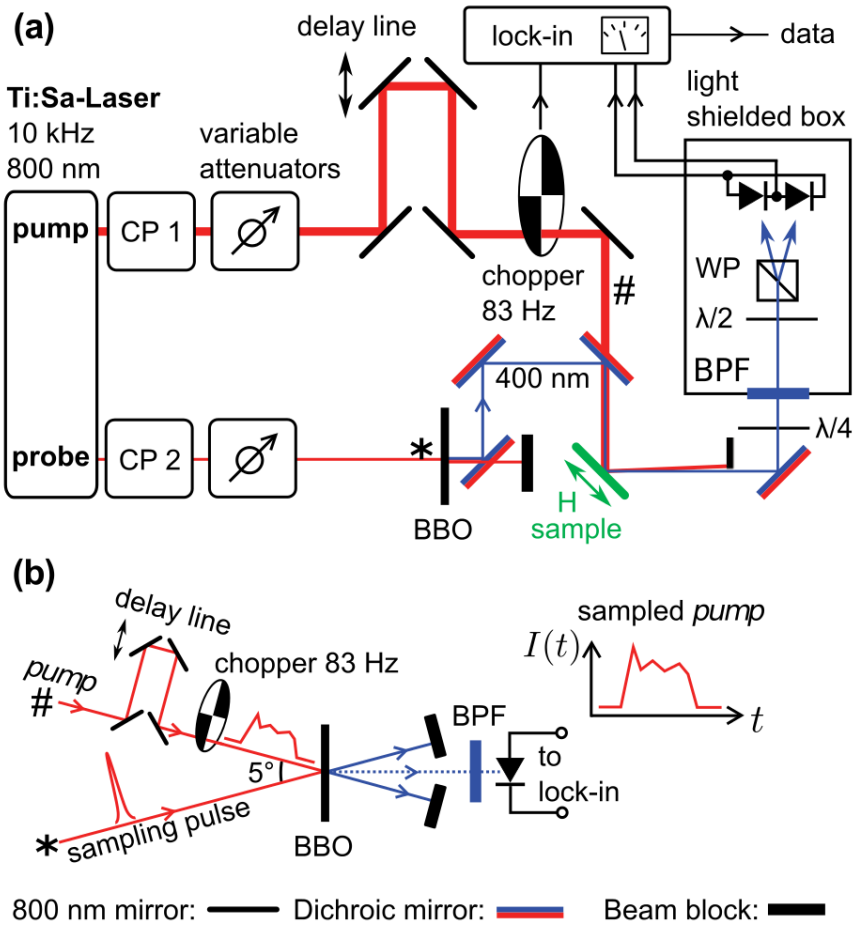

Figure 2.2: (a) MOKE experimental setup for the pulse length variable measurements. The length of the pulses is adjusted through the pump and probe pulse compressors. State-blocking effects are avoided by using a band pass filter with a frequency doubler crystal and a set of dichroic mirrors. (b) Schematic representation of the cross-correlator employed to measure the pulse length, using a 20 fs, 800 nm pulse to sample the pump via up-conversion in a BBO crystal. Reproduced from [83]

sample consists of a 20 nm thick nickel film grown by electron beam evaporation on a standard glass substrate. The film has been structured as 5 nm Cr/50 nm Cu/20 nm Ni/3 nm Ti for the following reasons. The material of the thin capping layer, which prevents nickel oxidation, should be chosen to minimize any additional contributions to the Kerr signal. Since the spin-orbit coupling is the driver of the magneto-optical Kerr effect [7] and since it roughly scales with the atomic number, $H_{SO} \propto Z$, a reasonable choice seems to be the low-Z element titanium. The seed layer is made of chromium with an interlayer of cupper intended to promote a flat film growth.

The length of the pump pulse, modified through the pulse compressor, has been measured with a cross-correlation setup shown in fig. 2.2 (b). For short pulses of several tens of femtoseconds the auto-correlation technique is suitable because a nearly gaussian pulse shape can be safely assumed. However as the compressor lengthens the pulse, its profile becomes severely distorted. The lack of symmetry then requires a cross-correlation to be employed, whereby a short sample pulse of fixed length (20 fs) is overlapped with the variable length pulse in a BBO crystal. The resulting intensity profile is measured in a photo-diode, as fig. 2.3 exhibits. For simplicity, the auto-correlation of the same pulses has also been recorded (inset of fig. 2.3) and the FWHM of the corresponding lorentzian fits used as labels for the pulse lengths.

2.4.2 Results and discussion

Pump pulses with lengths from 40 fs to 7 ps give rise to the demagnetization dynamics displayed in fig. 2.4 (a). For lengths below 1 ps a clear ultrafast demagnetization followed by an also fast remagnetization within the first few picoseconds is observed. Shortly after, the signal stabilizes in a slower remagnetization curve lasting several tens of picoseconds. For lengths above 1 ps, though, the signal does not follow a fast demagnetization curve but rather a slow magnetization decay of up to 6 ps. After this time all traces converge to the same curve. This indicates that, after approx. 6 ps, the magnetization dynamics is mainly determined by the total energy of the pulse, and not by its length or shape. Independently of the pulse length, then, remagnetization dynamics, at least at such timescales, can be established by a definite common temperature between the electron, the spin and the lattice reservoirs. This is in agreement with earlier experiments [149, 270], in which a time of around 2 fs is needed for the lattice to thermalize. Further support is found in studies of variable laser fluence where the remagnetization time constant τ_R is seen to increase linearly with the fluence [68, 150], pointing to the total power absorbed as the cause for the change in τ_R. The maximum demagnetization of 5 % is achieved with the shortest pulse of 40 fs. Two regimes are clearly devised in the dependence of the maximum amplitude

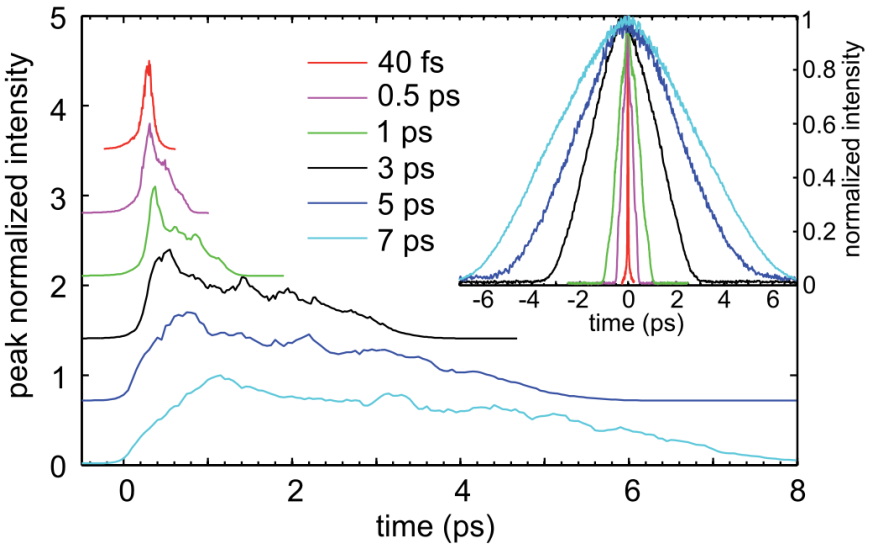

Figure 2.3: Measured pump pulse profiles from the cross-correlation setup and the corresponding auto-correlation traces (inset), whose gaussian fit FWHM values are used as labels for each pulse length. Reproduced from [83]

.

with the pulse length. For pulses shorter than circa 2 ps a strong dependence is found with a slope $m_{<2\,\mathrm{ps}} = -1.5\,\%\,\mathrm{ps}^{-1}$, whereas pulses over 2 ps long show a weaker dependence with a slope $m_{>2\,\mathrm{ps}} = -0.2\,\%\,\mathrm{ps}^{-1}$, almost a factor of 7 smaller. The crossover between the two regimes at roughly 2 ps corresponds to the electron-phonon thermalization time mentioned above. As a reference, a demagnetization of 3 % corresponds to a temperature increase of 50 K [56]. Notice from fig. 2.3 and fig. 2.4 (b) that the peak intensity for longer pulses occurs long before the magnetization reaches its minimum. For instance, the pulse with an auto-correlation of 3 ps has its intensity peak around 0.25 ps, but the corresponding demagnetization curve has its minimum at 3 ps. In fact, a closer look at fig. 2.4 (b) reveals that there is an almost one-to-one correspondence with the time of the maximum demagnetization and the pulse length as determined by its auto-correlation trace. Roughly speaking, as long as pump power is applied into the system, demagnetization takes place. Fig. 2.4 (a) also shows that the remagnetization process has two regimes. The fast regime is only visible for pulses shorter than 2 ps. Pulses longer than this time are concealing fast remagnetization dynamics and the associated demagnetization amplitudes are only weakly dependent on their length. Hence the question arises: is this simply a consequence of the pulse length or do different mechanism undergo in each

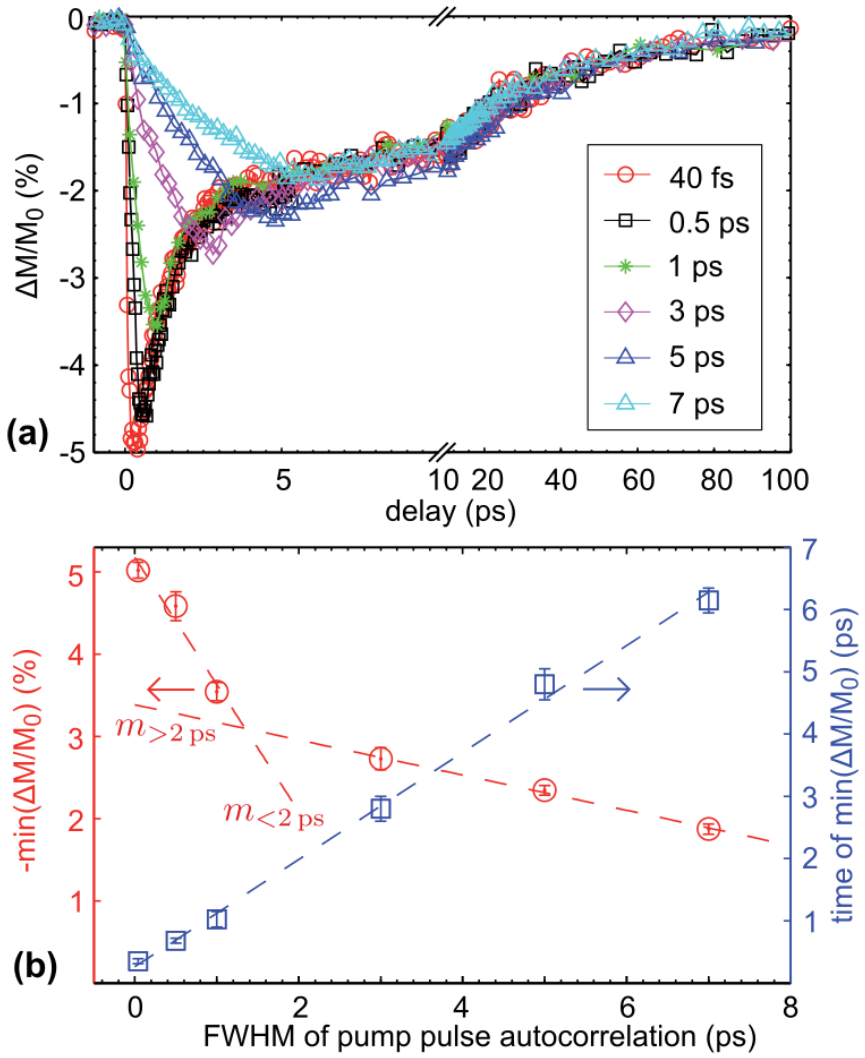

Figure 2.4: (a) Time-resolved relative demagnetization for different pulse lengths. (b) Time position and amplitude of the maximum demagnetization for each pulse length. Reproduced from [83]

remagnetization regime? The following argument should shed some light on this topic. If the magnetization reacts in a linear manner to the excitation pulse, the magnetization response $M\{p\}(t)$ for any pulse shape $p(t)$ can be reconstructed as

$$M\{p\}(t) = (M\{\delta\} * p)(t) \tag{2.2}$$

where $M\{\delta\}$ is the magnetization curve for a delta pulse. Given the difference between the shortest pulse available of 40 fs and the longer ones up to 7 ps, the fastest demagnetization curve in fig. 2.4 (a) can be used as a substitute for the delta response. For this purpose a fit of this curve using eq. 1.7 has been performed, and its convolution with each pulse profile from fig. 2.3 has been computed. The results are depicted in fig. 2.5. Clearly, the calculated convolutions match the experimental demagnetization curves for pulses longer than 40 fs. This indicates that the different remagnetization regimes observed in 2.4 (a) might undergo the same dynamics. In this case, slower spin-flip types of scattering, for instance mediated by phonons, magnons or a combination thereof [119], could be a good candidate for the underlying mechanism. The same conclusion can be drawn from experiments with varying laser fluence where the pulse length is kept constant [9, p. 61]. Note also that the remagnetization for the 40 fs curve seems to be also reproduced by the rest of the curves, particularly for the pulses below 2 ps. This shows, that the process is linear with the deposited pump pulse energy, at least for the small demagnetization amplitudes seen here.

As stated above, 2.4 (b) shows that the initial demagnetization rate is limited by the pulse length. However, this is not true for the shortest pulse of 40 fs, for which the curve minimum lies at $t_{min} \approx 300$ fs (accounting for an exponential decay on the order of 100 fs). This timescale has been confirmed repeatedly in all 3d ferromagnets [11, 30, 42, 72, 149, 172, 223, 229, 243, 244, 258] for pulses as short as 25 fs, and it is reproducible in all of the experiments provided in the current thesis. This represents a fundamental limit on the demagnetization process and dismisses earlier claims that shorter demagnetization rates were to be expected [114, 118, 282, 285, 284]. Crucially important, it answers the question, at least qualitatively, on whether the delta-pulse assumption used in the base form of the 2TM and 3TM is acceptable [242]. That is, for pulses visibly shorter than the demagnetization timescale of ≈ 100 fs, an equivalent delta-pulse could still describe the same dynamics. This is compatible with the 3TM by Beaurepaire [26], in which the set of differential equations utilized behaves linearly for low temperature differences (see also eq. 2.8 in section 2.5.3 for comparison). The relatively weak coupling between the electron and spin systems and the increasing spin heat capacity with temperature makes the latter react at a slower rate, therefore setting a limit for the time in which the magnetization (that is proportional to the spin temperature in first approximation) can fall down.

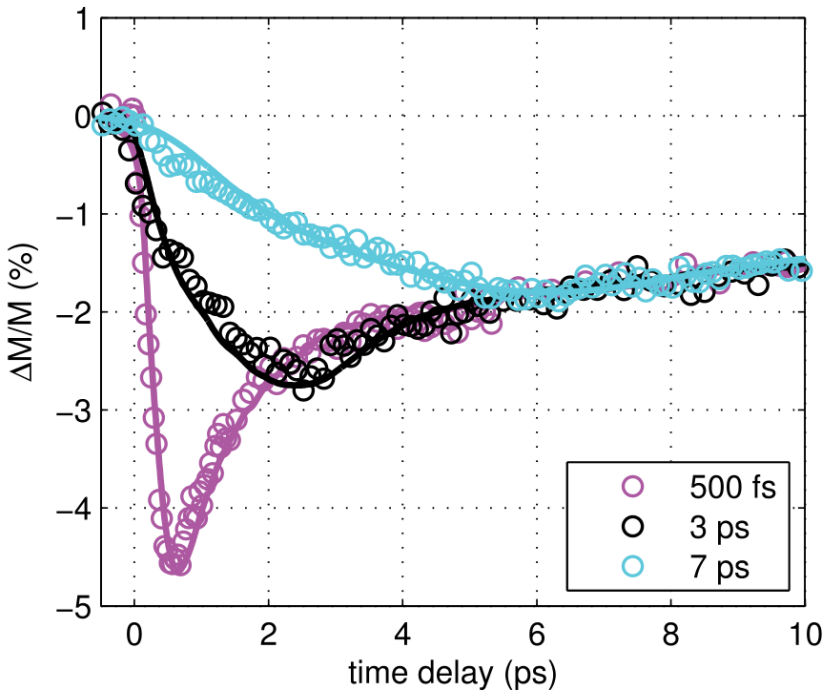

Figure 2.5: Selected experimental demagnetization curves (circles) and the convoluted curves from eq. 2.2 (solid lines) confirm that remagnetization dynamics from picosecond pulses can be reconstructed from femtosecond pulses. Reproduced from [83]

However the underlying mechanism are not described in this model, and a microscopic picture is needed to fully understand the process.

2.4.3 Conclusions

This experiment demonstrates that the demagnetization curve of nickel thin films by a picosecond laser pulse can be reconstructed from the response to a femtosecond pulse. Therefore, femtosecond demagnetization dynamics contain all the information for picosecond dynamics and are driven by the same mechanism, the coupling between the electrons and the lattice being an acceptable candidate thereof. Nonetheless, pulses longer than 2 ps conceal the regime whereby thermalization of the electron sea to the lattice is taking place, in agreement with previous measurements. The pulse length thus limits fundamental demagnetization rates only for lengths over 100 fs. This is in line with the 3TM, in which the spin temperature has an inherent delay over the electron temperature. A microscopic description of the demagnetiaztion process is however required if the underlying mechanism for angular momentum transfer are to be fully understood.

2.5 The effect of heat in the demagnetization process

In section 2.2 concerns around the assumption of an instantaneous thermalization of the electron sub-system have already been brought up. The generation of non-equilibrium electron distributions by femtosecond laser excitations in metals has been repeatedly confirmed, in both indirect reflectivity-based measurements [32, 64, 65, 96, 111, 235, 253] and direct observations of electronic distributions from 2PPE experiments [3, 4, 22, 40, 39, 77, 76, 141, 163, 162, 161, 198, 214]. The evidence shows that right after the initial excitation the electron system is brought into a strong non-equilibrium condition. Within the first few hundreds of femtoseconds mainly electron-electron interactions drive the system into a Fermi-Dirac distribution whereby a temperature can be defined. In parallel with this short-term *internal thermalization* [198], electron-phonon collisions push the lattice and the electron sub-systems into a common temperature whence the cool down takes place. The characteristic times of this *external thermalization* range from a few hundreds of femtoseconds to several picoseconds, which sometimes blurs the line separating the two processes [198]. In this sense, laser excitations that last longer than the internal thermalization time τ_{th} cannot reveal this ultrafast process, assuming an equilibrium temperature for each sub-system. The 2TM and 3TM may thus be applied in such cases provided that transport mechanisms and real pulse excitations are included. Withal, the aforementioned experiments on hot electron dynamics are mainly focused on noble metals. Ferromagnetic certainly possess some distinctive features. For instance, their d-bands are closer to the Fermi level, conferring them characteristic DOS spectra[6], and the inherent spin asymmetry adds an extra degree of freedom to the system, which translates into a net angular momentum and a macroscopic magnetization. It is therefore relevant to inspect how these electron dynamics translate into the magnetization dynamics. In other words: how is the demagnetization process affected, if at all, by the state of the electron sub-system and its interaction with the lattice?

In the standard 3TM, the couplings between the reservoirs are constant and the equations remain linear for low excitations[7]. However, the more sophisticated models based on spin-flip scattering, such as that from Koopmans [147, 149], involve phonon-mediated interactions between the electron and the spin sub-systems, which results in nonlinear equations. In particular, the modified three temperature model (M3TM) by Koopmans predicts an enhancement of the demagnetization when a previous pump has pre-heated a ferromagnetic sample such as nickel within a short time delay, as section

[6] reflectivity measurements, for instance, are known to be specially sensitive to the electronic structure of metals [112].

[7] Nonlinearities are mainly introduced through the temperature-dependent heat capacity

2.5.3 further reveals. Testing for this nonlinearity is an important step toward shedding light on the question previously stated. For this purpose, an experiment has been designed to overcome the difficulties of single pump-probe measurements in relating the Kerr signal changes to the electron and phonon temperatures. It introduces a *double pump* technique in the spirit of early research on electron dynamics [32]. That is, by varying the time delay between two pump pulses, a study of the demagnetization at different excited states of the electron and lattice sub-systems can be performed. First, the double pulse experiment will be explained with some detail. Then, an analysis of the nonlinearity of the system response will be presented. Finally, a simulation of the same experiment using the model introduced by Koopmans will be undertaken and compared with the data.

2.5.1 The Double Pulse experiment

For the current experiment a nickel sample layered as 3 nm Ti/ 20 nm Ni/3 nm Ti by e-beam evaporation was chosen. Since the amount of absorbed heat by the target film is an important parameter in this experiment, extra layers besides the thin anti-oxidizing titanium capping would complicate the observations unnecessarily. The setup depicted in fig. 2.1 has been used, this time directing the beams from each delay line (DL1, DL2) into the same sample face. Since the path followed by each beam line is different, an offset delay between them needs to be set by matching the zero time of the demagnetization traces obtained with each beam independently. This offset then corresponds to a zero pump-pump delay. Both delay stages then move together to map the probe arrival time for each fixed pump-pump delay. The pump doubling is achieved through a 50 % beam splitter that ensures pulse copies of similar energy. After each line, a polarizer plus a $\lambda/2$ plate provide power regulation (variable attenuator), which can be used either to set independent pulse powers or to adjust power variations from splitting asymmetries. The adjustment is made by setting the transmission values T_1 and T_2 (in %) that translate into a calibrated variable attenuator angle of the $\lambda/2$ plate. To calculate the fluence of the beam we use the following equation:

$$F = \frac{2P}{A_{\text{eff}} f_{\text{osc}}} \tag{2.3}$$

where P is the power in mW as measured with the power meter, $A_{\text{eff}} \approx 10^{-2}\,\text{cm}^2$ is the effective beam area as approximated from beam profile measurements, and $f_{\text{eff}} = f_{\text{osc}}/2$ is the effective repetition rate of the laser, which is half that of the oscillator, $f_{\text{osc}} = 10\,\text{kHz}$, after chopping (see fig. 2.1). Hereafter we designate the first pump pulse as the *heating pump* and the second one as the *probing pump*. In the present case two sets of pump powers have been contemplated. In the first set, the heating pump is tuned to a fixed transmission $T_1 = 20$, i.e. fluence $F_1 = 0.66\,\text{mJ}\,\text{cm}^{-2}$, and measurements

are taken at three different probing pump transmissions T_2 of 10, 20 and 30, i.e. $F_2 = 0.3, 0.6, 0.9\,\mathrm{mJ\,cm^{-2}}$. In the second set higher powers are used, with $T_1 = 60$, i.e. fluence $F_1 = 3.5\,\mathrm{mJ\,cm^{-2}}$, for the heating pump, and 10, 20 and 30, i.e. $F_2 = 0.3, 0.6, 0.9\,\mathrm{mJ\,cm^{-2}}$. The pulse length of the probe and the pumps were 20 fs and 18 fs respectively, as measured by the autocorrelator with a Gaussian fit. These values varied no more than 2 fs during an overnight measurement. For each measurement with a set $(F_1, F_2, \Delta t_{\mathrm{pump}})$ (with $\Delta t_{\mathrm{pump})}$ the pump-pump delay), several scans were taken and averaged. This was down in order to avoid artifacts from drifts and to improve the signal-to-noise ratio.

2.5.2 Results and discussion

Fig. 2.6 displays the demagnetization curves obtained by probing the Kerr rotation during the probing pump at a transmission value T_2 and after the heating pump at transmission T_1 has been absorbed. The pump-pump delay times, hereafter Δt_{pump}, range from 0.5 ps to 10 ps, as shown in the common legend. A delay time of -5.0 ps, represented by the black curve in fig. 2.6, has also been chosen as an equivalent to $\Delta t_{\mathrm{pump}} \to \infty$ for reference purposes. The solid lines with the same color as the experimental values are the result of fitting the latter with the double exponential function from eq. 1.7. The time coordinate has been shifted with the zero time t_0 obtained from the corresponding fit, which is located a bit later than the start of the demagnetization. Also the zero of the Kerr signal for each pulse, i. e. the Kerr signal value before the probing pulse, has been pulled to the same value for better comparison of the data.

The effect on the amplitudes

A first point can already be highlighted by observing the shapes of the curves for each heating pulse fluence (i.e. each column in fig. 2.6). Clearly, both the demagnetization amplitude and the characteristic time τ substantially differ. For $T_1 = 20$ ($F_1 = 0.66\,\mathrm{mJ\,cm^{-2}}$) the maximum demagnetization is approximately (5 ± 3) %, as computed by eq. 2.1 at the time of the lowest Kerr signal, and (20 ± 3) % for $T_1 = 60$ ($F_1 = 2.54\,\mathrm{mJ\,cm^{-2}}$). These values are in reasonable agreement with previous experiments [26, 42]. Note however that each of these larger sets was measured in a different run, between which realignment of the pump-pump and pump-probe overlap was performed. Note also that the fluences contemplated here are nominal and do not represent the absorbed power. It is also evident that after the strongest heating pump, the amplitude variations are higher and the demagnetization occurs at a slower rate. This effect can be better appreciated in the upper part of fig. 2.9, where a scatter plot of τ versus the demagnetization amplitude is depicted for each curve of fig. 2.6.

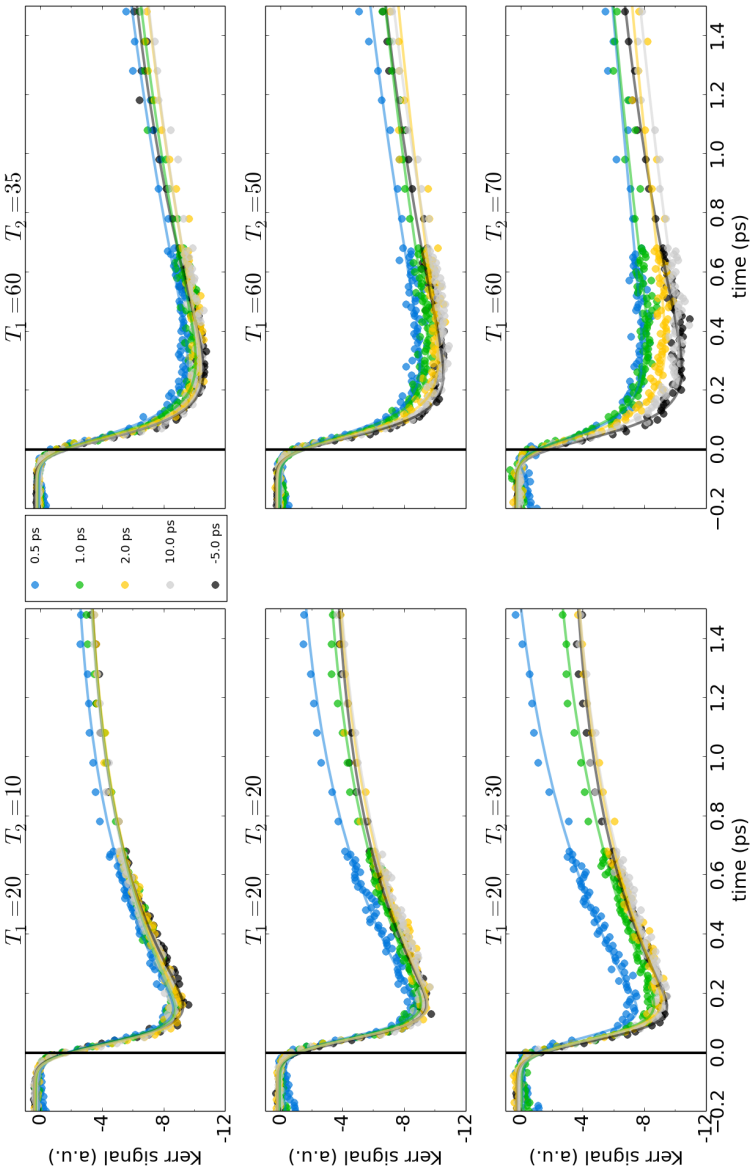

Figure 2.6: Experimental demagnetization curves (points) after the probing pump for different pump-pump delays as stated in the color legend. A negative time delay implies that the heating pump pulse occurs after the probing pulse, which renders it as a reference. Different fluences of the heating and probe pumps are labeled here with their matching (approximate) transmission values T_1 and T_2 for simplicity (see text for the correspondence to fluence). Fits (solid lines) have been added as help for the eye. The zero vertical line marks the t_0 time as obtained from the fit in 1.7.

The most notable feature in fig. 2.6 is nonetheless the difference in the demagnetization amplitudes for different pump-pump delays. On one hand, long delays show curves that virtually overlap with the reference (e.g. the grey and yellow curves at $\Delta t_{\text{pump}} = 10\,\text{ps}$ and $\Delta t_{\text{pump}} = 2\,\text{ps}$). On the other, shorter pump-pump delays show smaller demagnetization amplitudes. This difference in amplitudes becomes more pronounced for higher fluences of the probing pump F_2. Fig. 2.11 further reveals the change of the amplitudes with the pump-pump delay. The values have been normalized to their respective references for comparison. In a roughly exponential manner, the amplitudes stabilize after the 2 ps timescale. This is a surprising behavior, since one would expect shorter delays to result in larger amplitudes if the magnetic response was linear with the deposited energy. This could indicate that the state of the non-equilibrium system has a strong influence in the magnetization dynamics, since the introduction of a second excitation would not lead to a linear response of the system at short timescales.

The effect on the decay times

The first plot in fig. 2.10 also reports the characteristic demagnetization times as a function of the pump-pump delay Δt_{pump} for each set of fluences. While the fluence of the heating pump produces more than a twofold increase of the demagnetization time (from around 30 fs–40 fs to 70 fs–90 fs), the effect of the probing pump fluence is smaller, with a difference of nearly 10 fs and 20 fs in each case. Also, shorter time delays see a slight decrease in τ of a maximum of 10 fs for the highest probing fluences. Since deviations in the fitting procedure are on the order of $\pm 5\,\text{fs}$, the dependence of τ on Δt_{pump} is thus not unambiguously observable at these fluences.

The slowing down of the angular momentum quenching with increasing fluence is a well documented effect in ferromagnets like Ni, Fe and Co [9, 30, 42, 52, 149, 223]. The magnetization recovery time, herein characterized by ρ in eq. 1.7, is known to follow a similar trend [9, 68]. The reason for this behavior lies in the core of the interaction between the electron, the spin and the lattice system in the first few hundreds of femtoseconds. Some experiments [30, 42] have found a delay between the ultrafast decay of the reflectivity, which measures the electronic response, and that of the Kerr rotation (or ellipticity), which tracks the magnetization, originating two thermalization times, τ_e for the faster electron system and τ_s for the slower spin system. Bigot *et. al.* showed that at lower fluences τ_e and τ_s are similar but diverge at higher fluences, where τ_s becomes greater [30]. Koopmans [149] extended this concept to rare-earth ferromagnets that exhibit magnetization decays on the order of several picoseconds such as gadolinium, and predicted that nickel could undergo a phase transition in this way at temperatures close to T_C. Support for the last claim has been brought by Roth and co-workers in his studies of Ni films at temperatures up to 480 K [223]. The

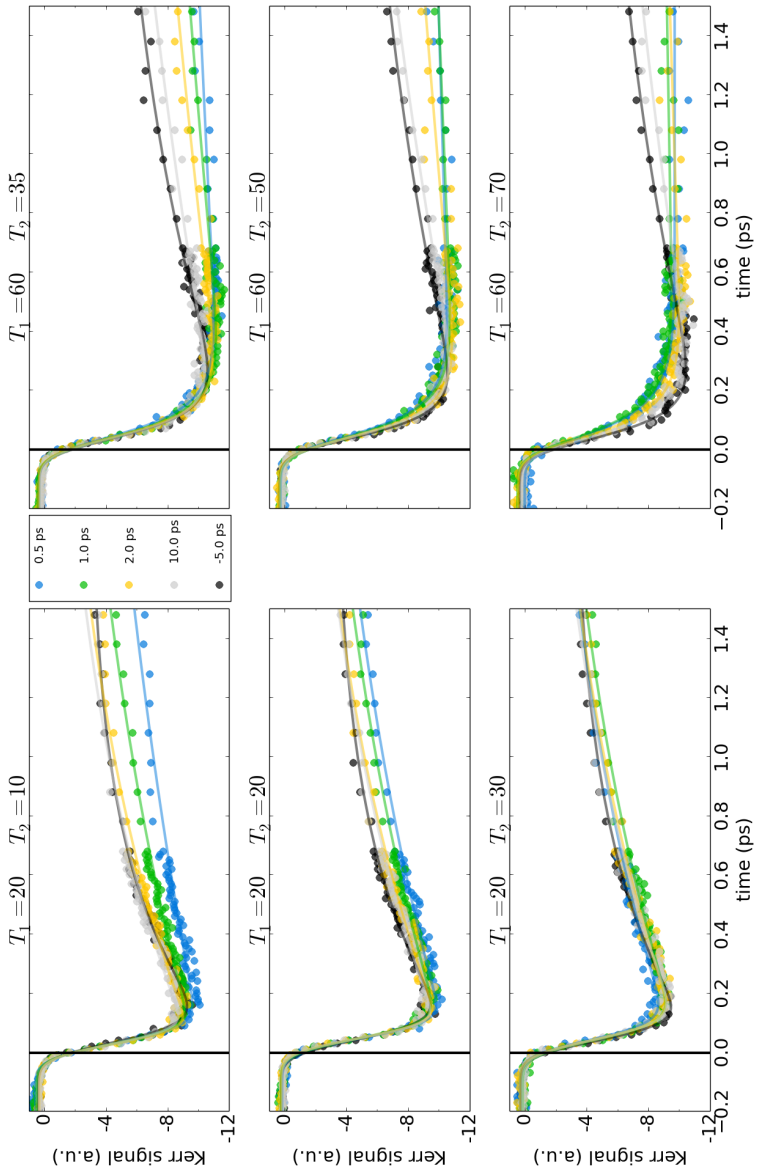

Figure 2.7: Demagnetization curves from fig. 2.6 with baseline correction. A fit from the reference curves at ($T_1 = 20, T_2 = 20$) and ($T_1 = 60, T_2 = 50$) have been used to determine the remagnetization slopes at ranges delayed by Δt_{pump} and subtracted from the actual curves.

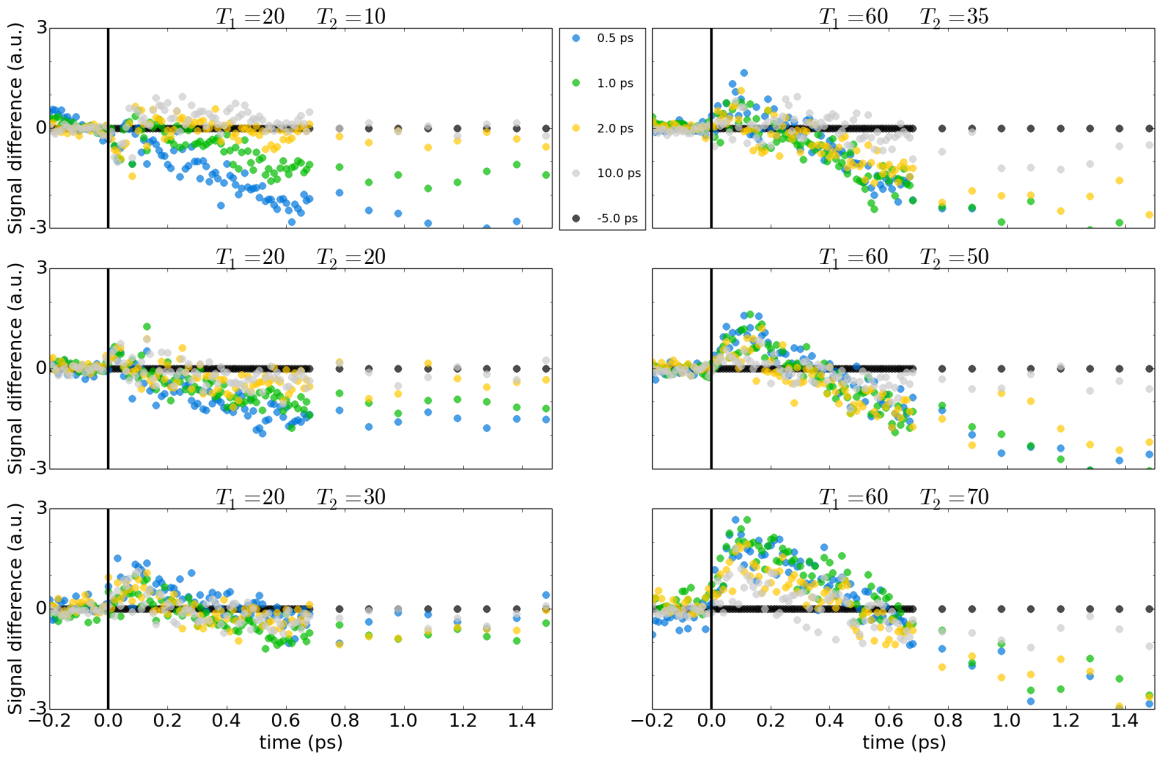

Figure 2.8: Deviations of the curves in fig. 2.7 from their respective reference as a measure of the nonlinearities affecting the probing pulse demagnetization dynamics.

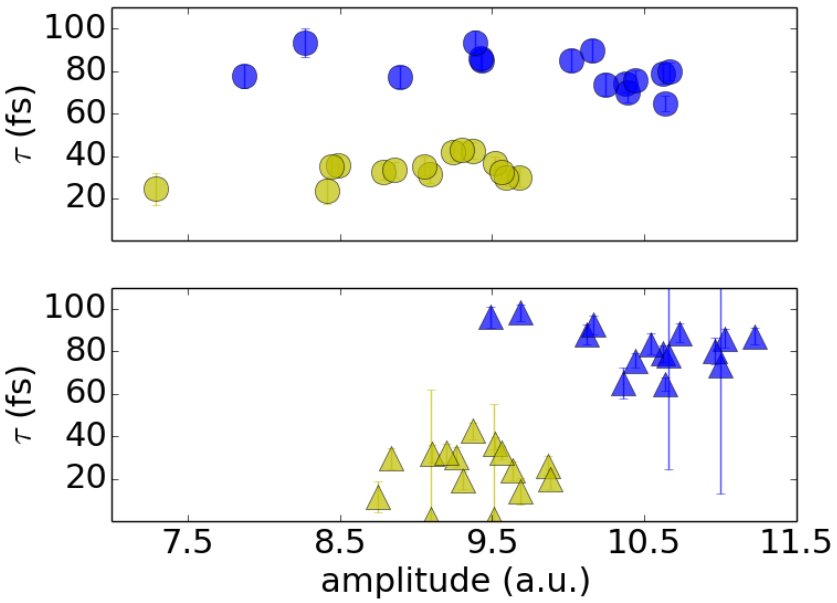

Figure 2.9: Scatter plot of the demagnetization characteristic times τ obtained from the fits in eq. 1.7 versus the amplitudes of the Kerr signal. The upper figure with circles refers to experimental data from fig. 2.6 and the lower one, with triangles, to the corrected, baseline-subtracted version from fig. 2.7. Blue marks correspond to the heating pump fluence $F_1 = 2.15\,\mathrm{mJ\,cm^{-2}}$ while yellow marks denote $F_1 = 0.66\,\mathrm{mJ\,cm^{-2}}$. Error bars in the vertical axis correspond to the errors obtained from the fitting process.

effect can also be observed straightforwardly in fig. 2.6 for the heating pump with the highest fluence. The reference curve ($\Delta t_{\mathrm{pump}} = -0.5\,\mathrm{ps}$) presents a faster remagnetization than the preheated curves. This trend difference is still small due to the generally low fluences used in the experiment, and after a few picoseconds all curves follow the same recovery[8]; but it qualitatively proves the influence of the heating pump in the demagnetization undertaken by the probing pump.

Analysis of the linearity

In order to properly analyze the linearity of the system it is important to recall that the curves in fig. 2.6 differ from static high temperature measurements in that the demagnetization process does not start from a thermal equilibrium. Hence, to isolate the effect of the probing pump, the dynamic effect of the heating pump first needs to be subtracted. Conceptually, the

[8]This is not shown in 2.9, but has been properly addressed in sec. 2.4

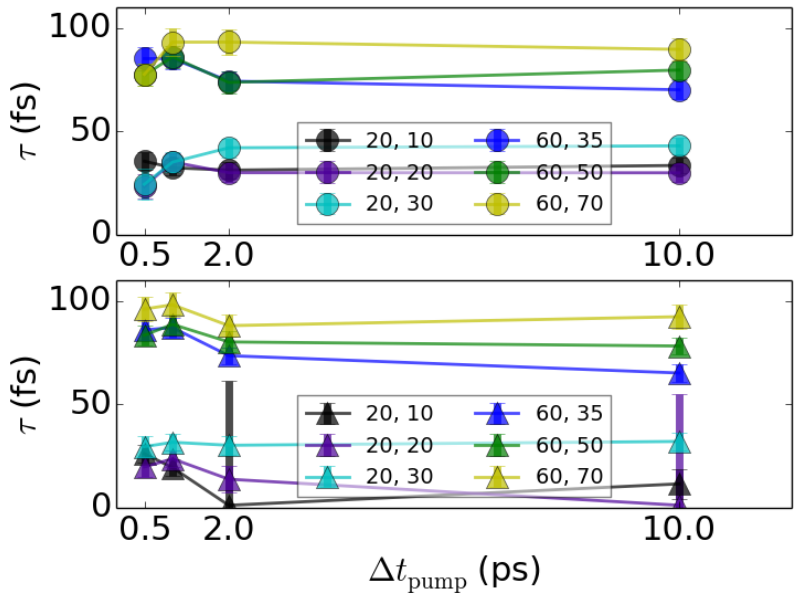

Figure 2.10: Demagnetization characteristic times τ obtained from the fits in eq. 1.7 versus the pump-pump delay, for each fluence set (T_1, T_2), as indicated in the legends. The upper figure with circles refers to experimental data from fig. 2.6 and the lower one to the corrected, baseline-subtracted version from fig. 2.7. The joining lines are meant as a guide for the eye.

linearity of the system to the excitation responses can be addressed as follows. Let $p_1(t)$ and $p_2(t)$ be two different excitation sources. If the system behaves linearly at all times, then

$$M\{(p_1 + p_2)(t)\} = M\{p_1(t)\} + M\{p_2(t)\} \tag{2.4}$$

where $M\{p_i(t)\}$ is the magnetic response to the corresponding excitation source. Therefore, in order to obtain a measure of the (non)linearity of the system the quantity

$$\Delta M_{\text{nonlin}} = M\{(p_1 + p_2)(t)\} - M\{p_1(t)\} - M\{p_2(t)\} \tag{2.5}$$

shall be calculated. The values of $M\{(p_1 + p_2)(t)\}$ are obviously the ones shown in fig. 2.6, and $M\{p_2(t)\}$ corresponds to the reference curves at $\Delta t_{\text{pump}} = -5\,\text{ps}$. $M\{p_1(t)\}$, the effect of the heating pulse, has been retrieved by fitting the reference curve whose fluence is closest to that of the heating pulse and then extrapolating the values at the appropriate pump-pump delays. The first subtraction in eq. 2.4, i.e. $M\{(p_1 + p_2)(t)\} - M\{p_1(t)\}$, which detaches the effect of the heating pump, can be observed

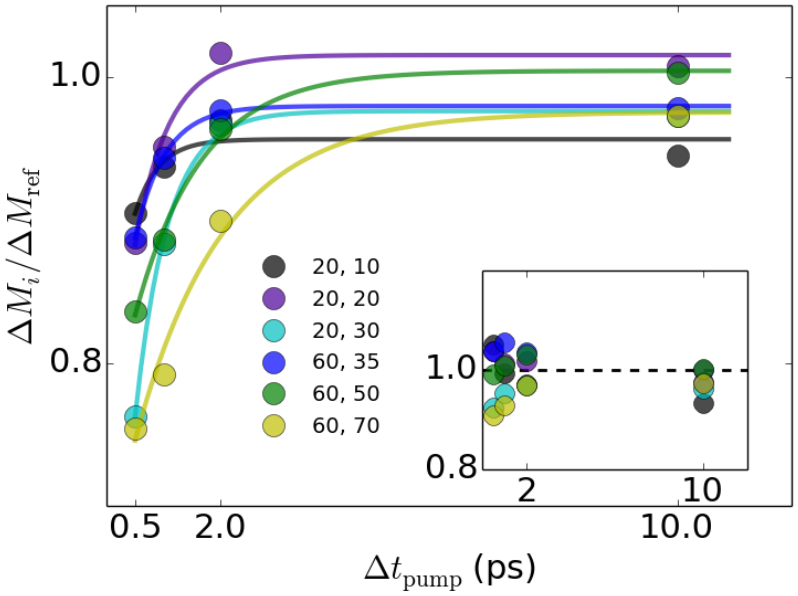

Figure 2.11: Demagnetization amplitudes obtained from the fits in eq 1.7 versus the pump-pump delay, for each fluence set (T_1, T_2), as indicated in the legend. The amplitudes have been normalized to their respective references. The main figure refers to experimental data from fig. 2.6 and the inset displays the corrected, baseline-subtracted version from fig. 2.7. The lines are meant as a guide for the eye.

in fig. 2.7. The results for $\Delta M_{\mathrm{nonlin}}$ are depicted in fig. 2.8. If all stages of the demagnetization process were linear, then one should expect $\Delta M_{\mathrm{nonlin}} = 0$ for all curves or, equivalently, the curves for each probing pump fluence in fig. 2.6 to scale down to their respecting references. Notwithstanding, the results presented in fig. 2.7 reveal a distinct comportment. The amplitude differences have diminished to a greater extent, as can be also appreciated in the inset of fig. 2.11, but inhibition of the demagnetization for short delays is still visible at higher fluences. In addition, the slopes of the remagnetization tails have considerably decreased, exposing an apparent enhancement of the aforementioned temperature effect. This enhancement is highest at the lower heating fluence and for the lowest probing fluence, which seems counter-intuitive.

Consider now the behavior of the curves for different pump delays. In one end, we have the curves at $\Delta t_{\mathrm{pump}} = 10\,\mathrm{ps}$. Clearly, at this timescales both the electron and the phonon systems have reached a common temperature [270] and are cooling down together, as section 2.4 has demonstrated. The probing pump pulse is thus acting on a system in equilibrium at a tempera-

ture $T(10\,\mathrm{ps}) > T_{\mathrm{room}}$. Let us estimate this temperature from the data. After 10 ps the magnetization of the reference curves is[9] a maximum of 1/4, for the highest fluence, and a minimum of 1/5, for the lowest, of the maximum demagnetization $\Delta M_{\mathrm{max}}/M_0$. This means that, at the most, there is still a 5 % demagnetization from the room temperature value. From data of the classical $M(T/T_{\mathrm{C}})$ figure for nickel [232], and taking $T_{\mathrm{room}} = 295\,\mathrm{K}$ and $T_{\mathrm{C}} = 627\,\mathrm{K}$, an equilibrium temperature $T(10\,\mathrm{ps}) = 374\,\mathrm{K}$ is obtained in the worst case scenario. This value is definitely far from the Curie temperature, which explains why the curve at 10 ps only differs from the reference in a slightly slower recovery at the highest fluences. It should be pointed out that recent temperature-resolved studies from Roth *et.al.* [223] indeed report an increase in the demagnetization amplitude at higher temperatures. However, the fluences used in this experiments were more than three times larger than the highest fluence set used here[10]. In the present case, the transition between Type I and Type II demagnetization behavior described by Koopmans [149] should occur at temperatures closer to T_C (cf. [223, fig. 4]). Hence, it seems reasonable to expect $\Delta t_{\mathrm{pump}} = 10\,\mathrm{ps}$ demagnetization curves with the same amplitudes as their respective references.

On the other hand, this behavior breaks as Δt_{pump} becomes smaller and the amplitudes unexpectedly decrease. At the shortest delay of 0.5 ps, for instance, the electron bath has thermalized through electron-electron interactions into a definite temperature, but the system is not yet in equilibrium with the lattice. The previous arguments involving the equilibrium $M(T/T_{\mathrm{C}})$ figure are thus not valid anymore and the interaction with the second excitation proceeds in a nonlinear manner.

With such results in hand, let us now examine the same aspects discussed here with the predictions of the M3TM.

2.5.3 Comparison with the M3TM model

A simulation based on the modified version of the 3TM model (M3TM) introduced by Koopmans [147, 149] has been performed to represent the double pulse experiment using the same sets of fluences and the same pump-pump delays.

[9] Not shown in the figures. Cf. section 2.4.

[10] The highest fluence for the probing pump, $F_2 = 2.15\,\mathrm{mJ\,cm^{-2}}$, reduces to nearly $1\,\mathrm{mJ\,cm^{-2}}$ when the absorption factor for Ni of $\sim 50\,\%$ is taken into account.

C_e [J kg^{-1} K^{-1}]	445$*$
C_p [10^6 J kg^{-1} K^{-1}]	2.33$*$
κ [J s^{-1} m^{-1} K^{-1}]	90.7$*$
g_{ep} [10^{18} J s^{-1} m^{-3} K^{-1}]	4.05$*$
τ_p [ps]	0.02
d [nm]	20
δ_{Ni} [nm]	14.58†
r_{Ni}	0.589†
t_{Ni}	0.025†
T_C [K]	627$*$
R [ps^{-1}]	17.2$*$

Table 2.1: Parameters for the simulation. $*$ values taken from [149] to maintain coherence with the original calculations from Koopmans[11]. † values taken from [204] with data by Rakic, 1998. τ_p is taken from the autocorrelation trace.

Definition and parameters

The differential equations to be solved [149] are reproduced here for convenience:

$$C_e(T_e)\frac{dT_e}{dt} = \nabla_z(\kappa\nabla_z T_e) - g_{ep}(T_e - T_p) + p(t) \tag{2.6}$$

$$C_p\frac{dT_p}{dt} = g_{ep}(T_e - T_p) \tag{2.7}$$

$$\frac{dm}{dt} = Rm\frac{T_p}{T_C}\left(1 - m\coth\left(\frac{mT_C}{T_e}\right)\right) \tag{2.8}$$

Here T_e and T_p denote the electron and the phonon temperatures. C_e and C_p stand for the respective heat capacities, κ is the thermal conductivity of nickel and g_{ep} the electron-phonon coupling constant. Additionally, $p(t)$ represents the energy source, which in this case is represented by the sum of the heating and the probing pump pulses, i.e. $p(t) = p_1(t + \Delta t_{\mathrm{pump}}) + p_2(t)$. Both pulses are in fact identical, gaussian-shaped excitations of the form

$$p_i(t) = p_0 e^{-4\ln 2\left(\frac{t}{\tau_p}\right)^2} \tag{2.9}$$

where τ_p is the FWHM length of the pulse and p_0 is the peak power density, which can be written as

$$p_0 = \frac{2\sqrt{\ln 2}}{\sqrt{\pi\tau_p\delta_{\mathrm{Ni}}(1 - e^{-d/\delta_{\mathrm{Ni}}})}}a_{\mathrm{Ni}}F \tag{2.10}$$

with d the film thickness and δ_{Ni} the optical absorption length of nickel. F is the incident laser fluence and the absorption coefficient is given by $a_{\mathrm{Ni}} = 1 - r_{\mathrm{Ni}} - t_{\mathrm{Ni}}$, with r_{Ni} and t_{Ni} the reflectance and transmittance of Ni, respectively[12].

It has to be emphasized that the original treatment by Koopmans makes use of both the instantaneous thermalization and the delta-pulse assumptions elaborated on in sec. 2.2. The former is implicit in the M3TM, whereas the latter has a minor influence for pulses much shorter than the thermalization time. For a double pulse experiment though, the finite length of the probing pump has been taken into consideration. Eq. 2.8 states the rate of change with time of the magnetization m, which depends on the sub-system temperatures, the Curie temperature T_C and a constant R. The latter depends at the same time on microscopic parameters, among which the spin-flip scattering probability a_{sf} from the Elliot-Yafet theory is to be highlighted[13].

Table 2.1 summarizes the parameter values used for the simulation. For the most part, the original values employed by Koopmans have been preserved.

The effect on the amplitudes

The results are depicted in fig. 2.12. Noteworthy, the quenching amplitudes resulting from the simulation are in qualitative agreement with the experimental values ($\approx 2\,\% - 6\,\%$ and $\approx 8\,\% - 22\,\%$). However, several differences can be also immediately found. The amplitudes for curves with $\Delta t_{\mathrm{pump}} > 0.5\,\mathrm{ps}$ are visibly larger than the reference for every set of fluences, that is, there is an enhancement of the demagnetization. The exception is for $\Delta t_{\mathrm{pump}} = 0.5\,\mathrm{ps}$ at the lowest fluence set, where the amplitude is substantially smaller. The remagnetization occurs particularly faster for this delay as well. Also notice that the amplitude of the curves at $\Delta t_{\mathrm{pump}} = 10\,\mathrm{ps}$ lies between that of $\Delta t_{\mathrm{pump}} = 0.5\,\mathrm{ps}$ and the rest. This effect can be better observed in the upper plot of fig. 2.16 that depicts the amplitudes against Δt_{pump}. A maximum around $\Delta t_{\mathrm{pump}} = 2\,\mathrm{ps}$ is observed, which suggests nonlinearities. In this figure, the higher demagnetization enhancement at higher fluences is clearly exposed too. While a similar change at short delays can be seen with the experimental data from fig. 2.11, in that case the amplitudes remain lower than the reference, never reaching a maximum, and higher fluences actually show a reduction of their amplitudes.

[12] Although the sample is capped by a 3 nm titanium layer we approximate $r_{\mathrm{Ni}} \approx r_{\mathrm{Ti}}$.

[13] Refer to [59, p. 63] for further details on the derivation of a_{sf} and the R parameter.

[13] Note, however, that some values such as g_{ep} have been refined [23]. C_e has been left as a constant too, which is a good approximation in the low fluence regime.

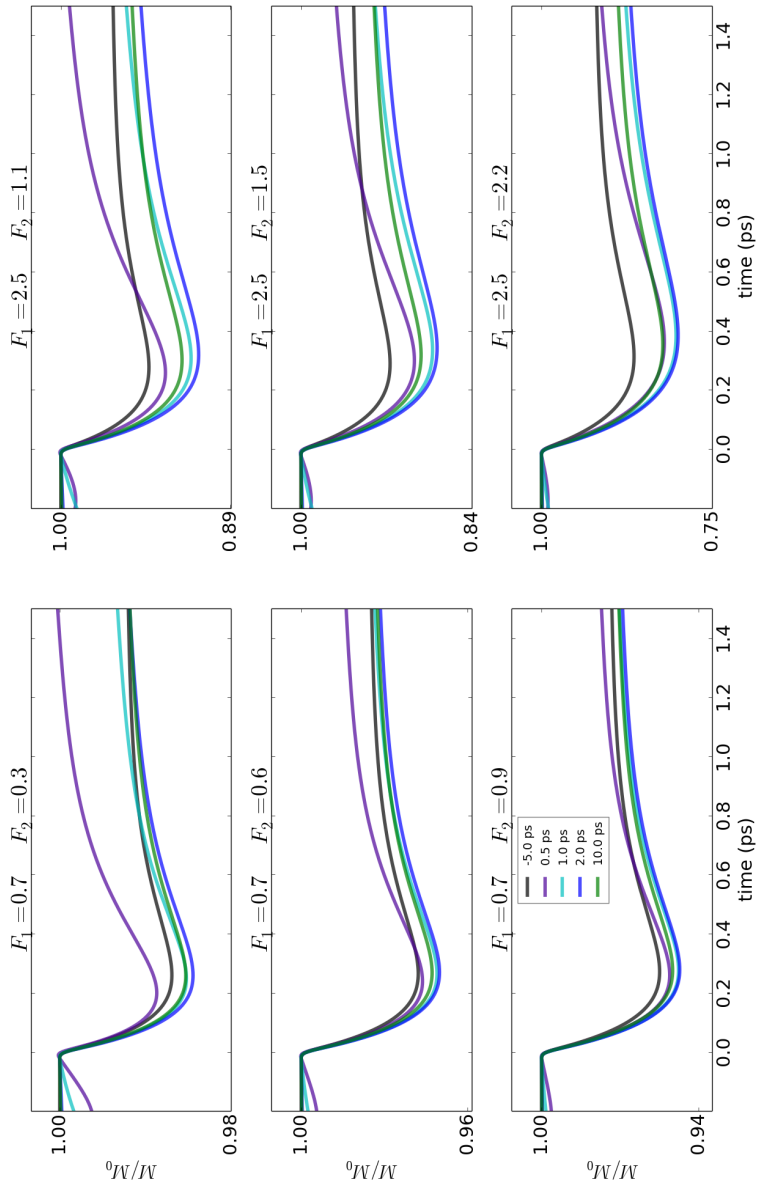

Figure 2.12: Simulations for the same set of fluences F_1 and F_2 (in mJ cm^{-2}) as in fig. 2.6. The common legend in the bottom left identifies the pump-pump delay times associated with each curve. Note that the amplitude ranges have been changed to accommodate the visibility of the curves.

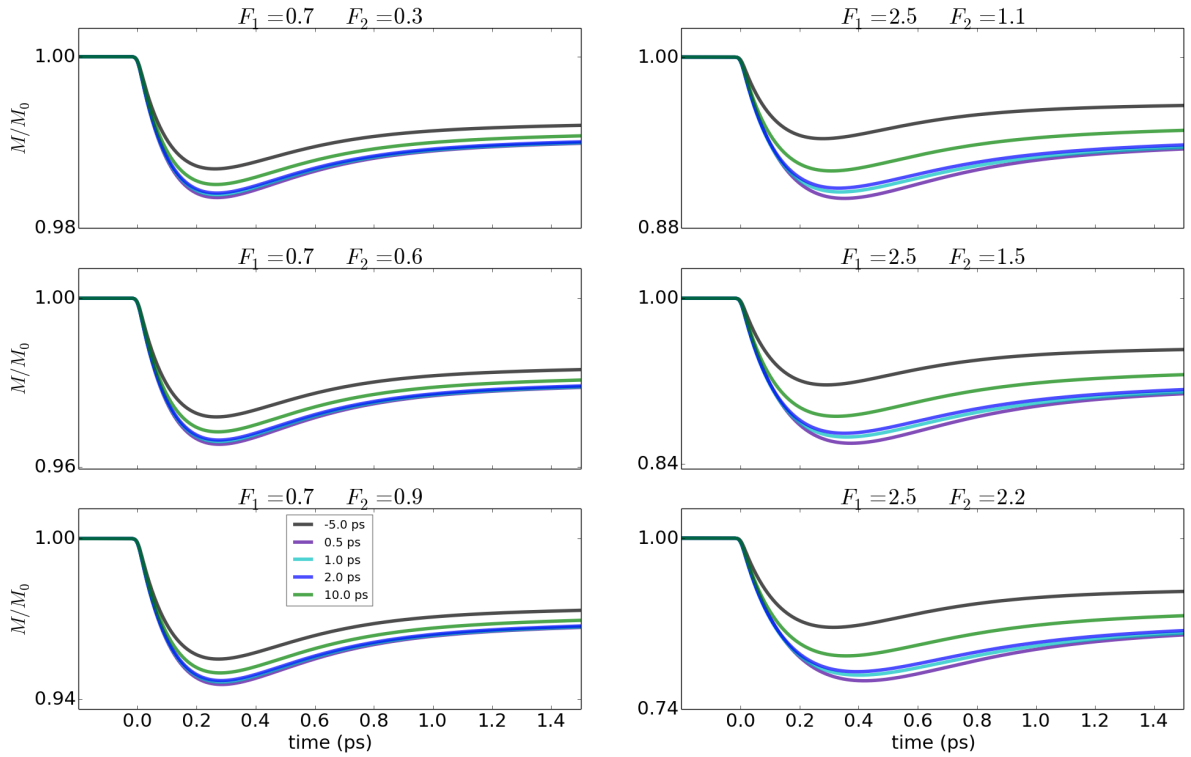

Figure 2.13: The corrected version of fig. 2.7, with the baseline trend from the heating pulse subtracted from each curve. To compare with fig. 2.13.

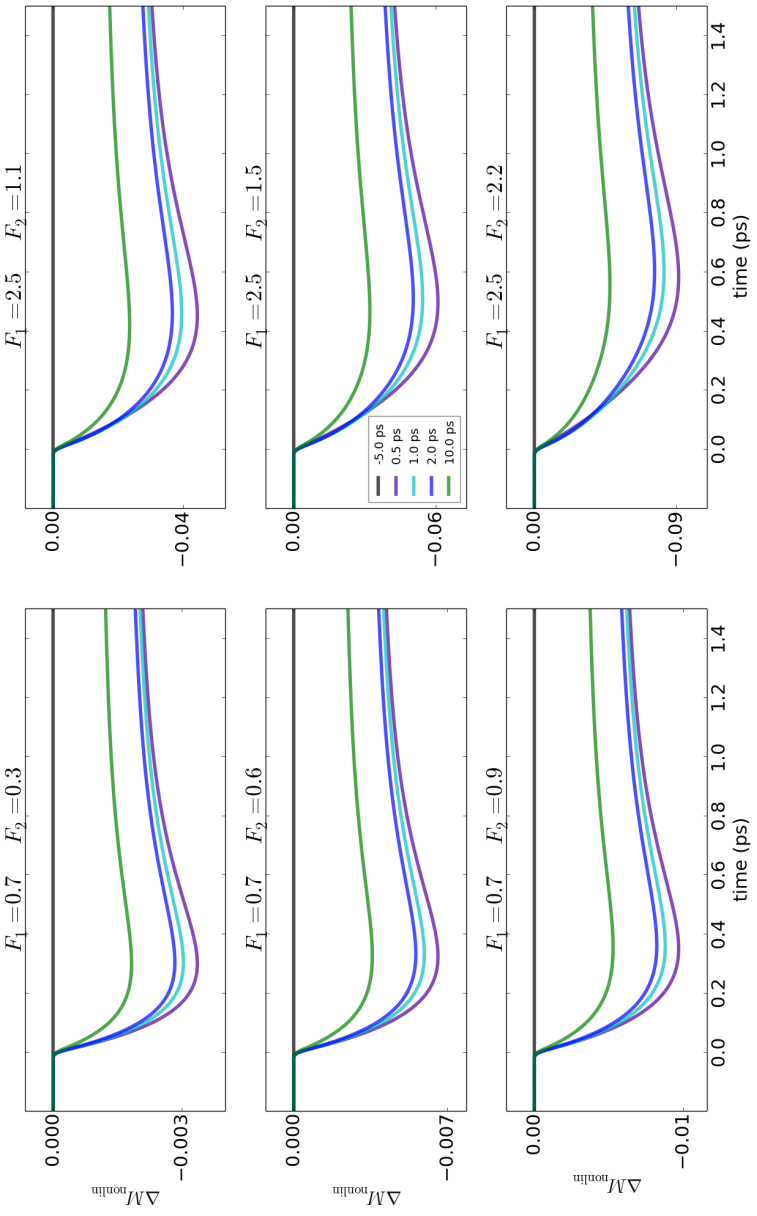

Figure 2.14: Deviations of the simulated curves in fig. 2.12 from their respective references as a measure of the nonlinearities affecting the probing pulse demagnetization dynamics.

The effect on the decay times

The decay times, herein calculated as the time of maximum demagnetization $t(\Delta M_{\max})$, are related to the quenching amplitudes as fig. 2.15 exhibits, that is, larger amplitudes correspond to slower demagnetization curves. This is in line with the measurements (fig. 2.10). However, in the simulation the transition from the lower to the higher heating pump fluences is smoother, whereas in the experiments mainly two regimes are present, one for each heating pump fluence. Further information can be appreciated in the upper plot of fig. 2.16, which presents the changes in $t(\Delta M_{\max})$ with the pump-pump delay. The short and small decrease of the time occurring at low pump delays is similarly reproduced in the experiments (fig. 2.10), although, again, the increase in time for higher fluences is less pronounced.

Analysis of the linearity

The same subtraction of the heating pump effect (eq. 2.4) can be applied to the simulation curves, which results in the plots in fig. 2.13. The curves appear now rescaled, with larger amplitudes at shorter pump delays in every case, thereby implying an inherent demagnetization enhancement not observable in the experimental data. The lower plot in fig. 2.16 depicts the amplitudes against the pump delay, in the same fashion as the inset of fig. 2.11. It reveals an almost linear variation of this enhancement (except for the shortest delays), but in this case all amplitudes are indeed larger than that of reference.

As for the decay times, fig. 2.10 clearly shows that the corrected curves have a slow variation across the delay range, except for the shortest times and the highest fluences, which slow down the decay. This is also the case for the data shown in the lower part of fig. 2.10. As discussed in the previous section, the increase of the demagnetization time with fluence is a well-documented effect. In this case, a shorter pump-delay implies a hotter electron gas prior to demagnetization, which is qualitatively equivalent to a higher fluence. However, this effect is weak and only observable for large fluence variations. Therefore, in order to see stronger variations in the decay time, it would be necessary to use higher fluences.

Finally, fig. 2.14 computes eq. 2.4 to find the (non)linearity of the system. It is remarkable that the values of ΔM_{nonlin} are roughly a 10 %-20 % of the maximum demagnetization for each fluence set and remain non-zero even after a few ps. This indicates that a linear response of the system is not to be expected during the first picoseconds after the second excitation. While the experiments also favor this hypotheses, the exposed behavior is opposed with respect to the demagnetization amplitudes. The M3TM model predicts an enhancement of the demagnetization mainly due to the effect of the heating pump, with the probing pump having a smaller influence. In the ex-

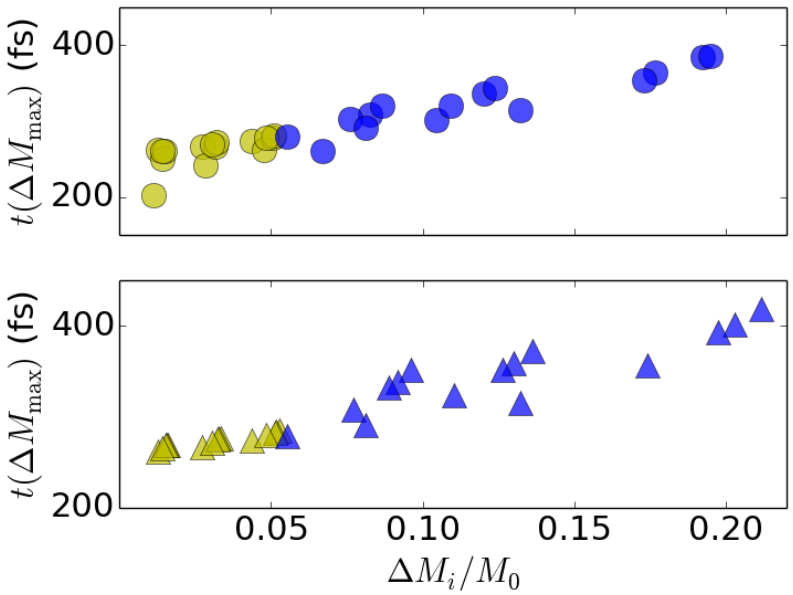

Figure 2.15: Scatter plot of the times at maximum demagnetization obtained from the simulation (eq. 2.6 versus the demagnetization amplitudes. The upper figure with circles refers to simulation data from fig. 2.12 and the lower one, with triangles, to the corrected, baseline-subtracted version from fig. 2.13. Blue marks correspond to the heating pump fluence $F_1 = 2.15\,\mathrm{mJ\,cm^{-2}}$ while yellow marks denote $F_1 = 0.66\,\mathrm{mJ\,cm^{-2}}$

periments this enhancement is not observable, but rather a slight inhibition of the demagnetization for higher fluences is measured, accompanied by an increase in the recovery time. Since the lattice and the electron sub-systems are not in thermal equilibrium at the short delays examined here, a nonlinear response of the system to the second excitation could be the cause of such discrepancies.

2.5.4 Conclusions

In this study a double pulse Kerr experiment has been performed, wherein a heating pump pre-heats a nickel thin film followed by a second excitation from a standard pump-probe experiment. Measurements have been taken for different excitation fluences, as well as for different pump-pump delays. The linearity of the system response has been computed by subtracting the dynamic baseline extrapolated from the heating excitation. For long delays and for low fluences, the results show a linear response during the demagnetization but an increase in the recovery time. For short delays and for high

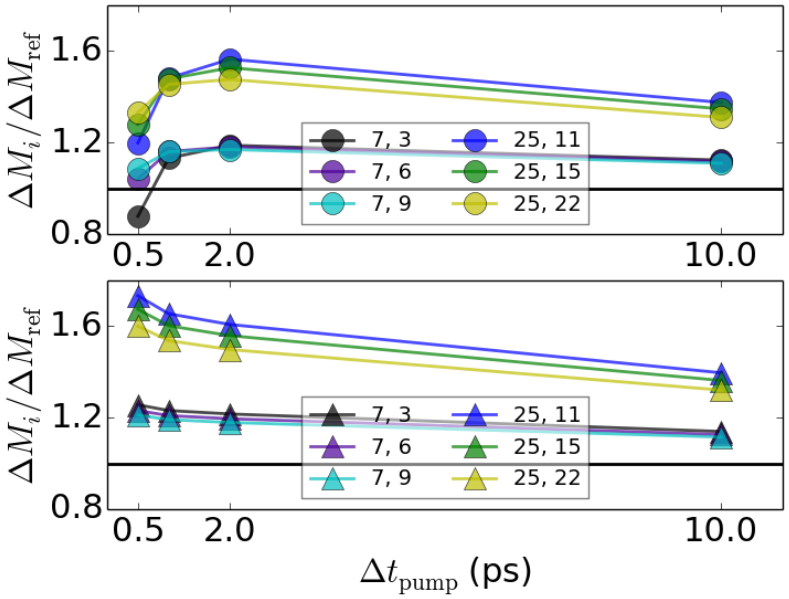

Figure 2.16: Demagnetization amplitudes obtained from the simulation (eq. 2.6) versus pump-pump delay. Each fluence set (F_1, F_2) indicated in the legend denotes the fluence in $\mathrm{J\,m^{-2}}$. The amplitudes have been normalized to their respective references. The upper figure with circles refers to simulation data from fig. 2.12 and the lower displays the corrected, baseline-subtracted version from fig. 2.13. The lines are meant as a guide for the eye.

fluences, a relative decrease in the demagnetization amplitude, and therefore a nonlinear response, is observed. Simulations for the M3TM based on Elliot-Yafet spin-flip scattering predict instead an enhancement of the demagnetization, emphasized at shorter pump delays and higher fluences. In both cases an increase in the demagnetization time is observed at shorter delays and higher fluences as reported in other studies. The cause of the former discrepancy remains unclear and requires further studies on the nonlinear response of this system when the lattice and the electron sea are still in a non-equilibrium state with each other.

2.6 The effect of transport in the demagnetization process

The previous study has addressed the effect that a heating excitation produces in the magnetic response of a demagnetization process, specially at timescales shorter than the electron-phonon equilibration time of a few pi-

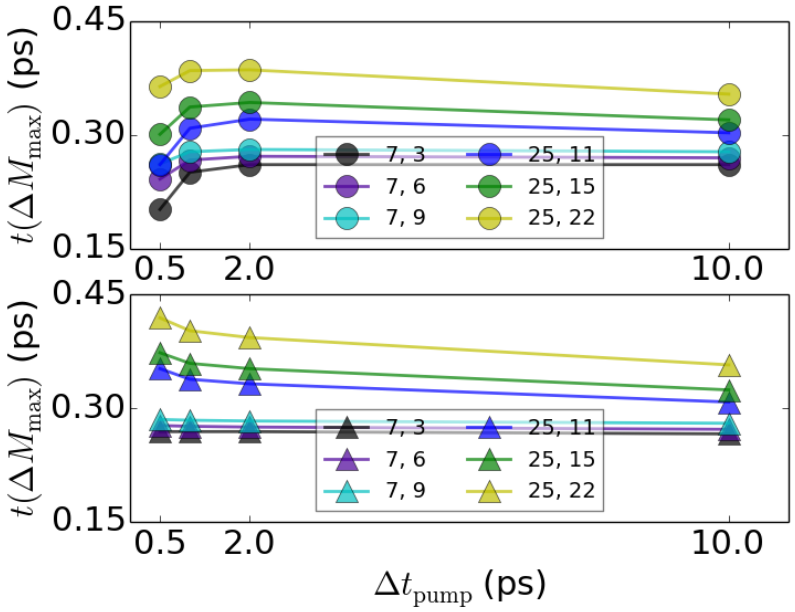

Figure 2.17: Demagnetization characteristic times τ obtained from the simulation (eq. 2.6) versus the pump-pump delay. Each fluence set (F_1, F_2) indicated in the legend denotes the fluence in J m^{-2}. The upper figure with circles refers to simulation data from fig. 2.12 and the lower one to the corrected, baseline-subtracted version from fig. 2.13. The joining lines are meant as a guide for the eye.

coseconds. In order to minimize diffusion, the sample thickness was maintained to a value close to the optical absorption length. In this section[14] attention is turned to the diffusive process that is present in less constrained systems. The observation of diffusive mechanisms in ultrafast magnetization dynamics has already been elaborated on in section 2.2. While the evidence for spin diffusion has been repeatedly proven in many systems, it remains controversial its influence in the demagnetization of single-layer ferromagnets [229]. In addition, there has been a debate around the contribution of hot electron versus direct excitation of light transmitted through the absorbent layer in transport experiments [73, 136, 265]. Finally, it is not clear whether the electrons involved in the transport phenomena show diffusive or super-diffusive/ballistic properties [19, 20, 70, 72, 178]. In the following investigation, demagnetization induced by hot electron transport is carried out by measuring the magnetic as well as the non-magnetic contrast of a nickel sample as a function of its thickness, in order to isolate the effect

[14] Part of this section has been published in [227].

of electron-mediated, lattice-mediated and optically induced heating on the demagnetization.

2.6.1 The Al/Ni experiment

For the present experiment a 10 nm nickel film grown on top of an aluminum layer of variable thickness d_{Al} has been used as the sample to study the effect of hot electron transport in the demagnetization process. Aluminum, being a non-magnetic material with a high spin diffusion length [18], with a similar refraction index to nickel and electrical characteristics of a good Fermi liquid [23], was chosen as an adequate candidate for the purpose of the study. The layer structure is formed by 3 nm Ti / 10 nm Ni / d_{Al} nm Al / 3 nm Ti, resembling the previous experiment. The aluminum layer thickness has been varied between 0 nm and 60 nm. The pump-probe setup employed has been already described in section 2.3. This time, only one of the pump pulses is used, directed to the back surface of the sample, while the 400 nm laser probe scans the front surface. Again, the angle of incidence is 45° and the applied alternating magnetic field 100 Oe, sufficient to saturate the sample. The balanced photodiodes measure the change of polarization rotation $\Delta\theta_{\uparrow,\downarrow}(t)$ and eq. 2.1 is used to retrieve the magnetization $\Delta M(t)$. In addition, the non-magnetic contribution of the pump-induced polarization rotation can be calculated as

$$\Delta N(t) = \frac{\Delta\theta_{\uparrow}(t) + \Delta\theta_{\downarrow}(t)}{\theta_{\uparrow} + \theta_{\downarrow}} \tag{2.11}$$

This quantity is useful in that it describes the response of the whole electron system to the polarized beam rather than the magnetic component.

2.6.2 Results and discussion

Fig. 2.18 depicts de relative demagnetization $\Delta M(t)/\Delta M_{\mathrm{max}}$ as well as the relative magnetic polarization change $\Delta N(t)/\Delta N_{\mathrm{max}}$ within the first 1.5 ps for the different aluminum thicknesses considered. In order to conveniently compare the magnetic and non-magnetic responses, the back pump fluence was adjusted so as to produce a maximum demagnetization of at least 4 % but no more than 10 %. This range belongs to a linear regime [83], which has been verified *in situ* for the used samples. Table 2.2 lists the values of the back pump fluence F_{pump} and the resulting demagnetization $\Delta M/M_s$ reached for every sample. The figure reveals that the non-magnetic part of the signal $\Delta N(t)/\Delta N_{\mathrm{max}}$ doesn't see its shape modified by d_{Al} before the first 200 fs, whereas the magnetic part $\Delta M(t)/\Delta M_{\mathrm{max}}$ has a faster decay rate for thinner Al layers. In order to determine a characteristic time of the demagnetization, t_{d}, a fit with eq. 1.7 was performed. Then, the time lapse from a 10 % to a 90 % of the maximum amplitude, ΔM_{max}, has been obtained

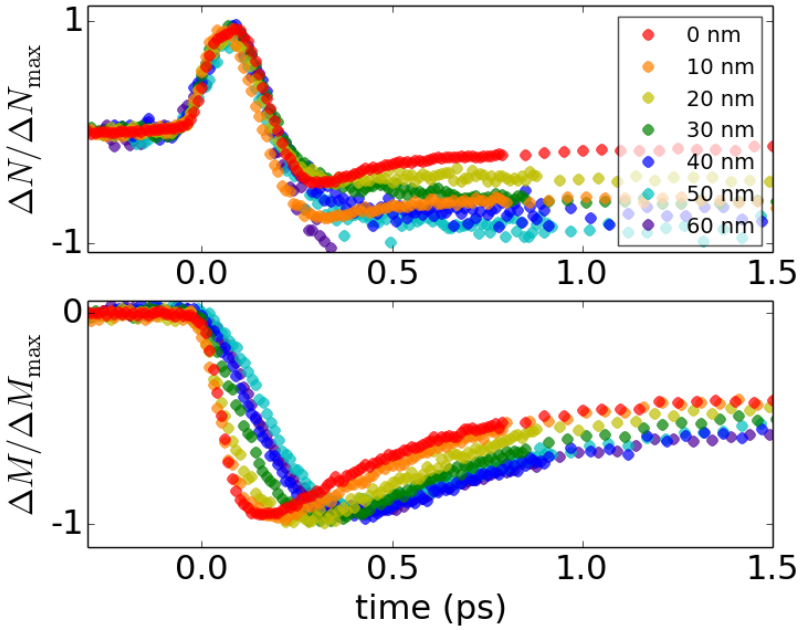

Figure 2.18: Non-magnetic (up) and magnetic (down) Kerr signal during the demagnetization of samples with different Al layer thicknesses, as stated in the legend. The values have been normalized with respect to the amplitude maximum. Reprinted from [227].

from the fit. While the τ parameter from eq. 1.7 is usually a good candidate to represent the decay time, it is not the best choice when a precise measure of the demagnetization time is required, since its value also depends on the recovery parameter ρ. A substantial increase in t_d for thicker Al films can be observed both in fig. 2.18 and in the inset of fig. 2.20. Since the experiment was performed in individual samples, it is necessary to determine the temporal overlap between the pump and the probe for each measurement series. The zero time has been taken from the non-magnetic curves, since their rising edges do not depend on d_{Al}. In particular, t_0 has been chosen such that $\Delta N(t_0)/\Delta N_{max} = 0.5$. Remarkably, the delays reported by Vodungbo *et. al.* [265] are not observed in the present experiment. The magnetic signal at longer times, up to 80 ps, is shown in fig. 2.19. In this figure, the transmission of heat by phonons throughout the absorber layer is clearly visible at thicker layers, which have been excited by a more intense pump.

To further investigate the causes of $\Delta M(t)$ and $\Delta N(t)$, the demagnetization amplitudes of both signals are first scaled with the corresponding pump fluence and then compared for each thickness. Fig. 2.20 therefore plots $\Delta M_{max}/F_{pump}$ (red circles) and $\Delta N_{max}/F_{pump}$ (blue triangles) as a function

d_{Al} (nm)	F_{pump} (mJ cm^{-2})	$\Delta M/M_s$ (%)
0	0.21	8.8
10	0.35	5.5
20	1.55	5.2
30	2.97	5.5
40	6.43	5.3
50	8.59	4.9
60	10.77	4.1

Table 2.2: Values of the back pump fluence F_{pump} and the resulting demagnetization $\Delta M/M_s$ for each layer thickness.

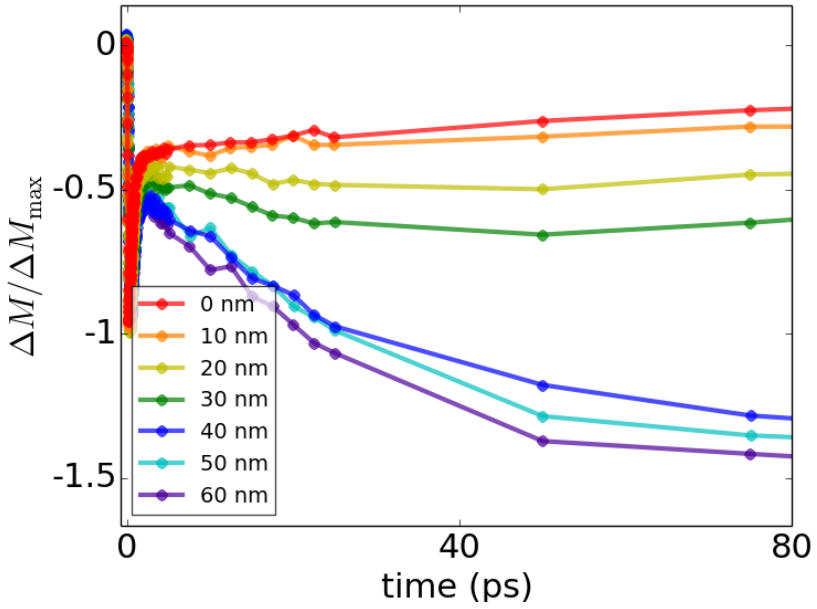

Figure 2.19: Magnetization signal at longer timescales showing the effect of heat from the back pump through the sample. The legend states the Al layer thicknesses. The values have been normalized with respect to the maximum of the initial demagnetization.

of d_{Al}. Note that the vertical axis is in a logarithmic scale, and that all curves have been scaled together for comparison. Noticeably, the curve $\Delta N_{\max}(d_{\mathrm{Al}})$, with a decay length of 10.5 nm, matches the optical transmission curve T_{opt} (green stars) that was measured independently for each sample. This indicates that the non-magnetic signal follows the electronic excitation undertaken by direct interaction with the laser light transmitted through the sample. Indeed, linearly polarized light can temporarily cause birefringence in metals, inducing an all-optical change in the rotation of the polarization in a reflected probe beam. This type of Kerr effect in a reflection geometry is commonly known as the specular optical Kerr effect (SOKE). It was first demonstrated by Saiki and coworkers [226] in 1992 and later studied by other authors [154, 205]. SOKE is known to be caused by non-equilibrium hot electrons. Since these have short lifetimes as detailed in 2.2, the resulting signal changes occur on the 100 fs timescale. The curves in fig. 2.18 are in agreement with studies by Krugylak [154] for nickel and other metals. From the match of $\Delta N_{\max}(d_{\mathrm{Al}})$ with T_{opt} it must be concluded that $\Delta N(t)$ is caused by electrons excited directly by the laser pump fraction transmitted through the sample. This also makes the SOKE signal a good reference to find the temporal overlap t_0 between the probe and the pump.

In contrast, the magnetic signal follows the trend of the SOKE signal only for the samples with $d_{\mathrm{Al}} < 30$ nm, but visibly slows down at larger thicknesses, thereafter reaching a decay length of 23.5 nm. This behavior is attributed to the diffusion of hot electrons from the backside of the sample, which further demagnetizes the nickel layer. In order to test this assumption, a simulation using the 2TM has been performed.

2.6.3 Simulations for transport. Is superdiffusion necessary?

It has been shown that in the low fluence regime the demagnetization amplitudes scales linearly with the fluence both experimentally [9, 42, 83] and theoretically [149]. In 3d ferromagnets, the demagnetization initially follows the heat absorbed by the electron gas as the electron-spin coupling is stronger than in other metals [149]. Since the heat per unit volume stored in an electron gas is $q = C_e(T_e)T_e = \gamma T_e^2$, where γ is the electron heat capacity coefficient, the exchange of heat within the electron gas caused by a temperature rise from T_0 to T_e is $\Delta q = \gamma(T_e^2 - T_0^2)$. That is to say, for small amplitudes, the demagnetization is proportional to the deposited heat in the sample:

$$\Delta M \propto (T_e^2 - T_0^2) \tag{2.12}$$

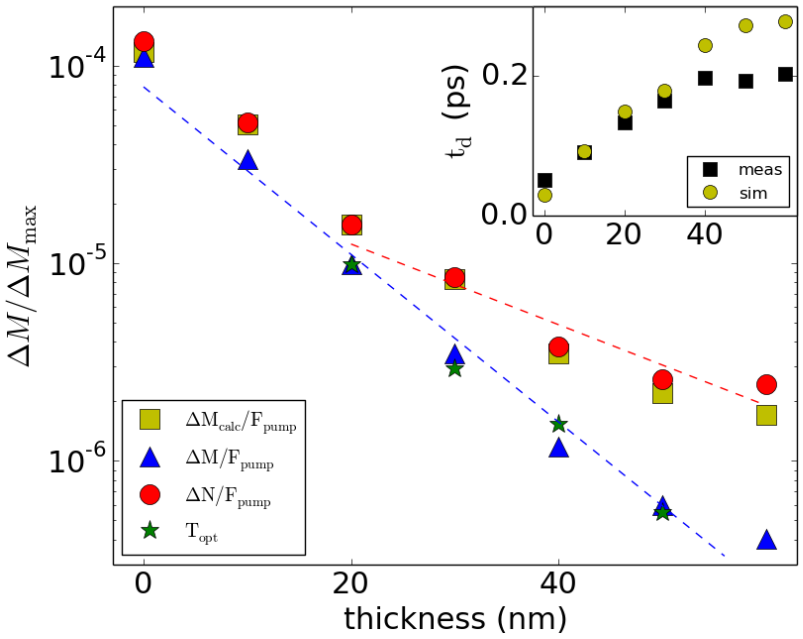

Figure 2.20: Maximum amplitudes of the magnetic (red circles) and non-magnetic (blue triangles) Kerr signals versus d_{Al}, rescaled with the corresponding laser fluence. The non-magnetic curve follows the same trend as the optical transmission (green stars), whereas the magnetic one is closer to the calculated values from simplified transport considerations. The inset shows the 10 % to 90 % decay time from both the measured data and the simulations detailed in the text. Reprinted from [227].

Due to this relation of the demagnetization with the exchanged heat, the dynamics of ΔM can be found by solving the heat diffusion equation as

$$\frac{d}{dt}(\gamma(x)T_e^2) = \nabla_x(\kappa(x)\nabla_x T_e) - G(x)(T_e - T_l) + p(x,t) \tag{2.13}$$

$$C_l\frac{dT_l}{dt} = G(x,T_e)(T_e - T_l) \tag{2.14}$$

$$\tag{2.15}$$

where T_e and T_l are the temperatures of the electron and the lattice subsystems, $C_e(T_e) = \gamma(x)T_e$ and C_l the corresponding heat capacities, $kappa(x)$ is the spatial-dependent thermal conductivity, $G(x,T_e) = \eta(x)T_e + G(x,T_{\text{room}})$ the temperature-dependent electon-lattice coupling constant and $p(x,t)$ the absorbed laser power density, modeled as

$$p(x,t) = p_0 e^{-4\ln 2\left(\frac{t}{\tau_p}\right)^2} e^{\frac{-x}{\delta(x)\cos(\alpha)}} \tag{2.16}$$

γ_{Al} [J nm^{-3} K^{-2}]	91.2×10^{-27}
γ_{Ni} [J nm^{-3} K^{-2}]	1077.4×10^{-27}
$C_{l(\mathrm{Al})}$ [J nm^{-3} K^{-1}]	2.46×10^{-21}
$C_{l(\mathrm{Ni})}$ [J nm^{-3} K^{-1}]	33.78×10^{-21}
κ_{Al} [J ps^{-1} nm^{-1} K^{-1}]	2.3×10^{-19}
κ_{Ni} [J ps^{-1} nm^{-1} K^{-1}]	0.8×10^{-19}
η_{Al} [J ps^{-1} nm^{-3} K^{-2}]	2.4×10^{-26}
η_{Ni} [J ps^{-1} nm^{-3} K^{-2}]	-33×10^{-26}
$G_{\mathrm{Al}}(T_{\mathrm{room}})^*$ [J ps^{-1} nm^{-3} K^{-1}]	2.4×10^{-22}
$G_{\mathrm{Ni}}(T_{\mathrm{room}})^*$ [J ps^{-1} nm^{-3} K^{-1}]	1.0×10^{-22}

Table 2.3: Parameter values for the simulation from eq. 2.13.$*$ T_{room} has been taken as 300 K.

Here τ_p is the FWHM of the excitation, $\delta(x)$ the optical penetration depth of the material and $\cos\alpha$ accounts for the angle of incidence (in this case 45°). The peak power density p_0 is given by

$$p_0 = \frac{2\sqrt{\ln 2}}{\sqrt{\pi\tau_p\delta(x)(1-e^{-d/\delta(x)})}}a(d)F \tag{2.17}$$

which is similar to eq.2.10 but this time the absorbance a has to be calculated for each sample thickness. Table 2.3 lists the parameters used. Since only the initial temperature rise is to be considered, cooling of the lattice and lateral diffusion effects have been glaringly neglected. Note also that eq. 2.13 is very close to the M3TM described in eq. 2.6. However, the thickness of the sample affects the simulation in several ways. For instance, $P(x,t)$ explicitly appears in it, and the spatial dependence of κ,G and C_l implicitly involve it. The absorption of $P(x,t)$ by the electron system is assumed to be instantaneous, since electron-hole pair creation occurs in a sub-10 fs timescale. As d_{Al} increases, the contribution of direct light absorbed by the nickel layer is reduced by the absorption in the aluminum layer. Nevertheless, also more heat is generated in that layer, which eventually diffuses into the ferromagnet. This process is slower the thicker the aluminum layer is. To retrieve the demagnetization time, eq. 2.12 has been computed from the resulting temperature evolution evaluated at 5 nm below the front surface of the nickel layer[15]. Then, from the rising edge of ΔM, t_{d} is determined as the 10 %–90 % rise time. The results can be visualized in the inset of fig. 2.20. They are in good agreement with the experimental values, except at larger thicknesses,

[15]Since the light at 400 nm has an optical penetration of $\approx$ 10 nm in Ni, the Kerr signal is probing deeper than the front surface. Values at the middle point of the Ni layer are, to a first approximation, an average value of the whole layer.

where defects in the Al absorber may be giving the laser a direct pathway to the Ni layer.

In addition to the simulation for diffusion, the dependence of the demagnetization on the thickness of the absorber layer can be inferred from a simple analytical model. In this model, the electron gas temperature is estimated at a time immediately after the experimentally determined demagnetization time t_d. In this way it will be demonstrated that laser light absorption, temperature equilibration within the electron gas and heat conduction from the electron gas to the lattice can account for the that dependence. Let us start with the heat per unit area deposited by the laser pulse:

$$q_{\mathrm{dep,A}} = F_{\mathrm{pump}} a \tag{2.18}$$

where F_{pump} is the pump fluence and $a(d_{\mathrm{Al}})$ the absorbance of the film, which has been computed from [158] by considering multiple reflections between the film surfaces, using the refractive indexes for bulk Al and Ni from [204] and an angle of incidence of 45°. Immediately after the pulse has been absorbed the heat deposited in the electron gas is

$$q_{\mathrm{dep}} = \int_0^d \gamma(x)(T_e^2(x, t=0) - T_0^2)dx \tag{2.19}$$

with $d = d_{\mathrm{Al}} + d_{\mathrm{Ni}}$ and $T_0 = 300\,\mathrm{K}$ the room temperature. Let us now assume that heat diffusion thermalizes the electron gas within the observed demagnetization time t_d. During this process the coupling between the electron and the lattice systems acts as a dissipation mechanism, that is, the rate at which the electronic heat is drained out of the system is

$$\frac{\partial q_{\mathrm{el}}}{\partial t} = -\int_0^d G(x)(T_e(x,t) - T_0)dx \tag{2.20}$$

with $G(x)$ the coupling constant, whose x dependence actually denotes its material dependence. Since the lattice heat capacity is much larger than the electron heat capacity, it is assumed in the last equation that the lattice temperature does not change during the demagnetization time, which is a reasonable approximation [149]. The integral can be also approximated by an average temperature $\bar{T}_e(t)$ if we assume instantaneous thermalization:

$$\frac{\partial q_{\mathrm{el}}}{\partial t} \approx -\bar{G}d(\bar{T}_e(x,t) - T_0)dx \tag{2.21}$$

with $\bar{G} = (G_{\mathrm{Al}}d_{\mathrm{Al}} + G_{\mathrm{Ni}}d_{\mathrm{Ni}})/d$. With a similar argument, it can be assumed that the rate at which heat is dissipated from the system is such that the temperature difference follows an exponential decay due to electron-phonon scattering, i.e., $T_e - T_0 = (T(0) - T_0)e^{-t/\tau}$, with τ being the characteristic time of that decay. Then from eq. 2.19 it follows that

$$\frac{\partial q_{\mathrm{el}}}{\partial t} \approx -\frac{T_0}{\tau}\bar{\gamma}d(\bar{T}_e(t) - T_0) \tag{2.22}$$

where $\bar{\gamma} = (\gamma_{\mathrm{Al}} d_{\mathrm{Al}} + \gamma_{\mathrm{Ni}} d_{\mathrm{Ni}})/d$ and the approximation $T_e^2(t) - T_0^2 \approx 2T_0(T(0) - T_0)e^{-t/\tau}$ to first order in the exponential decay has been utilized. Note that this is only valid for small differences $\bar{T}_e(t) - T_0$. Combining eqs. 2.21 and 2.22 yields

$$\tau = T_0 \frac{\gamma_{\mathrm{Al}} d_{\mathrm{Al}} + \gamma_{\mathrm{Ni}} d_{\mathrm{Ni}}}{G_{\mathrm{Al}} d_{\mathrm{Al}} + G_{\mathrm{Ni}} d_{\mathrm{Ni}}} \tag{2.23}$$

Using τ, the experimental demagnetization times t_{d} from the inset of fig. 2.20 and eq. 2.19 the electron temperature right after the demagnetization, and the demagnetization amplitude, can be estimated as

$$T_e \approx \left(\sqrt{\frac{2q_{\mathrm{dep}}}{\bar{\gamma} d} + T_0^2} - T_0 \right) e^{-t_{\mathrm{d}}/\tau} + T_0 \tag{2.24}$$

$$\Delta M \propto (T_e^2 - T_0^2) \tag{2.25}$$

The results can be seen in fig. 2.20. The demagnetization amplitude is qualitatively reproduced by the previous model, which incorporated total thermalization and heat transport to the lattice as an infinite reservoir. The discrepancies, specially for $d_{\mathrm{Al}} > 40\,\mathrm{nm}$, are likely caused by the approximations. For instance, for short t_{d} one has to consider the exact shape of the temperature distribution in eq. 2.21. Also the approximation to first order in eq. 2.22 does not hold for short times or higher temperature differences.

2.6.4 Conclusions

In this experiment indirect demagnetization of a ferromagnet by optical pumping through a non-magnetic metal of varying thickness has been demonstrated. The observed behavior shows two regimes. For aluminum absorber thicknesses $d_{\mathrm{Al}} \leq 30\,\mathrm{nm}$ optical transmission through the Al film directly excites the ferromagnet and dominates over the heat transport of the electron gas. This is indicated by the match of the decay length that both the non-magnetic specular optical Kerr effect (SOKE) and the optical absorption exhibit. Thicknesses $d_{\mathrm{Al}} \geq 30\,\mathrm{nm}$, in contrast, show that the Ni film is demagnetized by the transport of hot electrons from the absorber layer. The diffusion of these electrons causes a longer demagnetization time t_{d} for thicker absorber layers. The dependence of t_{d} with the layer thickness can be reproduced by solving the diffusion equation for the electron system coupled with the lattice reservoir. The demagnetization amplitudes can be estimated by a simplified analytical model that assumes rapid thermalization within the electron gas as well as heat dissipation to the lattice. It is concluded that transport of heat by diffusion is a good approximation to describe indirect demagnetization through a non-magnetic absorber layer at the thickness ranges investigated in this experiment.

2.7 Summary and conclusions

In this chapter experiments based on the magneto-optical Kerr effect have been carried out to add evidence on the ultrafast demagnetization dynamics of single-domain ferromagnetic thin films, with emphasis in nickel. First, a brief summary of the different approaches for the demagnetization mechanisms, both theoretical and experimental, has been laid out. The central framework whence the most recent developments depart is the three temperature model, which describes the evolution of the system in terms of the interaction between three coupled sub-systems, the electrons, the spins and the lattice, for which an individual dynamical temperature is assigned. The advantages and the disadvantages of this model have been elaborated on, and the validity of its assumptions challenged by the latest research. It has been shown that the underlying mechanisms of angular momentum transfer are still under strong debate, and it has been pointed out that elements such as the sample geometry and material, the excitation characteristics and external variables like temperature, can greatly influence the outcome of the experiments, making the elaboration of a unified theory even more challenging.

In the first experiment, the demagnetization process has been studied after varying the pump excitation length. It has been concluded that dynamics at the picosecond timescale can be derived from dynamics at the femtosecond timescale, while the thermalization time of the electrons to the lattice separates these two regimes. It has also been highlighted that the the laser pulse represents the limiting factor for pulse lengths on the order of the thermalization time. In the second experiment, the dynamical effect of preheating the sample at different time delays has been investigated through a double pump pulse setup. It has been confirmed that the demagnetization slows down due to the addition of energy from the heating excitation. The linearity of the system response to the double pulse has been analyzed and compared with a conspicuous modified version of the 3TM. While both the model and the experiment predict a nonlinearity in the first few picoseconds, several discrepancies between the two have been found. The strongest nonlinearities have been found at pump delays shorter than the thermalization time of the electrons with the lattice, i.e. when the system is still in a state of non-equilibrium. In order to take sensible conclusions further research needs to be performed in this line. Finally, a third experiment has examined the effect of transport in the demagnetization process by using an absorber layer from which hot electrons could be generated and driven to the ferromagnet. It has been observed that for small absorber thicknesses, direct excitation of the ferromagnet by the transmitted optical pump dominates over heat transport, whereas the latter plays a stronger role for thicker layers. A simplified analytical model based on a rapid thermalization as-

sumption, as well as heat dissipation to an infinite lattice reservoir supports this explanation. Numerically solving the heat diffusion equation predicts the observed increase in the demagnetization times with absorber thickness, with the gratest discrepancies in the thickest films.

Although it can be stated that the magnetization dynamics at timescales on the order of or larger than the thermalization time of all sub-systems is fairly well understood and reproduced by the research so far, the interaction of this sub-systems, and particularly the exact mechanism underlying the transfer of angular momentum during the first few hundred femtoseconds, is still an open debate. Besides the *on site* pathways for transfer of angular momentum (spin-flip scattering, electron-magnon, photon induced, etc.) varied types of ballistic, ballistic-diffusive and diffusive processes have been contemplated in the literature. Further studies shall be directed toward testing the influence of each regime in all possible materials and geometries. Since the different proposed mechanism seem to describe the experiments with different degrees of accuracy, it is most likely that a combination thereof needs to be taken into account and conveniently accommodated to each particular sample and experimental environment.

Bibliography

[1] Abela, R. et al. *XFEL: the european x-ray free-electron laser - technical design report*. DESY, Hamburg (2006). ISBN 978-3-935702-17-1.

[2] Ackermann, W. et al. *Operation of a free-electron laser from the extreme ultraviolet to the water window*. Nat Photon, 1(6):pp. 336–342 (2007). ISSN 1749-4885.

[3] Aeschlimann, M., Bauer, M. and Pawlik, S. *Surface reaction dynamics competing nonradiative channels for hot electron induced surface photochemistry*. Chemical Physics, 205(1):pp. 127 – 141 (1996). ISSN 0301-0104.

[4] Aeschlimann, M. et al. *Ultrafast spin-dependent electron dynamics in fcc co*. Physical Review Letters, 79(25):pp. 5158–5161 (1997).

[5] Aeschlimann, M. et al. *Transport and dynamics of optically excited electrons in metals*. Applied Physics A, 71(5):pp. 485–491 (2000). ISSN 1432-0630.

[6] Agababyan, A. et al. *Multi-processor based fast data acquisition for a free electron laser and experiments*. In *Real-Time Conference, 2007 15th IEEE-NPSS*, pp. 1–5 (2007).

[7] Argyres, P. N. *Theory of the faraday and kerr effects in ferromagnetics*. Phys. Rev., 97(2):pp. 334–345 (1955).

[8] Aryasetiawan, F. and Gunnarsson, O. *The GW method*. Rep. Prog. Phys., 61(3):pp. 237–312 (1998).

[9] Atxitia, U. *Modeling of ultrafast laser-induced magnetization dynamics within the Landau-Lifshitz-Bloch approach*. Ph.D. thesis (2012).

[10] Atxitia, U. and Chubykalo-Fesenko, O. *Ultrafast magnetization dynamics rates within the landau-lifshitz-bloch model*. Phys. Rev. B, 84:p. 144414 (2011).

[11] Atxitia, U. et al. *Evidence for thermal mechanisms in laser-induced femtosecond spin dynamics*. Phys. Rev. B, 81(17) (2010).

[12] Aune, B. et al. *Superconducting tesla cavities*. Phys. Rev. ST Accel. Beams, 3:p. 092001 (2000).

[13] Ayvazyan, V. et al. *Generation of gw radiation pulses from a vuv free-electron laser operating in the femtosecond regime*. Phys. Rev. Lett., 88:p. 104802 (2002).

[14] Ayvazyan, V. et al. *First operation of a free-electron laser generating gw power radiation at 32 nm wavelength*. The European Physical Journal D-Atomic, Molecular, Optical and Plasma Physics, 37(2):pp. 297–303 (2006).

[15] Baek, I.-G. et al. *Spin reorientation transition in fe(110) thin films: The role of surface anisotropy*. Phys. Rev. B, 67:p. 075401 (2003).

[16] Banerjee, T., Lodder, J. C. and Jansen, R. *Origin of the spin-asymmetry of hot-electron transmission in fe*. Phys. Rev. B, 76(14) (2007).

[17] Baral, A. et al. *Re-examination of the elliott-yafet spin-relaxation mechanism*. New Journal of Physics, 18(2):p. 023012 (2016).

[18] Bass, J. and Jr, W. P. P. *Spin-diffusion lengths in metals and alloys, and spin-flipping at metal/metal interfaces: an experimentalist's critical review*. Journal of Physics: Condensed Matter, 19(18):p. 183201 (2007).

[19] Battiato, M., Carva, K. and Oppeneer, P. M. *Superdiffusive spin transport as a mechanism of ultrafast demagnetization*. Phys. Rev. Lett., 105:p. 027203 (2010).

[20] Battiato, M., Carva, K. and Oppeneer, P. M. *Theory of laser-induced ultrafast superdiffusive spin transport in layered heterostructures*. Phys. Rev. B, 86:p. 024404 (2012).

[21] Battiato, M., Maldonado, P. and Oppeneer, P. M. *Treating the effect of interface reflections on superdiffusive spin transport in multilayer samples (invited)*. J. Appl. Phys., 115(17):p. 172611 (2014).

[22] Bauer, M. and Aeschlimann, M. *Dynamics of excited electrons in metals, thin films and nanostructures*. Journal of Electron Spectroscopy and

Related Phenomena, 124(2–3):pp. 225 – 243 (2002). ISSN 0368-2048. Frontiers in photoemission spectroscopy of solids and surfaces.

[23] Bauer, M., Marienfeld, A. and Aeschlimann, M. *Hot electron lifetimes in metals probed by time-resolved two-photon photoemission*. Progress in Surface Science, 90(3):pp. 319 – 376 (2015). ISSN 0079-6816.

[24] Baym, G. and Pethick, C. *Landau Fermi-liquid theory: concepts and applications*. John Wiley & Sons (2008).

[25] Beaulieu, N. et al. *Space charge effects occurring during fast demagnetization processes*. In *Ultrafast Magnetism I. Proceedings of the International Conference UMC*, edited by J.-Y. Bigot, W. Hübner, T. Rasing and R. Chantrell, vol. 159 of *Springer Proceedings in Physics*, pp. 313–316. Springer International Publishing (2013).

[26] Beaurepaire, E. et al. *Ultrafast spin dynamics in ferromagnetic nickel*. Phys. Rev. Lett., 76:pp. 4250–4253 (1996).

[27] Bechtel, J. H., Lee Smith, W. and Bloembergen, N. *Two-photon photoemission from metals induced by picosecond laser pulses*. Phys. Rev. B, 15:pp. 4557–4563 (1977).

[28] Berden, G. et al. *Benchmarking of electro-optic monitors for femtosecond electron bunches*. Phys. Rev. Lett., 99:p. 164801 (2007).

[29] Bigot, J.-Y. and Vomir, M. *Ultrafast magnetization dynamics of nanostructures*. Annalen der Physik, 525(1-2):pp. 2–30 (2013). ISSN 1521-3889.

[30] Bigot, J.-Y., Vomir, M. and Beaurepaire, E. *Coherent ultrafast magnetism induced by femtosecond laser pulses*. Nat Phys, 5(7):pp. 515–520 (2009). ISSN 1745-2473.

[31] Bigot, J.-Y. et al. *Femtosecond spectrotemporal magneto-optics*. Phys. Rev. Lett., 93(7) (2004).

[32] Bonn, M. et al. *Ultrafast electron dynamics at metal surfaces: Competition between electron-phonon coupling and hot-electron transport*. Physical Review B, 61(2):p. 1101 (2000).

[33] Borland, M. *Progress toward an ultimate storage ring light source*. Journal of Physics: Conference Series, 425(4):p. 042016 (2013).

[34] Bowen, H. G. *The Edison effect*. West Orange, N.J., Thomas Alva Edison Foundation (1951).

[35] Brillo, J., Kuhlenbeck, H. and Freund, H.-J. *Interaction of {O2} with wc(0001)*. Surface Science, 409(2):pp. 199 – 206 (1998). ISSN 0039-6028.

[36] Brinkmann, R. et al. *An x-ray {FEL} laboratory as part of a linear collider design*. Nuclear Instruments and Methods in Physics Research Section A: Accelerators, Spectrometers, Detectors and Associated Equipment, 393(1-3):pp. 86–92 (1997). ISSN 0168-9002. Free Electron Lasers 1996.

[37] Brorson, S. D., Fujimoto, J. G. and Ippen, E. P. *Femtosecond electronic heat-transport dynamics in thin gold films*. Phys. Rev. Lett., 59:pp. 1962–1965 (1987).

[38] Bytchkov, A. et al. *Development of mcp-based photon diagnostics at the tesla test facility at desy*. Nuclear Instruments and Methods in Physics Research Section A: Accelerators, Spectrometers, Detectors and Associated Equipment, 528(1-2):pp. 254 – 257 (2004). ISSN 0168-9002. Proceedings of the 25th International Free Electron Laser Conference, and the 10th {FEL} Users Workshop.

[39] Cao, J. et al. *Femtosecond photoemission study of ultrafast electron dynamics on cu(100)*. Phys. Rev. B, 56:pp. 1099–1102 (1997).

[40] Cao, J. et al. *Femtosecond photoemission study of ultrafast electron dynamics in single-crystal au(111) films*. Physical Review B, 58(16):pp. 10948–10952 (1998).

[41] Carpene, E. *Ultrafast laser irradiation of metals: Beyond the two-temperature model*. Phys. Rev. B, 74:p. 024301 (2006).

[42] Carpene, E. et al. *Dynamics of electron-magnon interaction and ultrafast demagnetization in thin iron films*. Phys. Rev. B, 78:p. 174422 (2008).

[43] Carpene, E. et al. *Measurement of the magneto-optical response of fe and CrO 2 epitaxial films by pump-probe spectroscopy: Evidence for spin-charge separation*. Phys. Rev. B, 87(17) (2013).

[44] Carva, K., Battiato, M. and Oppeneer, P. M. *Ab initio investigation of the elliott-yafet electron-phonon mechanism in laser-induced ultrafast demagnetization*. Phys. Rev. Lett., 107:p. 207201 (2011).

[45] Carva, K., Legut, D. and Oppeneer, P. M. *Influence of laser-excited electron distributions on the x-ray magnetic circular dichroism spectra: Implications for femtosecond demagnetization in ni*. EPL (Europhysics Letters), 86(5):p. 57002 (2009).

[46] Carva, K. et al. *Ab initio theory of electron-phonon mediated ultrafast spin relaxation of laser-excited hot electrons in transition-metal ferromagnets*. Phys. Rev. B, 87:p. 184425 (2013).

[47] Sinković, B., Shekel, E. and Hulbert, S. L. *Spin-resolved iron surface density of states*. Phys. Rev. B, 52:pp. R8696–R8699 (1995).

[48] Chantler, C. et al. *X-ray form factor, attenuation and scattering tables* (2005).

[49] Chapman, H. N. *Disruptive photon technologies for chemical dynamics*. Faraday Discuss., 171:pp. 525–543 (2014).

[50] Chen, G. *Ballistic-diffusive heat-conduction equations*. Phys. Rev. Lett., 86:pp. 2297–2300 (2001).

[51] Chevallay, E. et al. *Photocathodes tested in the dc gun of the CERN photoemission laboratory*. Nuclear Instruments and Methods in Physics Research Section A: Accelerators, Spectrometers, Detectors and Associated Equipment, 340(1):pp. 146 – 156 (1994). ISSN 0168-9002.

[52] Cinchetti, M. et al. *Spin-flip processes and ultrafast magnetization dynamics in co: Unifying the microscopic and macroscopic view of femtosecond magnetism*. PHYSICAL REVIEW LETTERS, 97(17) (2006). ISSN 0031-9007.

[53] Comin, A. et al. *Femtosecond dynamics of co thin films on si support*. Solid State Communications, 129(4):pp. 227 – 231 (2004). ISSN 0038-1098.

[54] Cooper, P. S. et al. *Polarized electron-electron scattering at gev energies*. Phys. Rev. Lett., 34:pp. 1589–1592 (1975).

[55] Costa, A. T., Muniz, R. B. and Mills, D. L. *Theory of large-wave-vector spin waves in ultrathin ferromagnetic films: Sensitivity to electronic structure*. Phys. Rev. B, 70(5) (2004).

[56] Crangle, J. and Goodman, G. M. *The magnetization of pure iron and nickel*. Proceedings of the Royal Society A: Mathematical, Physical and Engineering Sciences, 321(1547):pp. 477–491 (1971).

[57] Cultrera, L., Gatti, G. and Lorusso, A. *Photoemission studies on yttrium thin films*. Radiation Effects and Defects in Solids, 165(6-10):pp. 609–617 (2010).

[58] Czuba, K. and Weddig, H. C. *Design considerations for the rf phase reference distribution system for x-ray fel and tesla*. In *Photonics Applications*

in Astronomy, Communications, Industry, and High-Energy Physics Experiments II, vol. 5484, pp. 148–152. SPIE (2004).

[59] Dalla Longa, F. *Laser-induced magnetization dynamics*. Ph.D. thesis (2008).

[60] Dalla Longa, F. et al. *Influence of photon angular momentum on ultrafast demagnetization in nickel*. Phys. Rev. B, 75:p. 224431 (2007).

[61] Daniel, M., Arun, R. and Sabareesan, P. *Impact of magnetic surface anisotropy on the precessional switching of magnetization in pt-alloy nanofilms*. Physica B: Condensed Matter, 407(17):pp. 3352 – 3359 (2012). ISSN 0921-4526.

[62] Day, P. *The philosopher's tree: a selection of Michael Faraday's writings*. CRC Press (1999).

[63] Dekker, A. *Secondary electron emission*. In *Advances in Research and Applications*, edited by F. Seitz and D. Turnbull, vol. 6 of *Solid State Physics*, pp. 251 – 311. Academic Press (1958).

[64] Del Fatti, N. et al. *Nonequilibrium electron interactions in metal films*. Physical review letters, 81(4):p. 922 (1998).

[65] Del Fatti, N. et al. *Nonequilibrium electron dynamics in noble metals*. Physical Review B, 61(24):p. 16956 (2000).

[66] Dell'Angela, M. et al. *Vacuum space charge effects in sub-picosecond soft x-ray photoemission on a molecular adsorbate layer*. Structural Dynamics, 2(2):025101 (2015).

[67] van Dijken, S., Jiang, X. and Parkin, S. S. *Spin-dependent hot electron transport in ni 81 fe 19 and co 84 fe 16 films on gaas (001)*. Phys. Rev. B, 66(9):p. 094417 (2002).

[68] Djordjevic, M. and Münzenberg, M. *Connecting the timescales in picosecond remagnetization experiments*. Phys. Rev. B, 75(1) (2007).

[69] Elliott, R. J. *Theory of the effect of spin-orbit coupling on magnetic resonance in some semiconductors*. Phys. Rev., 96:pp. 266–279 (1954).

[70] Elyasi, M. and Yang, H. *Optically induced spin-dependent diffusive transport in the presence of spin-orbit interaction for all-optical magnetization reversal*. Physical Review B, 94(2):p. 024417 (2016).

[71] Emma, P. et al. *First lasing and operation of an angstrom-wavelength free-electron laser*. Nat Photon, 4(9):pp. 641–647 (2010). ISSN 1749-4885.

[72] Eschenlohr, A. et al. *Ultrafast spin transport as key to femtosecond demagnetization*. Nat Mater, 12(4):pp. 332–336 (2013). ISSN 1476-1122. Demagnetization fit exponential curve.

[73] Eschenlohr, A. et al. *Reply to'optical excitation of thin magnetic layers in multilayer structures'*. Nature materials, 13(2):pp. 102–103 (2014).

[74] Essert, S. and Schneider, H. C. *Electron-phonon scattering dynamics in ferromagnetic metals and their influence on ultrafast demagnetization processes*. Phys. Rev. B, 84:p. 224405 (2011).

[75] Fähnle, M. and Illg, C. *Electron theory of fast and ultrafast dissipative magnetization dynamics*. Journal of Physics: Condensed Matter, 23(49):p. 493201 (2011).

[76] Fann, W. S. et al. *Direct measurement of nonequilibrium electron-energy distributions in subpicosecond laser-heated gold films*. Physical Review Letters, 68(18):pp. 2834–2837 (1992).

[77] Fann, W. S. et al. *Electron thermalization in gold*. Phys. Rev. B, 46:pp. 13592–13595 (1992).

[78] Ferrini, G. et al. *Linear and nonlinear total-yield photoemission observed in the subpicosecond regime in mo*. Phys. Rev. B, 60:pp. 8383–8387 (1999).

[79] Flöttmann, K., Lidia, S. M. and Piot, P. *Recent improvements to the ASTRA particle tracking code*. In *Proceedings of the Particle Accelerator Conference*, edited by J. Chew, vol. 5, pp. 3500–3503. Stanford Linear Accelerator Center, Lawrence Berkeley National Laboratory, Portland, Oregon (2003).

[80] Flöttmann, K., Limberg, T. and Piot, P. *Generation of ultrashort electron bunches by cancellation of nonlinear distortions in the longitudinal phase space*. TESLA FEL Report 6, TESLA Technology Collaboration (TTC) (2001).

[81] Fognini, A. et al. *Magnetic pulser and sample holder for time- and spin-resolved photoemission spectroscopy on magnetic materials*. Review of Scientific Instruments, 83(6):063906 (2012).

[82] Fognini, A. et al. *The role of space charge in spin-resolved photoemission experiments*. New Journal of Physics, 16(4):p. 043031 (2014).

[83] Fognini, A. et al. *The influence of the excitation pulse length on ultrafast magnetization dynamics in nickel*. Structural Dynamics, 2(2):p. 024501 (2015).

[84] Gahl, C. et al. *A femtosecond x-ray//optical cross-correlator*. Nat Photon, 2(3):pp. 165–169 (2008). ISSN 1749-4885.

[85] Ganeev, R. A. *High-order harmonic generation in a laser plasma: a review of recent achievements*. Journal of Physics B: Atomic, Molecular and Optical Physics, 40(22):p. R213 (2007).

[86] Garduño-Mejía, J., Higlett, M. P. and Meech, S. R. *Modelling the influence of nonthermal electron dynamics in thin and ultrathin gold films*. Chemical Physics, 341(1–3):pp. 276 – 284 (2007). ISSN 0301-0104. Ultrafast Dynamics of Molecules in the Condensed Phase: Photon Echoes and Coupled ExcitationsA Tribute to Douwe A. Wiersma.

[87] Gay, T. J. and Dunning, F. B. *Mott electron polarimetry*. Review of Scientific Instruments, 63(2):pp. 1635–1651 (1992).

[88] Gerasimova, N., Dziarzhytski, S. and Feldhaus, J. *The monochromator beamline at flash: performance, capabilities and upgrade plans*. Journal of Modern Optics, 58(16):pp. 1480–1485 (2011).

[89] Getzlaff, M., Bansmann, J. and Schönhense, G. *Spin-polarization effects for electrons passing through thin iron and cobalt films*. Solid State Communications, 87(5):pp. 467 – 469 (1993). ISSN 0038-1098.

[90] Gilton, T. L. et al. *Intense surface photoemission: Space charge effects and self-acceleration*. Journal of Applied Physics, 68(9):pp. 4802–4810 (1990).

[91] Girardeau-Montaut, C. and Girardeau-Montaut, J. P. *Space-charge effect on the energy spectrum of photoelectrons produced by high-intensity short-duration laser pulses on a metal*. Phys. Rev. A, 44:pp. 1409–1411 (1991).

[92] Goldmann, A. *Magnetic transition metals*, vol. 23c2 of *Landolt-Börnstein - Group III Condensed Matter*. Springer Berlin Heidelberg (1999).

[93] Goris, A. et al. *Role of spin-flip exchange scattering for hot-electron lifetimes in cobalt*. Phys. Rev. Lett., 107:p. 026601 (2011).

[94] Graves, C. E. et al. *Nanoscale spin reversal by non-local angular momentum transfer following ultrafast laser excitation in ferrimagnetic gdfeco*. Nat Mater, 12(4):pp. 293–298 (2013). ISSN 1476-1122.

[95] Graves, W. S. et al. *Intense superradiant x rays from a compact source using a nanocathode array and emittance exchange*. Phys. Rev. Lett., 108:p. 263904 (2012).

[96] Groeneveld, R. H. M., Sprik, R. and Lagendijk, A. *Femtosecond spectroscopy of electron-electron and electron-phonon energy relaxation in ag and au*. Phys. Rev. B, 51:pp. 11433–11445 (1995).

[97] Gudat, W. and O.Rader. *Magnetic transition metals*, vol. 23c2 of *Landolt-Börnstein - Group III Condensed Matter*. Springer Berlin Heidelberg (1999).

[98] Guidoni, L., Beaurepaire, E. and Bigot, J.-Y. *Magneto-optics in the ultrafast regime: Thermalization of spin populations in ferromagnetic films*. Phys. Rev. Lett., 89(1) (2002).

[99] Gutt, C. et al. *Single-pulse resonant magnetic scattering using a soft x-ray free-electron laser*. Phys. Rev. B, 81:p. 100401 (2010).

[100] Haag, M., Illg, C. and Fähnle, M. *Theory of scattering of crystal electrons at magnons*. Physical Review B, 87(21):p. 214427 (2013).

[101] Haag, M., Illg, C. and Fähnle, M. *Role of electron-magnon scatterings in ultrafast demagnetization*. Phys. Rev. B, 90(1) (2014).

[102] Hallwachs, W. *Üeber den einfluss des lichtes auf elektrostatisch geladene körper - deutsche digitale bibliothek* (1888).

[103] Hanh, D. W. and Özisik, M. N. *Heat conduction*. John Wiley & Sons, 3rd ed. (2012). ISBN 978-0-470-90293-6.

[104] Heil, J. et al. *Real space imaging of ballistic carrier propagation in bi single crystals*. Phys. Rev. Lett., 74:pp. 146–149 (1995).

[105] Heil, J. et al. *Electron focusing in ag and w single crystals*. Phys. Rev. B, 54:pp. R2280–R2283 (1996).

[106] Hellmann, S. et al. *Ultrafast melting of a charge-density wave in the mott insulator* 1t-tas_2. Phys. Rev. Lett., 105:p. 187401 (2010).

[107] Hellmann, S. et al. *Time-resolved x-ray photoelectron spectroscopy at flash*. New Journal of Physics, 14(1):p. 013062 (2012).

[108] Hertz, H. *Über einen einfluss des ultravioletten lichtes auf die electrische entladung*. Annalen der Physik, 267(8):pp. 983–1000 (1887). ISSN 1521-3889.

[109] Hilbert, M. and López, P. *The world's technological capacity to store, communicate, and compute information*. Science, 332(6025):pp. 60–65 (2011). ISSN 0036-8075.

[110] Hofler, A., Evtushenko, P. and Marhauser, F. *Optimizing SRF gun cavity profiles in a genetic algorithm framework*. In *Proceedings of the 10th International Computational Accelerator Physics Conference*, edited by J. Chew, THPSC020, pp. 296–298. San Francisco, California (2009).

[111] Hohlfeld, J. et al. *Time-resolved thermoreflectivity of thin gold films and its dependence on film thickness*. Applied Physics B, 64(3):pp. 387–390 (1997). ISSN 1432-0649.

[112] Hohlfeld, J. et al. *Electron and lattice dynamics following optical excitation of metals*. Chemical Physics, 251(1–3):pp. 237 – 258 (2000). ISSN 0301-0104.

[113] Huang, Z. *Brightness and coherence of synchrotron radiation and fels*. In *IPAC2013: Proceedings of the 4th International Particle Accelerator Conference*, edited by Z. Dai, C. Petit-Jean-Genaz, V. RW Schaa and C. Zhang, MOYCB101. International Particle Accelerator Conference (2013).

[114] Hübner, W. and Zhang, G. *Ultrafast spin dynamics in nickel*. Physical Review B, 58(10):p. R5920 (1998).

[115] Hüfner, S. *Photoelectron Spectroscopy*. Springer (2010). ISBN 3642075207.

[116] Hüning, M. and Schlarb, H. *Measurement of the beam energy spread in the TTF photo-injector*. In *Proceedings of the Particle Accelerator Conference*, edited by J. Chew, vol. 5, pp. 2074–2076. Stanford Linear Accelerator Center, Lawrence Berkeley National Laboratory, Portland, Oregon (2003).

[117] Hüning, M. et al. *Observation of femtosecond bunch length using a transverse deflecting structure*. In *Proceedings of the 27th International Free-Electron Laser Conference*, edited by H.-D. Nuhn and R. Reitmeyer, TUBAU06. SLAC, SLAC, Arrillaga Alumni Center, Stanford University, Palo Alto, California (2005).

[118] Hübner, W. and Zhang, G. *Femtosecond spin dynamics probed by linear and nonlinear magneto-optics*. Journal of Magnetism and Magnetic Materials, 189(1):pp. 101–105 (1998).

[119] Illg, C., Haag, M. and Fähnle, M. *Ultrafast demagnetization after laser irradiation in transition metals: Ab initio calculations of the spin-flip electron-phonon scattering with reduced exchange splitting*. Phys. Rev. B, 88(21) (2013).

[120] Iwasaki, S.-I. *Perpendicular magnetic recording focused on the origin and its significance*. IEEE transactions on magnetics, 38(4):pp. 1609–1614 (2002).

[121] Iwasaki, S.-i. and Nakamura, Y. *An analysis for the magnetization mode for high density magnetic recording*. IEEE Transactions on Magnetics, 13(5):pp. 1272–1277 (1977).

[122] Jaeglé, P. *Coherent Sources of XUV Radiation. Soft X-Ray Lasers and High-Order Harmonic Generation*, vol. 106 of *Springer Series in Optical Sciences*. Springer-Verlag New York, 1 ed. (2006).

[123] Jansen, R. *The spin-valve transistor: a review and outlook*. Journal of Physics D: Applied Physics, 36(19):p. R289 (2003).

[124] Jenkins, D. et al. *Advanced optical and magneto-optical recording techniques: a review*. Microsystem Technologies, 10(1):pp. 66–75 (2003). ISSN 1432-1858.

[125] Jiles, D. C. *Introduction to Magnetism and Magnetic Materials, Second Edition*. CRC Press, 2 edition ed. ISBN 978-0-412-79860-3.

[126] Johnston, L. *Read and write speeds as they relate to data storage*.

[127] Kaltenborn, S. and Schneider, H. C. *Spin-orbit coupling effects on spin-dependent inelastic electronic lifetimes in ferromagnets*. Phys. Rev. B, 90:p. 201104 (2014).

[128] Kaltenborn, S. and Schneider, H. C. *Inelastic electron lifetimes in simple metals: Influence of spin-orbit coupling*. Phys. Status Solidi RRL, 9(7):pp. 436–439 (2015).

[129] van Kampen, M. *Ultrafast spin dynamics in ferromagnetic metals*. Ph.D. thesis, Technische Universiteit Eindhoven (2003).

[130] van Kampen, M. et al. *Sub-picosecond electron and phonon dynamics in nickel*. Journal of Physics: Condensed Matter, 17(43):p. 6823 (2005).

[131] Kampfrath, T. et al. *Ultrafast magneto-optical response of iron thin films*. Phys. Rev. B, 65:p. 104429 (2002).

[132] Kampfrath, T. et al. *Terahertz spin current pulses controlled by magnetic heterostructures*. Nat Nano, 8(4):pp. 256–260 (2013). ISSN 1748-3387.

[133] Kerr, J. *A new relation between electricity and light: dielectrified media birefringent*. 50 (1875).

[134] Kessler, J. *Electron spin polarization by low-energy scattering from unpolarized targets*. Rev. Mod. Phys., 41:pp. 3–25 (1969).

[135] Kessler, J. *Polarized electrons*, vol. 1. Springer Science & Business Media, first ed. (1976).

[136] Khorsand, A. et al. *Optical excitation of thin magnetic layers in multilayer structures*. Nature materials, 13(2):pp. 101–102 (2014).

[137] Kim, J. et al. *Large scale timing distribution and rf-synchronization for fel facilities*. In *Proceedings of the 26th International Free-Electron Laser Conference*. Synchrotrone Trieste, Synchrotrone Trieste, Italy (2004).

[138] Kim, K.-J. *Rf and space-charge effects in laser-driven rf electron guns*. Nuclear Instruments and Methods in Physics Research Section A: Accelerators, Spectrometers, Detectors and Associated Equipment, 275(2):pp. 201 – 218 (1989). ISSN 0168-9002.

[139] Kirilyuk, A., Kimel, A. V. and Rasing, T. *Ultrafast optical manipulation of magnetic order*. Rev. Mod. Phys., 82:pp. 2731–2784 (2010).

[140] Kleinpoppen, H. and Newell, W. *Polarized Electron/Polarized Photon Physics*. Physics of Atoms and Molecules. Springer US, first ed. (1995).

[141] Knoesel, E., Hotzel, A. and Wolf, M. *Ultrafast dynamics of hot electrons and holes in copper: Excitation, energy relaxation, and transport effects*. Phys. Rev. B, 57:pp. 12812–12824 (1998).

[142] Knorren, R., Bouzerar, G. and Bennemann, K. H. *Theory for transport and temperature effects on two-photon photoemission: Application to cu*. Phys. Rev. B, 63:p. 125122 (2001).

[143] Knorren, R. et al. *Dynamics of excited electrons in copper and ferromagnetic transition metals: Theory and experiment*. Phys. Rev. B, 61:pp. 9427–9440 (2000).

[144] Koopmans, B. *Time-resolved Kerr-effect and Spin Dynamics in Itinerant Ferromagnets*. John Wiley & Sons, Ltd (2007). ISBN 9780470022184.

[145] Koopmans, B., Van Kampen, M. and De Jonge, W. *Experimental access to femtosecond spin dynamics*. Journal of Physics: Condensed Matter, 15(5):p. S723 (2003).

[146] Koopmans, B. et al. *Ultrafast magneto-optics in nickel: Magnetism or optics?* Phys. Rev. Lett., 85:pp. 844–847 (2000).

[147] Koopmans, B. et al. *Microscopic model for femtosecond magnetization dynamics*. Journal of Magnetism and Magnetic Materials, 286:pp. 271 – 275 (2005). ISSN 0304-8853. Proceedings of the 5th International Symposium on Metallic Multilayers.

[148] Koopmans, B. et al. *Unifying ultrafast magnetization dynamics*. Phys. Rev. Lett., 95:p. 267207 (2005).

[149] Koopmans, B. et al. *Explaining the paradoxical diversity of ultrafast laser-induced demagnetization*. Nat Mater, 9(3):pp. 259–265 (2010). ISSN 1476-1122.

[150] von Korff Schmising, C. et al. *Nonlocal ultrafast demagnetization dynamics of co/pt multilayers by optical field enhancement*. New Journal of Physics, 17(3):p. 033047 (2015).

[151] Krasilnikov, M. et al. *Pitz status, recent measurements and tests*. In *Proceedings of the 34th International Free-Electron Laser Conference*, edited by T. Tanaka and V. R. Schaa, MOPD59. Spring-8 and Kioto University, Nara Prefectural New Public Hall, Japan (2012).

[152] Krauss, M. et al. *Ultrafast demagnetization of ferromagnetic transition metals: The role of the coulomb interaction*. Phys. Rev. B, 80:p. 180407 (2009).

[153] Kronmüller, H. and Parkin, S. S. *Handbook of magnetism and advanced magnetic materials*. John Wiley & Sons (2007).

[154] Kruglyak, V. et al. *Measurement of hot electron momentum relaxation times in metals by femtosecond ellipsometry*. Physical Review B, 71(23):p. 233104 (2005).

[155] Kutnyakhov, D. et al. *Imaging spin filter for electrons based on specular reflection from iridium (001)*. Ultramicroscopy, 130:pp. 63–69 (2013).

[156] Lambert, G. et al. *Injection of harmonics generated in gas in a free-electron laser providing intense and coherent extreme-ultraviolet light*. Nat Phys, 4(4):pp. 296–300 (2008). ISSN 1745-2473.

[157] Landau, L. D. and Lifshitz, E. *On the theory of the dispersion of magnetic permeability in ferromagnetic bodies*. Phys. Z. Sowjetunion, 8(153):pp. 101–114 (1935).

[158] Landry, J. P. *Optical oblique-incidence reflectivity difference microscopy: Application to label-free detection of reactions in biomolecular microarrays*. Ph.D. thesis, University of California, Davis (2008).

[159] Lenard, P. *Ueber die lichtelektrische wirkung*. Annalen der Physik, 313(5):pp. 149–198 (1902). ISSN 1521-3889.

[160] Lewis, E. P. *The effects of a magnetic field on radiation*. American Book Company (1900).

[161] Lisowski, M. et al. *Femtosecond dynamics and transport of optically excited electrons in epitaxial cu films on si(111)*. Appl. Phys. A, 79(4-6):pp. 739–741 (2004).

[162] Lisowski, M. et al. *Ultra-fast dynamics of electron thermalization, cooling and transport effects in ru(001)*. Applied Physics A, 78(2):pp. 165–176 (2004). ISSN 0947-8396.

[163] Lisowski, M. et al. *Femtosecond electron and spin dynamics in gd(0001) studied by time-resolved photoemission and magneto-optics*. Physical Review Letters, 95(13) (2005).

[164] Liu, X., Stock, R. and Rudolph, W. *Ballistic electron transport in au films*. Phys. Rev. B, 72:p. 195431 (2005).

[165] Löhl, F., Hacker, K. and Schlarb, H. *A sub-50 femtosecond bunch arrival time monitor system for FLASH*. In *Proceedings of the 8th European Workshop on Beam Diagnostics and Instrumentation for Particle Accelerators*, edited by I. Andrian and V. R. Schaa, WEPB15. Elettra, Fermi, NH Laguna Palace, Venice, Italy (2007).

[166] Löhl, F. et al. *Measurements of the transverse emittance at the flash injector at desy*. Phys. Rev. ST Accel. Beams, 9:p. 092802 (2006).

[167] Löhl, F. et al. *Electron bunch timing with femtosecond precision in a superconducting free-electron laser*. Phys. Rev. Lett., 104:p. 144801 (2010).

[168] Malinowski, G. et al. *Control of speed and efficiency of ultrafast demagnetization by direct transfer of spin angular momentum*. Nat Phys, 4(11):pp. 855–858 (2008). ISSN 1745-2473.

[169] Maltezopoulos, T. et al. *Single-shot timing measurement of extreme-ultraviolet free-electron laser pulses*. New Journal of Physics, 10(3):p. 033026 (2008).

[170] Manchon, A. et al. *Theory of laser-induced demagnetization at high temperatures*. Phys. Rev. B, 85(6) (2012).

[171] Martins, M. et al. *Monochromator beamline for flash*. Review of Scientific Instruments, 77(11):115108 (2006).

[172] Mathias, S. et al. *Probing the timescale of the exchange interaction in a ferromagnetic alloy*. Proceedings of the National Academy of Sciences, 109(13):pp. 4792–4797 (2012).

[173] Mathias, S. et al. *Ultrafast element-specific magnetization dynamics of complex magnetic materials on a table-top*. Journal of Electron Spectroscopy and Related Phenomena, 189:pp. 164 – 170 (2013). ISSN 0368-2048.

[174] Mearian, L. *Flash memory's density surpasses hard drives for first time. http://www.computerworld.com/article/3030642/data-storage/flash-memorys-density-surpasses-hard-drives-for-first-time.html* (Accessed 2016-02-08).

[175] Melnikov, A. et al. *Ultrafast transport of laser-excited spin-polarized carriers in* Au/Fe/MgO(001). Phys. Rev. Lett., 107:p. 076601 (2011).

[176] Merschdorf, M. et al. *Transient electron energy distribution in supported ag nanoparticles*. New Journal of Physics, 4(1):p. 95 (2002).

[177] Miesch, S. et al. *Fe on w(110), a stable magnetic reference system*. Journal of Applied Physics, 109(1):013905 (2011).

[178] Moisan, N. et al. *Investigating the role of superdiffusive currents in laser induced demagnetization of ferromagnets with nanoscale magnetic domains*. Scientific Reports, 4:p. 4658 (2014).

[179] Mondal, R. et al. *Ab initio investigation of light-induced relativistic spin-flip effects in magneto-optics*. Phys. Rev. B, 91:p. 174415 (2015).

[180] Moos, G. et al. *Anisotropy of quasiparticle lifetimes and the role of disorder in graphite from ultrafast time-resolved photoemission spectroscopy*. Phys. Rev. Lett., 87:p. 267402 (2001).

[181] Mott, N. F. *The scattering of fast electrons by atomic nuclei*. Proceedings of the Royal Society of London A: Mathematical, Physical and Engineering Sciences, 124(794):pp. 425–442 (1929). ISSN 0950-1207.

[182] Mueller, B., Haag, M. and Fähnle, M. *Ab initio theory for ultrafast magnetization dynamics with a dynamic band structure*. Journal of Magnetism and Magnetic Materials, 414:pp. 14–18 (2016).

[183] Mueller, B. Y. and Rethfeld, B. *Relaxation dynamics in laser-excited metals under nonequilibrium conditions*. Phys. Rev. B, 87:p. 035139 (2013).

[184] Mueller, B. Y. et al. *Driving force of ultrafast magnetization dynamics*. New Journal of Physics, 13(12):p. 123010 (2011).

[185] Mueller, B. Y. et al. *Feedback effect during ultrafast demagnetization dynamics in ferromagnets*. Phys. Rev. Lett., 111:p. 167204 (2013).

[186] Murphy, J., Pellegrini, C. and Bonifacio, R. *Collective instability of a free electron laser including space charge and harmonics*. Optics Communications, 53(3):pp. 197 – 202 (1985). ISSN 0030-4018.

[187] Nozieres, P. *Theory of interacting Fermi systems*. Addison-Wesley (1964).

[188] Oloff, L.-P. et al. *Time-resolved haxpes at sacla: probe and pump pulse-induced space-charge effects*. New Journal of Physics, 16(12):p. 123045 (2014).

[189] Oppeneer, P. M. and Liebsch, A. *Ultrafast demagnetization in ni: theory of magneto-optics for non-equilibrium electron distributions*. Journal of Physics: Condensed Matter, 16(30):p. 5519 (2004).

[190] Oura, M. et al. *Development of a single-shot ccd-based data acquisition system for time-resolved x-ray photoelectron spectroscopy at an x-ray free-electron laser facility*. Journal of Synchrotron Radiation, 21(1):pp. 183–192 (2014).

[191] Ovchinnikov, Y. and Kresin, V. *Relaxation cascade in solids: microscopic theory*. The European Physical Journal B - Condensed Matter and Complex Systems, 32(3):pp. 297–302 (2003). ISSN 1434-6036.

[192] Overhauser, A. W. *Paramagnetic relaxation in metals*. Phys. Rev., 89:pp. 689–700 (1953).

[193] Passlack, S. et al. *Space charge effects in photoemission with a low repetition, high intensity femtosecond laser source*. Journal of Applied Physics, 100(2):024912 (2006).

[194] Patterson, B. D. and Abela, R. *Novel opportunities for time-resolved absorption spectroscopy at the x-ray free electron laser*. Phys. Chem. Chem. Phys., 12:pp. 5647–5652 (2010).

[195] Penn, D. R., Apell, S. P. and Girvin, S. M. *Spin polarization of secondary electrons in transition metals: Theory*. Phys. Rev. B, 32:pp. 7753–7768 (1985).

[196] Penn, D. R., Apell, S. P. and Girvin, S. M. *Theory of spin-polarized secondary electrons in transition metals*. Phys. Rev. Lett., 55:pp. 518–521 (1985).

[197] Pfau, B. et al. *Ultrafast optical demagnetization manipulates nanoscale spin structure in domain walls*. Nat. Commun., 3:pp. 1100– (2012).

[198] Pietanza, D. L. et al. *Non-equilibrium electron and phonon dynamics in metals under femtosecond laser pulses*. The European Physical Journal D, 45(2):pp. 369–389 (2007). ISSN 1434-6079.

[199] Pietzsch, A. et al. *Towards time resolved core level photoelectron spectroscopy with femtosecond x-ray free-electron lasers*. New Journal of Physics, 10(3):p. 033004 (2008).

[200] Piot, P. et al. *Subpicosecond compression by velocity bunching in a photoinjector*. Phys. Rev. ST Accel. Beams, 6:p. 033503 (2003).

[201] Piramanayagam, S. and Srinivasan, K. *Recording media research for future hard disk drives*. Journal of Magnetism and Magnetic Materials, 321(6):pp. 485–494 (2009).

[202] Plihal, M. and Mills, D. *Spin-flip exchange scattering of low-energy electrons in ferromagnetic iron*. Physical Review B, 58(21):p. 14407 (1998).

[203] Pockels, F. *Lehrbuch der Kristalloptik*. B.G. Teubner (1906).

[204] Polyanskiy, M. N. *Refractive index database*.

[205] Popov, S., Svirko, Y. P. and Zheludev, N. *Pump–probe reflective polarization-sensitive nonlinear optics*. JOSA B, 13(12):pp. 2729–2738 (1996).

[206] Poulsen, V. *Method of recording and reproducing sounds or signals.* (1900). US Patent 661,619.

[207] Prandolini, M. J. and Riedel, R. *A review of high power opcpa technology for high repetition rate free-electron lasers*. In *Proceedings of the 36th International Free Electron Laser Conference*, edited by J. Chrin, S. Reiche and V. R. Schaa (2014).

[208] Radcliffe, P. et al. *An experiment for two-color photoionization using high intensity extreme-uv free electron and near-ir laser pulses*. Nuclear Instruments and Methods in Physics Research Section A: Accelerators, Spectrometers, Detectors and Associated Equipment, 583(2-3):pp. 516–525 (2007). ISSN 0168-9002.

[209] Ramberg, E. G. *Optical factors in the photoemission of thin films*. Appl. Opt., 6(12):pp. 2163–2170 (1967).

[210] Reagan, B. A. et al. *Advances in high average power, 100 hz repetition rate table-top soft x-ray lasers*. In *Proceedings of the 14th International Conference on X-Ray Lasers*, edited by M. M. Jorge Rocca, Carmen Menoni,

vol. 169 of *Springer Proceedings in Physics*, p. 416. Colorado State University, Springer International Publishing, Colorado State University, Fort Collins (2016).

[211] Redlin, H. et al. *The {FLASH} pump-probe laser system: Setup, characterization and optical beamlines*. Nuclear Instruments and Methods in Physics Research Section A: Accelerators, Spectrometers, Detectors and Associated Equipment, 635(1, Supplement):pp. S88 – S93 (2011). ISSN 0168-9002. PhotonDiag 2010.

[212] Regensburger, H., Vollmer, R. and Kirschner, J. *Time-resolved magnetization-induced second-harmonic generation from the ni(110) surface*. Phys. Rev. B, 61(21):pp. 14716–14722 (2000).

[213] Reichert, E. *Summary report of the workshop on polarized electron sources and electron spin polarimeters*. In *High Energy Spin Physics*, edited by K.-H. Althoff and W. Meyer, pp. 303–317. Springer Berlin Heidelberg (1991). ISBN 978-3-642-86997-6.

[214] Rhie, H.-S., Dürr, H. A. and Eberhardt, W. *Femtosecond electron and spin dynamics in* Ni/W(110) *films*. Phys. Rev. Lett., 90:p. 247201 (2003).

[215] Richard, F. et al. *Tesla technical design report. part 1. executive summary.* (2001).

[216] Richardson, O. W. *The Emission Of Electricity From Hot Bodies*. Longmans Green And Company (1916).

[217] Rippard, W. H. and Buhrman, R. A. *Ballistic electron magnetic microscopy: Imaging magnetic domains with nanometer resolution*. Appl. Phys. Lett., 75(7):p. 1001 (1999).

[218] Rocca, J., Menoni, C. and Marconi, M. *X-Ray Lasers 2014. Proceedings of the 14th International Conference on X-Ray Lasers*, vol. 169 of *Springer Proceedings in Physics*. Springer International Publishing, 1 ed. (2016).

[219] Rocca, J. J. *Table-top soft x-ray lasers*. Review of Scientific Instruments, 70(10):pp. 3799–3827 (1999).

[220] Röhrs, M., Gerth, C. and Schlarb, H. *Investigations of the longitudinal electron bunch structure at the flash linac with a transverse deflecting rf-structure*. In *Proceedings of the 28th International Free-Electron Laser Conference*, edited by V. R. Schaa, TUBAU06. BESSY, The BESSY FEL Conference Team, BESSY, Berlin (2006).

[221] Ross, A. W. and Fink, M. *Atomic scattering factor and spin-polarization calculations*. Phys. Rev. A, 38:pp. 6055–6058 (1988).

[222] Rossbach, J. *A {VUV} free electron laser at the {TESLA} test facility at {DESY}*. Nuclear Instruments and Methods in Physics Research Section A: Accelerators, Spectrometers, Detectors and Associated Equipment, 375(1-3):pp. 269 – 273 (1996). ISSN 0168-9002. Proceedings of the 17th International Free Electron Laser Conference.

[223] Roth, T. et al. *Temperature dependence of laser-induced demagnetization in ni: A key for identifying the underlying mechanism*. Phys. Rev. X, 2:p. 021006 (2012).

[224] Roy, D. and Tremblay, D. *Design of electron spectrometers*. Reports on Progress in Physics, 53:pp. 1621–1674 (1990).

[225] Rudolf, D. et al. *Ultrafast magnetization enhancement in metallic multilayers driven by superdiffusive spin current*. Nat. Commun., 3:pp. 1037– (2012).

[226] Saiki, T. et al. *Giant nonlinear phase shift at exciton resonance in znse*. Applied physics letters, 60(2):pp. 192–194 (1992).

[227] Salvatella, G. et al. *Ultrafast demagnetization by hot electrons: Diffusion or super-diffusion?* Structural Dynamics, 3(5):055101 (2016).

[228] Sandratskii, L. M. and Mavropoulos, P. *Magnetic excitations and femtomagnetism of ferh: A first-principles study*. Phys. Rev. B, 83:p. 174408 (2011).

[229] Schellekens, A. J. et al. *Investigating the contribution of superdiffusive transport to ultrafast demagnetization of ferromagnetic thin films*. Applied Physics Letters, 102(25):252408 (2013).

[230] Schellekens, A. J. et al. *Exploring laser-induced interlayer spin transfer by an all-optical method*. Phys. Rev. B, 90:p. 104429 (2014).

[231] Schellekens, A. J. et al. *Ultrafast spin-transfer torque driven by femtosecond pulsed-laser excitation*. Nat Commun, 5 (2014).

[232] Schlosser, W. *The temperature dependence of the magnetic moment of iron, nickel and invar for t/t c< 0.5*. Physics Letters A, 40(3):pp. 195–196 (1972).

[233] Schmüser, P. et al. *Free-Electron Lasers in the Ultraviolet and X-Ray Regime. Physical Principles, Experimental Results, Technical Realization*, vol. 258 of *Springer Tracts in Modern Physics*. Springer International Publishing, 2 ed. (2014).

[234] Schneidmiller, E. A. and Yurkov, M. V. *Using the longitudinal space charge instability for generation of vacuum ultraviolet and x-ray radiation*. Phys. Rev. ST Accel. Beams, 13:p. 110701 (2010).

[235] Schoenlein, R. et al. *Femtosecond studies of nonequilibrium electronic processes in metals*. Physical Review Letters, 58(16):p. 1680 (1987).

[236] Shull, C. G., Chase, C. T. and Myers, F. E. *Electron polarization*. Phys. Rev., 63:pp. 29–37 (1943).

[237] Shvyd'ko, Y. V. et al. *High-reflectivity high-resolution x-ray crystal optics with diamonds*. Nat Phys, 6(3):pp. 196–199 (2010). ISSN 1745-2473.

[238] Si, M. S. and Zhang, G. P. *Resolving photon-shortage mystery in femtosecond magnetism*. Journal of Physics: Condensed Matter, 22(7):p. 076005 (2010).

[239] Siegmann, H. et al. *Magnetism with picosecond field pulses*. Journal of Magnetism and Magnetic Materials, 151(1):pp. L8 – L12 (1995). ISSN 0304-8853.

[240] Simrock, S. et al. *Performance of the new master oscillator and phase reference system at flash*. In *Proceedings of the Particle Accelerator Conference*, pp. 188–190 (2007).

[241] Sinclair, C. K. *Electron beam polarimetry*. AIP Conference Proceedings, 451(1):pp. 23–39 (1998).

[242] Singh, N. *Two-temperature model of non-equilibrium electron relaxation: A review*. eprint arXiv:cond-mat/0702331 (2007).

[243] Stamm, C. et al. *Femtosecond modification of electron localization and transfer of angular momentum in nickel*. Nat Mater, 6(10):pp. 740–743 (2007). ISSN 1476-1122.

[244] Stamm, C. et al. *Femtosecond x-ray absorption spectroscopy of spin and orbital angular momentum in photoexcited ni films during ultrafast demagnetization*. Phys. Rev. B, 81(10) (2010).

[245] Stanciu, C. D. et al. *All-optical magnetic recording with circularly polarized light*. Phys. Rev. Lett., 99:p. 047601 (2007).

[246] Steffen, B. R. *Electro-optic methods for longitudinal bunch diagnostics at FLASH*. Ph.D. thesis, University of Hamburg (2007).

[247] Steiauf, D. and Fähnle, M. *Elliott-yafet mechanism and the discussion of femtosecond magnetization dynamics*. Phys. Rev. B, 79:p. 140401 (2009).

[248] Steiauf, D., Illg, C. and Fähnle, M. *Demagnetization on the fs time-scale by the elliott-yafet mechanism*. Journal of Physics: Conference Series, 200(4):p. 042024 (2010).

[249] Steiauf, D., Illg, C. and Fähnle, M. *Extension of yafet's theory of spin relaxation to ferromagnets*. Journal of Magnetism and Magnetic Materials, 322(6):pp. L5–L7 (2010).

[250] Stöhr, J. and Siegmann, H. C. *Magnetism: from fundamentals to nanoscale dynamics*, vol. 152 of *Solid State Sciences*. Springer (2006).

[251] Stoletow, M. *On a kind of electrical current produced by ultra-violet rays*. Philosophical Magazine Series 5, 26(160):pp. 317–319 (1888).

[252] Stoner, E. C. and Wohlfarth, E. *A mechanism of magnetic hysteresis in heterogeneous alloys*. Philosophical Transactions of the Royal Society of London A: Mathematical, Physical and Engineering Sciences, 240(826):pp. 599–642 (1948).

[253] Sun, C.-K. et al. *Femtosecond-tunable measurement of electron thermalization in gold*. Phys. Rev. B, 50:pp. 15337–15348 (1994).

[254] Teichmann, M. et al. *Transient band structures in the ultrafast demagnetization of ferromagnetic gadolinium and terbium*. Phys. Rev. B, 91:p. 014425 (2015).

[255] Tiedtke, K. et al. *Gas detectors for x-ray lasers*. Journal of Applied Physics, 103(9):094511 (2008).

[256] Tiedtke, K. et al. *The soft x-ray free-electron laser flash at desy: beamlines, diagnostics and end-stations*. New Journal of Physics, 11(2):p. 023029 (2009).

[257] Tudosa, I. et al. *The ultimate speed of magnetic switching in granular recording media*. Nature, 428(6985):pp. 831–833 (2004). ISSN 0028-0836.

[258] Turgut, E. et al. *Controlling the competition between optically induced ultrafast spin-flip scattering and spin transport in magnetic multilayers*. PHYSICAL REVIEW LETTERS, 110(19) (2013). ISSN 0031-9007.

[259] Tveten, E. G., Brataas, A. and Tserkovnyak, Y. *Electron-magnon scattering in magnetic heterostructures far out of equilibrium*. Physical Review B, 92(18):p. 180412 (2015).

[260] Varvaro, G. and Casoli, F. *Ultrahigh-density magnetic recording*. Pan Stanford Publishing (2016). ISBN 978-981-4669-59-7.

[261] Vaterlaus, A., Beutler, T. and Meier, F. *Spin-lattice relaxation time of ferromagnetic gadolinium determined with time-resolved spin-polarized photoemission*. Phys. Rev. Lett., 67:pp. 3314–3317 (1991).

[262] Vernier, P. *Surface and volume photoemission in thin films*. Thin Solid Films, 36(1):pp. 223 – 229 (1976). ISSN 0040-6090.

[263] Viefhaus, H. *Low-energy electron diffraction. von m. a. van hove, w. h. weinberg und c.-m. chn. springer-verlag berlin - heidelberg - new york -london -paris -tokyo 1986. XVII, 603 s., 213 abb., DM 124,-.ISBN 3-540-16262-3*. 38(7):pp. 404–404. ISSN 1521-4176.

[264] Vodungbo, B. et al. *Laser-induced ultrafast demagnetization in the presence of a nanoscale magnetic domain network*. Nat Commun, 3:pp. 999– (2012).

[265] Vodungbo, B. et al. *Indirect excitation of ultrafast demagnetization*. Scientific Reports, 6:p. 18970 (2016).

[266] Vogel, E. et al. *Test and commissioning of the third harmonic rf system for flash*. In *Proceedings of the 1st International Particle Accelerator Conference*, edited by A. N. abd Ch. Petit-Jean-Genaz, V. Schaa, T. Shirai and A. Shirakawa, TUPE004. Science Council of Japan and The Physical Society of Japan and Particle Accelerator Society of Japan and Atomic Energy Society of Japan, IPAC'10 OC/ACFA, Kyoto International Conference Center (KICC) (2010).

[267] Vogt, M. et al. *The free-electron laser flash at desy*. In *Proceedings of the 4th International Particle Accelerator Conference*, edited by Z. Dai, C. Petit-Jean-Genaz, V. RW Schaa and C. Zhang, MOYCB101. International Particle Accelerator Conference, Shanghai, China (2013).

[268] Wang, J. et al. *Ultrafast quenching of ferromagnetism in inmnas induced by intense laser irradiation*. PHYSICAL REVIEW LETTERS, 95(16) (2005). ISSN 0031-9007.

[269] Wang, T. et al. *Femtosecond single-shot imaging of nanoscale ferromagnetic order in* Co/Pd *multilayers using resonant x-ray holography*. Phys. Rev. Lett., 108:p. 267403 (2012).

[270] Wang, X. et al. *Temperature dependence of electron-phonon thermalization and its correlation to ultrafast magnetism*. Phys. Rev. B, 81:p. 220301 (2010).

[271] Wang, Y. et al. *Phase-coherent, injection-seeded, table-top soft-x-ray lasers at 18.9 nm and 13.9 nm*. Nat Photon, 2(2):pp. 94–98 (2008). ISSN 1749-4885.

[272] Wellhöfer, M. et al. *Performance of the monochromator beamline at flash*. Journal of Optics A: Pure and Applied Optics, 9(7):p. 749 (2007).

[273] Wietstruk, M. et al. *Hot-electron-driven enhancement of spin-lattice coupling in gd and tb* $4f$ *ferromagnets observed by femtosecond x-ray magnetic circular dichroism*. Phys. Rev. Lett., 106:p. 127401 (2011).

[274] Will, I. et al. *Photoinjector drive laser of the flash fel*. Opt. Express, 19(24):pp. 23770–23781 (2011).

[275] Winkelmann, A. et al. *High efficiency electron spin polarization analyzer based on exchange scattering at fe/w(001)*. Review of Scientific Instruments, 79(8):p. 083303 (2008).

[276] Wolff, P. A. *Theory of secondary electron cascade in metals*. Phys. Rev., 95:pp. 56–66 (1954).

[277] Yafet, Y. *g factors and spin-lattice relaxation of conduction electrons*. Solid state physics, 14:pp. 1–98 (1963).

[278] Yastremsky, I. A., Oppeneer, P. M. and Ivanov, B. A. *Theory of fast time evolution of nonequilibrium spin states in magnetic heterostructures*. Phys. Rev. B, 90(2) (2014).

[279] Zakeri, K. et al. *On the preparation of clean tungsten single crystals*. Surface Science, 604(2):pp. L1 – L3 (2010). ISSN 0039-6028.

[280] Zdyb, R. and Bauer, E. *Spin-resolved inelastic mean free path of slow electrons in fe*. Journal of Physics: Condensed Matter, 25(27):p. 272201 (2013).

[281] Zdyb, R. et al. *Magnetization and structure of ultrathin fe films*. Phys. Rev. B, 80:p. 184425 (2009).

[282] Zhang, G. and Hübner, W. *Femtosecond electron and spin dynamics probed by nonlinear optics*. Applied Physics B: Lasers and Optics, 68(3):pp. 495–499 (1999).

[283] Zhang, G. et al. *Laser-induced ultrafast demagnetization: Femtomagnetism, a new frontier?* In *Spin Dynamics in Confined Magnetic Structures I*, edited by B. Hillebrands and K. Ounadjela, vol. 83 of *Topics in Applied Physics*, pp. 245–289. Springer Berlin / Heidelberg (2002). ISBN 978-3-540-41191-8.

[284] Zhang, G. P. and Hübner, W. *Femtosecond spin dynamics in the time domain*. J. Appl. Phys., 85(8):p. 5657 (1999).

[285] Zhang, G. P. and Hübner, W. *Laser-induced ultrafast demagnetization in ferromagnetic metals*. Phys. Rev. Lett., 85:pp. 3025–3028 (2000).

[286] Zhang, G. P. et al. *Paradigm of the time-resolved magneto-optical kerr effect for femtosecond magnetism*. Nat Phys, 5(7):pp. 499–502 (2009). ISSN 1745-2473.

[287] Zhavoronkov, N. et al. *Microfocus cu k(alpha) source for femtosecond x-ray science*. Opt. Lett., 30(13):pp. 1737–1739 (2005).

[288] Zhou, F., Ben-Zvi, I. and Wang, X. *Beam dynamics simulations for a DC gun based injector for PERL*. In *Proceedings of the Particle Accelerator Conference*, edited by S. W. P. Lucas, vol. 3, pp. 2266–2268. Argonne National Laboratory, Fermi National Accelerator Laboratory, Oak Ridge National Laboratory, Chicago, Illinois (2001).

[289] Zhou, X. et al. *Space charge effect and mirror charge effect in photoemission spectroscopy*. Journal of Electron Spectroscopy and Related Phenomena, 142(1):pp. 27 – 38 (2005). ISSN 0368-2048.

[290] Zhukov, V. P. and Chulkov, E. V. *The femtosecond dynamics of electrons in metals*. Physics-Uspekhi, 52(2):p. 105 (2009).

[291] Zhukov, V. P., Chulkov, E. V. and Echenique, P. M. *$GW + t$ theory of excited electron lifetimes in metals*. Phys. Rev. B, 72:p. 155109 (2005).

[292] Zhukov, V. P., Chulkov, E. V. and Echenique, P. M. *Lifetimes and inelastic mean free path of low-energy excited electrons in fe, ni, pt, and au: Ab initio* GW + T *calculations*. Phys. Rev. B, 73:p. 125105 (2006).

Acknowledgments

First and foremost I would like to thank Prof. Dr. Andreas Vaterlaus for the invaluable opportunity that he has given to me by working in his group. Thanks to him I have had access to world class research in a fascinating topic such as femtomagnetism and I could stay in a new country full of opportunities.

In the same way I want to express my most sincere gratitude to Dr. Yves Acremann for his support and his understanding during the hard process that this thesis has meant for me. I will carry with me some of his impressive knowledge and skills on virtually every subject related to physics, electronics and technology I could think of.

I'm also greatly indebted to my coworkers for their friendly attitude and their worthy insight during this project. Special thanks to Thomas Michlmayr for his patient teachings on vacuum technology, Andreas Fognini for his initiative and collaboration on explaining the details of the FEL measurements, Rafael Gort for his great vibe and his support during the experiments, Christopher Wetli for his humor and sensible discussions, Thomas Bähler for his sharpness and useful training in CAT modeling, Andreas Lichtenberg for his passes in the football tournaments, Simon Däster for his german and programming lessons and Kevin for sharing his last experimental findings.

The collaborating group of Prof. Dr. Danilo Pescia shouldn't go without special mention. Hugo Cabrera for his strong support during my everyday life in Switzerland and his immeasurable quality as a person, Lorenzo de Pietro for his selfless help in my settling as a foreigner; Alessandro Vindigni, Danilo Zanin and Bertolini Gabriele for their team attitude; Dr. Urs Ramsperger for integrating me in the group.

I can't finish this acknowledgment without showing my highest recognition to the people who made this possible in the very first place: my family. Endless gratitude to Pilar for her infinite patience and long-life altruistic support; Josep for his constant sacrifice in making the best out me. My siblings Clara, Pol and Marc, for their unvaluable personalities and for bringing me a sense of a family. To the close friends who have been there during my stay in this country: Albert for holding his hand open in every moment and for being the strongest support in my darkest moments, Pablo and Miguel for their honest comradeship and acceptance. To Stefanie for caring about me and taking me as her dance pupil. To Dorit for her courage in life and for bringing to mine the loveliest joy and tenderness.

Thank you.